1996

Dendrite and silicon particle refinement using aluminum-insoluble elements in hypoeutectic aluminum silicon alloys.

Yunsong. Wen
University of Windsor

DENDRITE AND SILICON PARTICLE REFINEMENT USING Al-INSOLUBLE ELEMENTS IN HYPOEUTECTIC ALUMINUM SILICON ALLOYS

by

Yunsong Wen

A Thesis
Submitted to the Faculty of Graduate Studies and Research
Through the Engineering Materials Program in the
Department of Mechanical and Materials Engineering
in Partial Fulfilment of the Requirement for
the Degree of Master of Applied Science
at the University of Windsor

Windsor, Ontario, Canada

1996

ISBN 0-612-11037-0

Name Yunsong Wen

Dissertation Abstracts International and *Masters Abstracts International* are arranged by broad, general subject categories. Please select the one subject which most nearly describes the content of your dissertation or thesis. Enter the corresponding four-digit code in the spaces provided.

Materials Science
SUBJECT TERM

0794
SUBJECT CODE

UMI

Subject Categories

THE HUMANITIES AND SOCIAL SCIENCES

COMMUNICATIONS AND THE ARTS

Architecture 0729
Art History 0377
Cinema 0900
Dance 0378
Fine Arts 0357
Information Science 0723
Journalism 0391
Library Science 0399
Mass Communications 0708
Music 0413
Speech Communication 0459
Theater 0465

EDUCATION

General 0515
Administration 0514
Adult and Continuing 0516
Agricultural 0517
Art 0273
Bilingual and Multicultural 0282
Business 0688
Community College 0275
Curriculum and Instruction 0727
Early Childhood 0518
Elementary 0524
Finance 0277
Guidance and Counseling 0519
Health 0680
Higher 0745
History of 0520
Home Economics 0278
Industrial 0521
Language and Literature 0279
Mathematics 0280
Music 0522
Philosophy of 0998
Physical 0523
Psychology 0525
Reading 0535
Religious 0527
Sciences 0714
Secondary 0533
Social Sciences 0534
Sociology of 0340
Special 0529
Teacher Training 0530
Technology 0710
Tests and Measurements 0288
Vocational 0747

LANGUAGE, LITERATURE AND LINGUISTICS

Language
- General 0679
- Ancient 0289
- Linguistics 0290
- Modern 0291

Literature
- General 0401
- Classical 0294
- Comparative 0295
- Medieval 0297
- Modern 0298
- African 0316
- American 0591
- Asian 0305
- Canadian (English) 0352
- Canadian (French) 0355
- English 0593
- Germanic 0311
- Latin American 0312
- Middle Eastern 0315
- Romance 0313
- Slavic and East European 0314

PHILOSOPHY, RELIGION AND THEOLOGY

Philosophy 0422
Religion
- General 0318
- Biblical Studies 0321
- Clergy 0319
- History of 0320
- Philosophy of 0322

Theology 0469

SOCIAL SCIENCES

American Studies 0323
Anthropology
- Archaeology 0324
- Cultural 0326
- Physical 0327

Business Administration
- General 0310
- Accounting 0272
- Banking 0770
- Management 0454
- Marketing 0338

Canadian Studies 0385
Economics
- General 0501
- Agricultural 0503
- Commerce-Business 0505
- Finance 0508
- History 0509
- Labor 0510
- Theory 0511

Folklore 0358
Geography 0366
Gerontology 0351
History
- General 0578
- Ancient 0579
- Medieval 0581
- Modern 0582
- Black 0328
- African 0331
- Asia, Australia and Oceania 0332
- Canadian 0334
- European 0335
- Latin American 0336
- Middle Eastern 0333
- United States 0337

History of Science 0585
Law 0398
Political Science
- General 0615
- International Law and Relations 0616
- Public Administration 0617

Recreation 0814
Social Work 0452
Sociology
- General 0626
- Criminology and Penology 0627
- Demography 0938
- Ethnic and Racial Studies 0631
- Individual and Family Studies 0628
- Industrial and Labor Relations 0629
- Public and Social Welfare 0630
- Social Structure and Development 0700
- Theory and Methods 0344

Transportation 0709
Urban and Regional Planning 0999
Women's Studies 0453

THE SCIENCES AND ENGINEERING

BIOLOGICAL SCIENCES

Agriculture
- General 0473
- Agronomy 0285
- Animal Culture and Nutrition 0475
- Animal Pathology 0476
- Food Science and Technology 0359
- Forestry and Wildlife 0478
- Plant Culture 0479
- Plant Pathology 0480
- Plant Physiology 0817
- Range Management 0777
- Wood Technology 0746

Biology
- General 0306
- Anatomy 0287
- Biostatistics 0308
- Botany 0309
- Cell 0379
- Ecology 0329
- Entomology 0353
- Genetics 0369
- Limnology 0793
- Microbiology 0410
- Molecular 0307
- Neuroscience 0317
- Oceanography 0416
- Physiology 0433
- Radiation 0821
- Veterinary Science 0778
- Zoology 0472

Biophysics
- General 0786
- Medical 0760

EARTH SCIENCES

Biogeochemistry 0425
Geochemistry 0996
Geodesy 0370
Geology 0372
Geophysics 0373
Hydrology 0388
Mineralogy 0411
Paleobotany 0345
Paleoecology 0426
Paleontology 0418
Paleozoology 0985
Palynology 0427
Physical Geography 0368
Physical Oceanography 0415

HEALTH AND ENVIRONMENTAL SCIENCES

Environmental Sciences 0768
Health Sciences
- General 0566
- Audiology 0300
- Chemotherapy 0992
- Dentistry 0567
- Education 0350
- Hospital Management 0769
- Human Development 0758
- Immunology 0982
- Medicine and Surgery 0564
- Mental Health 0347
- Nursing 0569
- Nutrition 0570
- Obstetrics and Gynecology 0380
- Occupational Health and Therapy 0354
- Ophthalmology 0381
- Pathology 0571
- Pharmacology 0419
- Pharmacy 0572
- Physical Therapy 0382
- Public Health 0573
- Radiology 0574
- Recreation 0575
- Speech Pathology 0460
- Toxicology 0383

Home Economics 0386

PHYSICAL SCIENCES

Pure Sciences

Chemistry
- General 0485
- Agricultural 0749
- Analytical 0486
- Biochemistry 0487
- Inorganic 0488
- Nuclear 0738
- Organic 0490
- Pharmaceutical 0491
- Physical 0494
- Polymer 0495
- Radiation 0754

Mathematics 0405
Physics
- General 0605
- Acoustics 0986
- Astronomy and Astrophysics 0606
- Atmospheric Science 0608
- Atomic 0748
- Electronics and Electricity 0607
- Elementary Particles and High Energy 0798
- Fluid and Plasma 0759
- Molecular 0609
- Nuclear 0610
- Optics 0752
- Radiation 0756
- Solid State 0611

Statistics 0463

Applied Sciences

Applied Mechanics 0346
Computer Science 0984
Engineering
- General 0537
- Aerospace 0538
- Agricultural 0539
- Automotive 0540
- Biomedical 0541
- Chemical 0542
- Civil 0543
- Electronics and Electrical 0544
- Heat and Thermodynamics 0348
- Hydraulic 0545
- Industrial 0546
- Marine 0547
- Materials Science 0794
- Mechanical 0548
- Metallurgy 0743
- Mining 0551
- Nuclear 0552
- Packaging 0549
- Petroleum 0765
- Sanitary and Municipal 0554
- System Science 0790

Geotechnology 0428
Operations Research 0796
Plastics Technology 0795
Textile Technology 0994

PSYCHOLOGY

General 0621
Behavioral 0384
Clinical 0622
Developmental 0620
Experimental 0623
Industrial 0624
Personality 0625
Physiological 0989
Psychobiology 0349
Psychometrics 0632
Social 0451

To my parents, for their support and encouragement

ABSTRACT

For hypoeutectic Al-Si alloy castings, minimizing dendrite arm spacing and modification of the secondary Si particles is the most effective means for maximizing strength and ductility. Dendrite refinement can be affected by microalloying with selective elements that promote interfacial instability through constitutional and thermal supercooling. The microalloying elements used in commercial Al alloys A319 and A356 are 0.5 to 1.0 wt% of Sb, Bi, In and Sn, which have little or no solubility in Al, i.e. they have extremely low distribution coefficients. Significant refinement of the dendrite structures (decreasing DAS) and the modification of eutectic Si particles were obtained with the additions of the microalloying elements Sb and Bi. Also the mechanical properties (strength, elongation and impact toughness) were significantly improved with Al-insoluble elements.

A dendrite-growth model, based on the Mullins-Sekerka interfacial stability theory, further enhanced by Langer and Muller-Krumbhaar, which uses the thermal supercooling and interfacial instability resulting from solute trapping due to non-steady state growth conditions, is proposed to account for the results.

ACKNOWLEDGEMENTS

The author wishes to express his sincere gratitude to Dr. W.V.Youdelis for his guidance, supervision and valuable discussions through this work.

He would like to sincerely thank Mr. J. Robinson for his technical support and assistance with electron microscopy. He also wishes to thank Dr. D.O. Northwood, Dr. D.F. Watt, J.H. Sokolowski and Dr. A.T. Alpas for their helpful discussions; and Mrs. Barbara L. Denomey for all the help she provided him during his study at Windsor.

Acknowledgements are given to Natural Sciences and Engineering Research Council of Canada for their financial support, and Alcan International for providing the A319 and A356 alloys.

Finally, he must thank his parents for their encouragement, patience and understanding during his graduate work.

TABLE OF CONTENTS

LIST OF TABLES

LIST OF FIGURES

CHAPTER 1

INTRODUCTION

The hypoeutectic Al-Si casting alloys are widely used throughout the automotive and aerospace industries for structural components. These alloys are characterized by their excellent castability and pressure tightness, their good corrosion resistance, and their good tensile and fatigue properties. As-cast grain structures are important for most properties of an alloy material, because subsequent deformation and heat treatment do not change them significantly. For hypoeutectic Al-Si alloy castings, minimizing dendrite arm spacing and modification of the secondary Si particles are the most effective means for maximizing strength and ductility [1].

The addition of microalloying elements to alloys can significantly refine the microstructure and improve the mechanical properties of alloys. In earlier research by Youdelis and coworkers [2-5], it was shown that small additions of third elements (e.g. Si, Be) significantly improves the grain refinement of Al by Ti. The authors proposed that the effect of the third elements results principally from the increase in nucleation entropy and the corresponding increase in the nucleation rate for the peritectic compound $TiAl_3$ when Si or Be are incorporated into the compound. The increased nucleation rate ultimately translates into a finer cast grain structure via the peritectic reaction. It was also shown that the addition of Be to Al-Cu and Al-Mg-Si alloys refines the $CuAl_2$ and Mg_2Si precipitates in the solid-state transformations (aging), and improves the age-hardening response of the alloys [6,7].

The success in refining the microstructure, i.e. refinement of grain size and precipitates in the above alloys by microalloying suggested the same approach may be successful in refining dendrites and precipitates in the Al casting alloys used in the production of engine blocks and heads for the automotive industry, i.e. A319 and A356, which are the principle industrial hypoeutectic Al-Si alloys. The approach used in this investigation is to increase the nucleation rate through selective use of microalloying elements that have the potential to increase the nucleation entropy, and so stimulate the nucleation of the primary phase, or to restrict growth of a phase through a pile-up of a microalloying element (insoluble in the solid), and so force additional nucleation during solidification. In this study, the effect of the Al-insoluble elements Sb, Bi, In and Sn (all have extremely low distribution coefficients in both Al and Si) on the microstructure and mechanical properties of the commercial Al alloys A319 and A356 are investigated. Of most interest is the effect of the above microalloying elements on the dendrite arm spacing, and the morphology and size of the secondary Si particles, and if the refinement translates into an increase in tensile strength, ductility and toughness.

CHAPTER 2

LITERATURE REVIEW

2.1. ALUMINUM-SILICON ALLOYS

The most widely used aluminum casting alloys are Al-Si base alloys. Al alloys containing silicon as the major alloying element offer excellent castability, good corrosion resistance, and can be easily machined and welded. The Al-Si binary phase diagram shows the eutectic silicon level at about 12%*. Al-Si alloys containing silicon less than 12% are hypoeutectic Al-Si alloys, with the A319 and A356 Al-Si alloys containing nominally about 7% silicon.

2.1.1 Alloy Compositions

For the hypoeutectic Al-Si alloys, a number of alloying elements may be added to the melt to influence the mechanical properties of the casting. Silicon promotes castability by improving the fluidity and feeding characteristics of the melt, and also increases the resistance to hot tear. The size and shape of the silicon particles in the eutectic regions of the microstructure strongly influence the mechanical properties of the casting. Silicon additions also result in a reduction in specific gravity and coefficient of thermal expansion for the alloys. Copper increases the strength and hardness of the alloy, especially via thermal

---

* all concentrations in wt%.

processing. Alloys containing 4 to 6% Cu respond most strongly to the thermal treatments (aging). However, copper generally reduces the resistance of the alloy to general corrosion, and Al-Si alloys containing Cu are more prone to hot tearing. The addition of magnesium promotes aging response, and is commonly used in more complex Al-Si alloys containing copper, nickel, and other elements for the same purpose. Mg combines with Si to form the active precipitation - hardening phase Mg_2Si. This compound, when precipitated from solid solution during aging, is responsible for the significant improvement in hardness and mechanical strength of the alloy. Mg_2Si also displays a useful solubility limit corresponding to approximately 0.70% Mg, beyond with either no further strengthening occurs or matrix softening takes place. Common premium-strength compositions in the Al-Si family employ Mg in the range of 0.40 to 0.70%. Iron improves hot tear resistance and decreases the tendency for die sticking or soldering in die casting of Al alloys. Increases in iron content are, however, accompanied by substantially decreased ductility. Small quantities of impurities such as Zn are often present in casting alloys. Zn reduces ductility and should be maintained within specified limits [10,37].

2.1.2 A319 and A356 Alloy Systems

The chemical composition and mechanical properties of the A319 and A356 alloys are given in Table 2.1 and 2.2 respectively, and the thermal properties in Table 2.3. In A319, the Si imparts the good casting characteristics, and the Cu imparts moderately high strength and improved machinability, but reduces the alloy's ductility and resistance to corrosion. Alloy A319 is produced from recycled metal, with the alloying elements added or removed

to meet specific composition ranges. Automobile engine components made from this alloy include cylinder heads and intake manifolds. There are other applications for A319, where its good castability and weldability, pressure tightness and moderate strength are required.

As with A319, the addition of Si imparts excellent castability and resistance to hot-tearing to the A356 alloy. Mg is added to increase the strength and make it an age-hardening alloy. As A356 has excellent casting characteristics and resistance to corrosion, it is used in large quantities for sand and permanent mold casting. Several heat treatments are used and provide the various combinations of tensile and physical properties that make it very attractive for many automotive and aircraft applications. A companion alloy of A356 with lower iron content, affords higher tensile properties in the premium-quality sand and permanent-mold castings. The premium quality A356 alloys, obtained by T6-type heat treatment, are usually specified for military and aircraft applications [8,9].

Table 2.1 Chemical composition of alloys A319 and A356 [38]

Alloy	%Si	%Cu	%Mg	%Ti	%Mn	%Fe	%Zn	Others
A319	5.5-6.5	3-4	<0.1	<0.25	<0.5	<0.1	<0.1	<0.5
A356	6.5-7.5	<0.25	0.2-0.45	<0.25	<0.35	<0.6	<0.35	<0.15

Table 2.2 Mechanical properties of alloys A319 and A356 [38]

Alloy (Temper)	Tensile Strength MPa	Yield Strength MPa	Elongation %	Hardness HB
A319 (As cast)	185	125	2.0	70
A319 (T6)	250	165	2.0	80
A356 (T51)	172	140	2.0	60
A356 (T6)	228	165	3.5	70
A356 (T7)	234	205	2.0	75
A356 (T71)	193	145	3.5	60

Table 2.3 Thermal properties of alloys A319 and A356 [38]

Alloy	Liquidus temperature	Solidus temperature	Solution temperature	Aging temperature
A319	605^{0}C	515^{0}C	500 - 505^{0}C	150 - 155^{0}C
A356	615^{0}C	555^{0}C	535 - 540^{0}C	(T51) 225-230^{0}C (T6) 150-155^{0}C (T7) 225-230^{0}C (T71) 245-250^{0}C

2.2. DENDRITIC GROWTH THEORY

2.2.1 Nucleation Theory

Volmer and Weber [11], and Becker and Doring [12] first developed the classical nucleation theory for the nucleation from the vapour phase. It was extended by Turnbull and Fisher [13] to describe homogeneous nucleation in a condensed system. Crystallization begins with the formation of solid nuclei which then grow by consuming the melt. The small crystals develop as a result of thermal fluctuations. Nuclei capable of growth must satisfy the condition $d(\Delta G)/dr < 0$, where ΔG is the Gibbs free energy change for nucleation and r is the nuclei radius. The total free energy change consists of two parts: a positive free energy change associated with the formation of the solid/liquid interface (surface free energy, γ), and a negative volume transformation free energy change (ΔG_v) for the liquid to solid, thus

$$\Delta G=\frac{4}{3}\pi r^3\Delta G_v+4\pi r^2\gamma \qquad (2\text{-}1)$$

The function goes through an extremum (maximum) at $r^*=2\gamma/\Delta G_v$, and the free energy of formation of critical-sized embryos for homogeneous nucleation is given by

$$\Delta G^*_{hom}=\frac{16\pi\gamma^3}{3(\Delta G_v)^2} \qquad (2\text{-}2)$$

The transformation free energy change for the system (solid plus liquid) per unit volume ΔG_v is related to the volume entropy change (ΔS_v) and undercooling ($\Delta T = T_l - T$, where T_l=liquidus temperature and T the nucleation temperature) by $\Delta G_v \approx -\Delta S_v \Delta T$ [3] , where for regular behaving solutions, ΔS_v is given by [3]

$$\Delta S_v = \sum_r N_r^s (S_r^s - S_r^l) - R\sum_r N_r^s \ln(N_r^l / N_r^s) \qquad (2\text{-}3)$$

where N_r^s and N_r^l refer to the mole fractions of the rth component in the solid and liquid phases respectively, and S_r^s and S_r^l are the molar entropies of the rth component in the pure solid and liquid states respectively, at the nucleation temperature. The behaviour of intermediate compounds or phases of limited solid solubility are far removed from regular solution behaviour. However, by appropriate combination of the solution and compound for the nucleation rate (N) formation reactions and their entropies, the regular solution behaviour can be removed to give

$$\dot{N} = A\exp\left(\frac{-16\pi\gamma^3}{3\Delta S_v^2 \Delta T^2 kT}\right) \qquad (2\text{-}4)$$

where the pre-exponential parameter A includes the embryo surface concentration of atoms, and the jump frequency for the atom (which has an exponential dependency on the activation energy for grain boundary diffusion).

For heterogeneous nucleation, a substrate reduces the surface energy needed to form a nucleus, and thereby decreases the free energy of formation of the critical-sized nucleus by a factor that is a function of the contact angle (θ) at the nucleus/substrate interface. The substrate effect is taken into account by modifying ΔG^* for homogeneous nucleation thus,

$$\Delta G_{het}^* = \frac{16\pi\gamma^3}{3(\Delta S_v)^2 (\Delta T)^2} f(\theta) \qquad (2\text{-}5)$$

where the function $f(\theta)$ is given by

$$f(\theta)=\frac{2-3\cos\theta+\cos^3\theta}{4} \qquad (2-6)$$

2.2.2 Stability of a Solid/Liquid Interface

2.2.2.1 Crystal Growth in Pure Metals

A liquid metal at a temperature below its freezing point should form crystal nuclei, and these nuclei will subsequently grow into large crystals. The shape of solid/liquid interface of pure metals is determined by the way in which the heat of crystallization is dissipated. Suppose Fig.2.1 represents a region containing a solid-liquid interface and that the heat is conducting away from the interface in both directions; that is, the heat is being removed through both the solid and the supercooled liquid. Because of the heat of fusion released at the interface, the temperature of the interface usually rises above that of both the liquid and solid. The resulting temperature contour is shown in Fig.2.1 and is known in general as a temperature inversion [39]. Under this condition, when the temperature falls in the liquid in the advance of the interface, the latter becomes unstable and in the presence of any small perturbation, cells may grow out from the general interface into the liquid. The resulting structure is called a dendrite, and may also become quite complicated, with secondary branches, forming on the primary cell, and possibly with tertiary branches forming on the secondary ones. So dendrite growth will occur in the freezing of pure metals when the interface is allowed to move forward into sufficient supercooling liquid. However, in metals of relatively low purity it is almost impossible to obtain enough thermal supercooling, so the interface will be stable and the entire freezing process is planar (not dendritic) because more

heat would flow in through a bulge into the liquid, less would be conducted away and the solid bulge would melt again [40].

2.2.2.2 Crystal Growth in Alloys - Constitutional Supercooling

The theory termed 'constitutional supercooling' (CS) was first presented by Rutter and Chalmers [14]. This theory related to the unstable growth of a planar interface with undercooling due to the build-up of solute at the solid/liquid interface. Unstable growth of a solid phase in a pure liquid occurs with thermal undercooling. However, in an alloy system the undercooling of the interface can be related to the distribution of solute in the liquid during freezing and to the imposed temperature gradient.

Fig.2.2(a) shows that for steady state planar growth of a binary alloy of C_0 solute composition, the liquid at the interface has composition C_0/k_0 and solid of C_0 must separate from this, where k_0 is the distribution coefficient defined as $k_0 = C_s/C_l$. In growth, the boundary layer composition can increase to C_0/k_0 and the distribution in the liquid is shown in Fig.2.2(b). At a distance in the liquid, far removed from the interface the composition once more is C_0. It is necessary to consider the solute distributions in the liquid ahead of an advancing S/L planar interface during fluctuations in non-steady state growth conditions, and its effects on interface stability. Tiller and Coworkers [35] give the transport equation under following assumptions:

1. Diffusion in the solid is negligible.
2. The value of distribution coefficient k_0 (C_s/C_l) is constant.
3. Convection in the liquid is negligible.

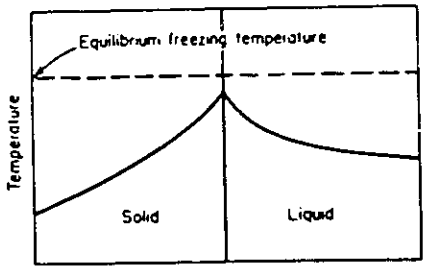

Fig.2.1 Temperature inversion during freezing [39].

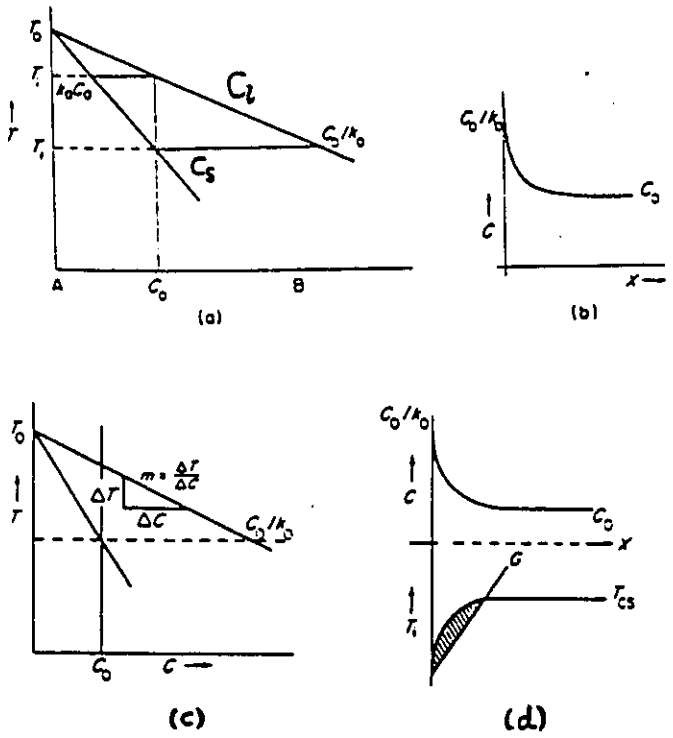

Fig.2.2 (a) Phase diagram. (b) Composition of boundary layer at solid-liquid interface. (c) Relationship between composition and temperature on equilibrium diagram. (d) Conversion of composition-distance to temperature-distance ahead of interface [34].

4. The S/L interface is plane and perpendicular to the axis of the specimen.

The differential equation describing the distribution of solute in the liquid ahead of the solid/liquid interface advancing at a velocity R(≡V) is given by

$$\frac{D\partial^2 C_l}{\partial x'^2}+R\frac{\partial C_l}{\partial x'}=\frac{\partial C_l}{\partial t} \qquad (2\text{-}7)$$

where D is the liquid diffusion coefficient, and x′ is the distance ahead of the interface. As the crystal grows the liquid concentration at the interface will rise because of the solute rejected from the solid according to the equlibrium diagram, which will give rise to the solute concentration in the solid, since the two concentrations are related by the distribtion coefficient k_0. This concentration will continue to increase until a steady state condition is reached. At this point the solid concentration adjacent to the interface will have reached a steady value and the distribution of solute in the liquid near the interface will also be constant too, i.e. dC/dt=0 and Eq.(2-7) becomes

$$\frac{D\partial^2 C_l}{\partial x'^2}+R\frac{\partial C_l}{\partial x'}=0 \qquad (2\text{-}8)$$

which yields a solution

$$C_l=C_0[1+(\frac{1-k_0}{k_0})e^{-(R/D)x'}] \qquad (2\text{-}9)$$

Fig.2.3 shows the steady-state distribution in the liquid ahead of the S/L interface for several k_0 values.

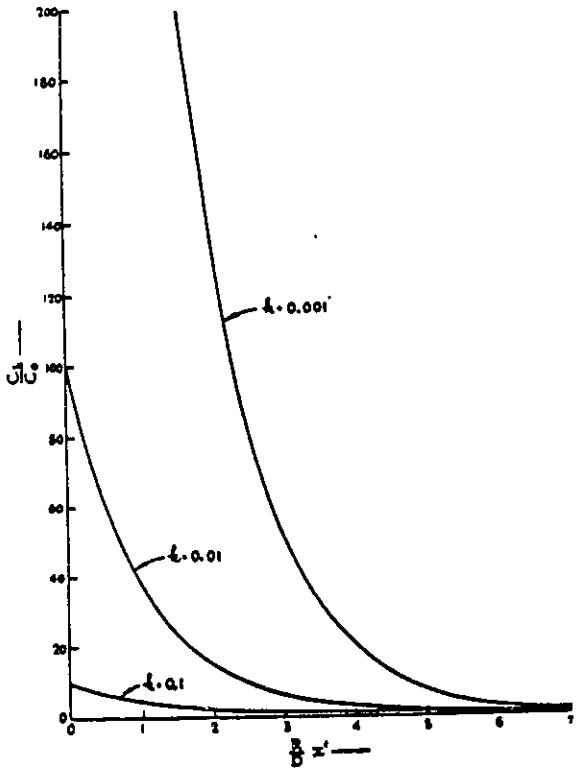

Fig.2.3 Steady state solute distribution in the liquid ahead of the advancing solid-liquid interface [36].

From Fig.2.2(c) the relationship between temperature T and composition C is given by $\Delta T = m\Delta C$. Fig.2.2(d) shows the conversion of the graph relating composition to temperature ahead of the interface. G is the actual temperature gradient in the liquid ahead of the interface. Fig.2.2(d) shows G smaller than the gradient of the liquidus temperature T_{cs} at the interface. This is a condition for constitutional supercooling, i.e. the actual temperature ahead of the interface is below the solidification temperature for the related solute composition. For this condition a point on the solid interface which grows ahead of the planar surface can grow initially under conditions of greater supercooling [15].

The liquidus temperature from Fig.2.2(c) is given $T = T_0 - mC_L$, and m is the slope of liquidus. For the solute boundary layer, the temperature is given by:

$$T = T_0 - mC_0[1 + (\frac{1-k_0}{k_0})e^{-(Rx'/D)}] \qquad \textbf{(2-10)}$$

For constitutional supercooling

$$|dT/dx|_{x'=0} \geq G$$

$$\textit{which gives} \qquad \frac{m(C_0R)}{D}(\frac{1-k_0}{k_0}) \geq G \qquad \textbf{(2-11)}$$

$$\textit{or}$$

$$\frac{G}{R} \leq \frac{mC_0}{D}(\frac{1-k_0}{k_0})$$

Eq.(2-11) show that increasing the solidification rate R, the solute concentration C_0 and decreasing k_0 will increase the tendency for constitutional supercooling for an alloy and that solutes that have little solubility in the parent solid ($k_0 << 1$) will tend to accumulate more

rapidly at the S/L interface.

2.2.2.3 Mullins-Sekerka (MS) Stability Theory

A drawback of the constitutional supercooling criterion is that it ignores the effect of the surface tension of the interface. It is reasonable to suppose that the latter should have a marked influence upon interface stability. In order to investigate this possibility, and to learn more about the morphological changes occurring near to the limit of stability, it is necessary to suppose that the interface has already been slightly disturbed and to study its development under the constraints of diffusion and capillarity. Mullins and Sekerka [16,17] have developed a theory of instability of a solid-liquid interface. In their studies the question of stability is studied by introducing a perturbation in the original interface shape and determining whether this perturbation will grow or decay. The principal physical assumptions of their analysis are those of isotropy of bulk and surface parameters, and of local equilibrium at the interface. The critical mathematical simplification is the use of steady-state values for the thermal and diffusion fields. In fact, the shape of the interface is changing due to the growth (or decay) of a perturbation in its planar shape. And the steady-state calculation is valid only for those perturbations whose shape changes sufficiently slowly. Therefore, stability criteria based on slowly changing perturbations should be reliable.

The perturbed interface can be described by a simple sinusoidal function (see Fig.2.4)

$$z=\phi(x,t)=\delta\sin\omega x \qquad \textbf{(2-12)}$$

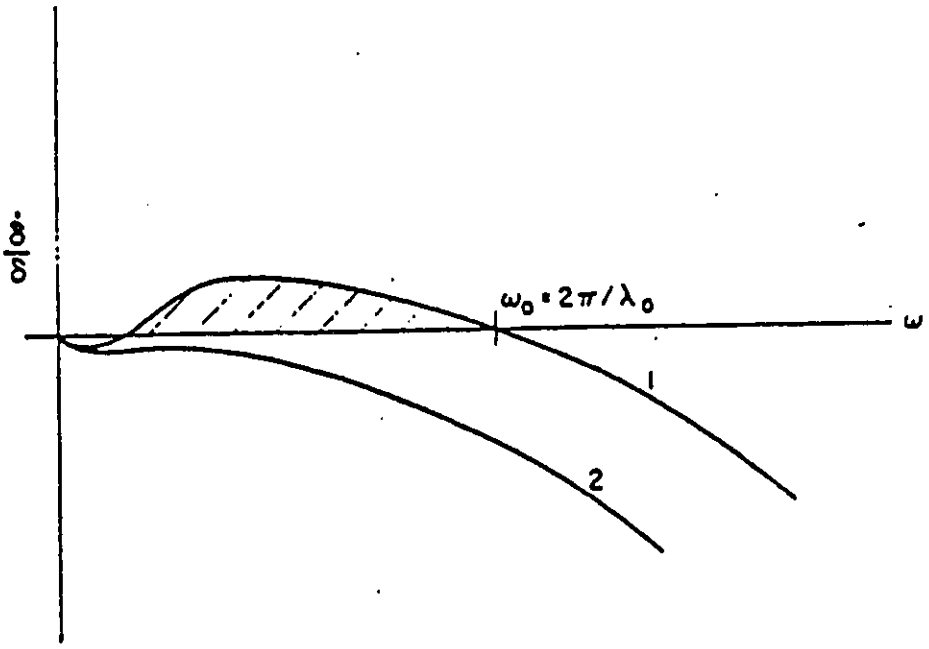

Fig.2.4 δ/δ as a function of frequency for two cases: curve 1 unstable, curve 2 stable [16].

where δ is the amplitude, and $\omega(=2\pi/\lambda)$ is the wave number, λ is wavelength. The MS theory requires solution of appropriate steady-state equations in a frame moving at the constant velocity R, subject to the boundary conditions for the interface and at an infinite distance from the interface (one boundary condition is related to temperature and a second is related to velocity), from which is obtained the critical expression

$$\frac{\dot{\delta}}{\delta}=\frac{R\omega\{-2T_M\phi\omega^2[\omega^*-\frac{R}{D}p]-(g_s+g_l)[\omega^*-\frac{R}{Dp}]+2mG_c[\omega^*-\frac{R}{D}]\}}{(g_s-g_l)[\omega^*-\frac{R}{D}p]+2\omega mG_c} \qquad \textbf{(2-13)}$$

where $\Phi = \gamma/\Delta H$ is a capillary constant in which γ is the specific liquid-solid interfacial free energy and ΔH is the latent heat of the solvent per unit volume; (typically $\Phi \approx 10^{-8}$ cm).

$\omega^* = (R/2D) + [(R/2D)^2 + \omega^2]^{1/2}$;

$p = 1-k_0$;

$G_c = -pC_0R/k_0D$, is the concentration gradient in the liquid at the interface, and

G_l and G_s are the thermal gradients at the unperturbed flat interface (δ=0) in the liquid and solid, respectively;

g_l, g_s are the actual thermal gradient in liquid and solid respectively, where $g_l = (k_l/\bar{k})G_l$, $g_s = (k_s/\bar{k})G_s$, and $\bar{k}=(k_s+k_l)/2$, where k_l=conductivity of liquid, k_s=conductivity of solid.

The value of $\dot{\delta}/\delta$ determines whether the perturbation grows or decays. Stability of the interface with respect to an undulation depends on the sign of $\dot{\delta}/\delta$; a positive value for any ω means growth of some undulations and hence instability of the original flat interface, whereas a negative sign for all ω means decay of all undulations and hence stability.

Proceeding with the analysis of Eq.(2-13), it is evident that the sign $\dot{\delta}/\delta$ depends only on the sign of the numerator since both terms in the denominator are always positive. Since $g_s > g_l$, and $\omega^* > R/D > (R/D)p$ from the definition of ω^*, and from the fact that $p \leq 1$ (for an eutectic system), the first term of denominator is positive. The second term of the denominator is also positive since m and G_c always have the same sign. Therefore, instability or stability depends on whether or not the numerator becomes positive. The numerator consists of three terms: the first term arises from capillarity and is always negative and therefore favours decay of any harmonic; the second term arises from thermal gradients, is negative because g_l, $g_s \geq 0$, and thus also favours decay; the third term, representing the effect of solute on the equilibrium melting temperature, is always positive by the same arguments applied to the denominator and, therefore, always favours growth. Instability occurs if there is any frequency for which the magnitude of the third term exceeds that of the sum of the first two terms; otherwise stability prevails. Stability then is shown to depend on the negative sign for $S(\omega)$, a stability function given by:

$$\begin{aligned} S(\omega) &= -T_m\Phi\omega^2 - (g_s+g_l)/2 + mG_c\{[\omega^* - R/D]/[\omega^* - (R/D)p]\} \\ &= f(\omega) - (g_s+g_l)/2 + mG_c \end{aligned} \tag{2-14}$$

where

$$f(\omega) = -T_m\Phi\omega^2 + mG_c g(\omega)$$

and

$$g(\omega) = \frac{\omega^* - R/D}{\omega^* - (R/D)p} - 1$$

If capillarity is left out of the treatment, $f(\omega) \approx 0$. Stability then depends on the sign of the frequency-independent terms, i.e. $-(g_s+g_l)/2 + mG_c$. It can be shown that if this is less than

zero, the interface will be stable. Substituting g_s, g_l and G_c into Eq(2-14), the modified criterion for stability is obtained

$$\frac{G_l k_l + G_s k_s}{k_l + k_s} \geq \frac{mRC_0}{D}\left(\frac{1-k_0}{k_0}\right) \qquad \textbf{(2-15)}$$

When compared to the constitutional supercooling concept developed by Rutter and Chalmers Eq.(2-11), the MS criterion has introduced the thermal conditions in the solid, which become important as R increases. Figure 2.4 shows a schematic plot of $\dot{\delta}/\delta$ as a function of frequency for two cases; the curve possessing a maximum and becoming positive for a range of frequencies corresponds to an unstable interface; the other curve which is always nonpositive corresponds to a stable interface. In the unstable case, projections develop at the solid/liquid interface, which are the forerunners of dendrite stalks, leading to side branching and ultimately a complete dendritic structure.

2.2.3 Dendrite Arm Model

2.2.3.1 Hunt Model

The Hunt model is based on two major assumptions: (1) a dendritic interface with sidearms is approximated as a smooth steady-state interface, and (2) a constant temperature and a constant liquid composition in the direction normal to the primary dendritic growth direction are assumed. Under these assumptions, Hunt [33] derived the shape of the cells by following the procedure developed earlier by Bower, Brody, and Flemings [18]. Since the second assumption of the Hunt model is valid only for the dendrite or cell region which is far behind the tip, the interface shape in not valid near the tip region. Hunt circumvented this

problem by fitting part of a sphere to the derived shape at the growing front, and obtained the relationship between the tip radius, r, and the primary dendrite spacing λ_1, given by

$$\frac{G\lambda_1^2}{r} = -4\sqrt{2}[mC_t(1-k_0)+\frac{DG}{R}] \qquad \textbf{(2-16)}$$

where C_t is the liquid solute composition at the tip.

The relationship between the dendrite tip undercooling and the dendrite tip radius is derived for a spherical dendrite front model by using a procedure similar to that described by Burden and Hunt [19]. By substituting the value of the dendrite tip radius from Eq.(2-16) into this result, Hunt obtained a result which related primary dendrite spacing to tip undercooling. By assuming that the primary dendrite spacing adjusts to the minimum dendrite tip undercooling, Hunt obtains

$$RG^2\lambda_1^4 = -64\frac{\gamma D}{\Delta S}[m(1-k_0)C_\infty+\frac{k_0GD}{R}] \qquad \textbf{(2-17)}$$

where γ is the solid-liquid interfacial energy, ΔS is the entropy of fusion per unit volume, and C_∞ is the initial solute content of the alloy. When $R >> R_{cs}$, where R_{cs} is the critical velocity at which the planar interface becomes unstable, the second term in the bracket of Eq.(2-17) becomes negligible. Under this condition, Hunt's result can be simplified to

$$\lambda_1 = -(64\frac{\gamma D}{\Delta S})^{\frac{1}{4}}[mC_\infty(1-k_0)]^{\frac{1}{4}}R^{-\frac{1}{4}}G^{-\frac{1}{2}} \qquad \textbf{(2-18)}$$

Examination of Eq.(2-18) shows that a maximum in λ_1 is predicated as a function of velocity (i.e. $\lambda_1 \propto R^{-1/4}$) when G and C_∞ are held constant.

2.2.3.2 Kurz and Fisher Model

Lipton, Gliksman and Kurz [20] have predicted the growth rate and the tip radius of a free dendritic crystal growing into an undercooled binary alloy melt. Free dendritic crystals require an undercooled melt to sustain their growth because this acts as a sink for the latent heat rejected during growth. When the distribution coefficient k_0 is less than the unity, solute is also being rejected into the melt. The corresponding gradients of temperature and concentration in the liquid at the solid-liquid interface are therefore negative. The undercooling ΔT of the melt actually consists of three contributions, namely thermal undercooling ΔT_t, the solutal undercooling ΔT_c, and curvature undercooling ΔT_r, thus

$$\Delta T = \Delta T_t + \Delta T_c + \Delta T_r \qquad \textbf{(2-19)}$$

or

$$\Delta T = \frac{\Delta H}{c_p} P_t + mC_0\{1 - \frac{1}{1-(1-k_0)P_c}\} + \frac{2\Gamma}{r} \qquad \textbf{(2-20)}$$

where ΔH is the latent heat and C_p is the specific heat;

$\Gamma = \gamma/S$, is the Gibbs-Thomson parameter and S is the melting entropy;

P_c and P_t are the solutal and thermal Peclet numbers, respectively, and

r is the tip radius.

If the dendrite tip is assumed to have a parabolic shape, both solutal and thermal supersaturation are directly related to the solutal and thermal Peclet numbers through the Ivantsov transport solution in the first approximation form [21] and are given by

$$P_c=\frac{Rr}{2D} \qquad P_t=\frac{Rr}{2a} \tag{2-21}$$

where a is the thermal diffusivity, and D is the liquid interdiffusion coefficient.

In order to obtain the relationship equation for R and r, the stability criterion is applied. To find the operating point of the system, and avoid the usual ambiguity in the solution, the dendrite tip is tested for stability using the MS result. Because the latter's general equation is quite complicated, Kurz and Fisher [22] suppose the special case of a planar solid-liquid interface, no latent heat ΔH, equal thermal conductivities in solid and liquid, and small distribution coefficient k_0 and starting with the central [MS] obtain [23]

$$r=\{\frac{\Gamma}{\sigma^*(mG_c-G)}\}^{1/2} \tag{2-22}$$

where $\sigma^*=(2\pi)^{-2}$ is a stability constant, and G_c and G are the concentration and temperature gradients respectively, evaluated at the solid-liquid interface.

An approximation to G_c is given by

$$G_c = \frac{RpC_0}{D\Omega p-D} = \frac{C_0}{\frac{r}{2}-\frac{D}{Rp}} \tag{2-23}$$

where Ω = Rr/2D. Combining Eq.(2-22) and (2-23) gives

$$R=\frac{2D(Gr^2+4\pi^2\Gamma)}{r^3pG-2r^2pC_0m+4\pi^2\Gamma rp} \tag{2-24}$$

In order to proceed analytically without solving the above cubic equation in r, it is necessary to consider different limiting cases. For example, when R is small, r will be large (Fig.2.5)

so that Eq.(2-24) can be simplified to

$$R \simeq \frac{2DG}{rpG - 2pC_0 m}, \quad then \quad r = \frac{2D}{Rp} + \frac{2mC_0}{G} \quad (for \quad R < R_{tr}) \qquad (2\text{-}25)$$

Likewise, at high velocity R, r will be very small and Eq.(2-24) can be simplified to:

$$R \simeq \frac{4D\pi^2\Gamma}{r^2 pC_0(-m)}, \quad then \quad r = 2\pi\left(\frac{D\Gamma}{Vk\Delta T_0}\right)^{\frac{1}{2}} \quad (for \quad R > R_{tr}) \qquad (2\text{-}26)$$

where $\Delta T_0 = -mC_0 p/k_0$, and R_{tr} is the transition velocity. The form of Eq.(2-26) is also shown in Fig.2.5.

Kurz and Fisher [22] assumed that the shape of the dendrite can be approximated as an ellipsoid. Assuming that the last liquid solidifies at the distance from the tip, $a = \Delta T'/G$, where $\Delta T'$ is the difference between the tip temperature and the non-equilibrium solidus, and the minor axis of ellipsoid $b = \lambda_1/\sqrt{3}$. The tip radius is determined by $r = b^2/a$. From the geometry of the ellipse, there is found the relationship between r and λ_1

$$r = \frac{b^2}{a} = \frac{\lambda_1^2 G}{3\Delta T'}, \quad and \quad \lambda_1 = (3\Delta T' r)^{\frac{1}{2}} G^{-\frac{1}{2}} \qquad (2\text{-}27)$$

$\Delta T'$ will vary strongly at low and high R, close to the limits of constitutional and absolute stability. Substituting for r from the marginal stability criterion, Eq.(2-25) and (2-26) in Eq.(2-27) gives at low velocity R

$$\lambda_1 = \left[\frac{6\Delta T'}{Gp}\left(\frac{D}{R} - \frac{\Delta T_0 k_0}{G}\right)\right]^{\frac{1}{2}} \qquad (2\text{-}28)$$

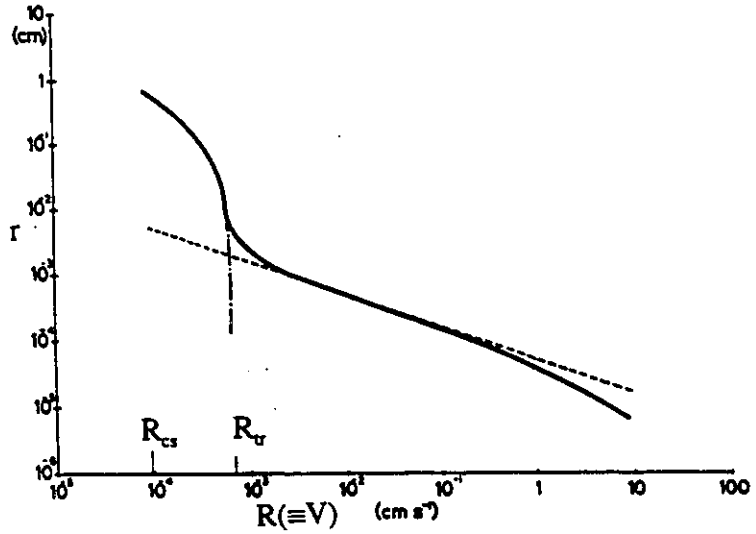

Fig.2.5 Tip radius, r, as a function of growth rate, R for Al-2 wt%Cu at G =100 Kcm^{-1}. Solid line: full solution, Eq.(2-21), dashed line: high rate approximation. Eq.(2-23), dot-dashed line: low growth rate approximation Eq.(2-22) [22].

and at high velocity R

$$\lambda_1 = 4.3(\Delta T')^{\frac{1}{2}}\left[\frac{D\Gamma}{\Delta T_0 k_0}\right]^{\frac{1}{4}} G^{-\frac{1}{2}} R^{-\frac{1}{4}} \qquad \textbf{(2-29)}$$

2.2.3.3 Trivedi Model

Trivedi and coworkers [24-26] selected the transparent succinonitrile-acetone organic system in their study to characterize dendrite tip radius and interdendrite spacings as functions of growth rate and temperature gradient in the liquid. Variations in the primary dendrite arm spacing λ_1, the secondary dendrite arm spacing λ_2, and r with controlled growth rates at a constant temperature gradient are shown in Figure 2.6. The variation λ_1 on the log λ_1 vs log R plot is essentially linear for R between 4 and 100 μm per second. A least square linear regression gives the proportionality equation $\lambda_1 \propto R^{-0.37\pm0.01}$. Below R = 1 μm sec^{-1}, λ_1 decreases sharply with the decrease in R, and the interface changes from a dendritic to cellular structure. But r increases sharply with decreasing R when R is less than 1 μm per second. The experimental results [26] show that for R > 2 μm per second both λ_2 and r depend similarly on R, which indicates a simple relationship between λ_2 and r. It is shown that $\lambda_2/r \approx 2.2 \pm 0.03$ for all velocities studied [25], and is independent of temperature gradient. From the above experimental results, Trivedi, et al arrived at three important conclusions:

(1) The experimentally measured tip radii match precisely with the theoretically predicted values based on an isolated dendrite growth model.

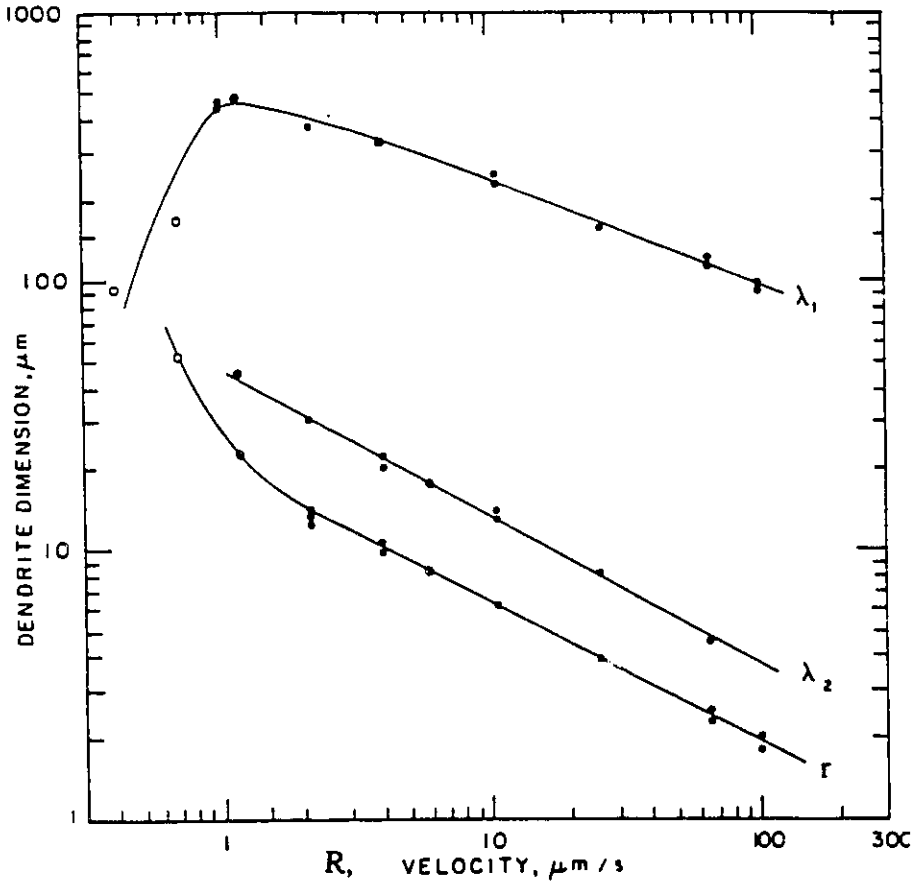

Fig.2.6 Variation of λ_1, λ_2 and r with R at G = 67 K/cm [26].

(2) The sharp decrease in λ_1 occurs at the dendrite-cell transition velocity (Fig.2.6).

(3) In the high velocity regime, a variation in the temperature gradient significantly alters the primary dendrite spacing but has no effect on the tip radius or on the initial secondary dendrite arm spacing.

Given the above, thermal diffusion plays an important part in determining the primary dendrite spacing. Thus, the dimensionless parameter which characterizes the primary dendrite spacing is defined as $\Lambda = (\lambda_1/r)(\lambda_1/l_t) = (\lambda_1^2 G/rk_0\Delta T_0)$, where l_t is the characteristic thermal diffusion length given by $l_t = k_0\Delta T_0/G$. Another dimensionless parameter is defined as $\Lambda' = l_c/l_s = \gamma V/(2\Delta S D k_0 \Delta T_0)$, where l_s is the solute diffusion length ($l_s = 2D/V$) and l_c is the capillary length ($l_c = \gamma/\Delta S k_0 \Delta T_0$). Based on the Hunt model, the general relationship between Λ and Λ' is obtained,

$$\Lambda = 4\sqrt{2}\Lambda' \frac{L}{p^2} \qquad (2\text{-}30)$$

where $L = 1/2(l+1)(l+2)$ in which the l=6 harmonic is found to be operative for the dendrite growth process (L=28).

Substituting Λ and Λ' and p, L into Eq.(2-30), gives the relationship between the dendrite spacing and the dendrite tip radius, for given conditions of solute composition, growth velocity and temperature gradient in the liquid,

$$\lambda_1^2 = 224\sqrt{2} D \frac{\gamma}{\Delta S} G^{-1} R^{-1} r^{-1} \qquad (2\text{-}31)$$

The most important result of this theoretical analysis is the prediction of a maximum in primary spacing as a function of velocity, and this maximum is correlated with the

dendrite-to-cell transition. It is also shown that the dendrite-to-cell transition occurs when the temperature gradient effects become significant and that such a transition is accompanied by a reduction in the primary spacing.

2.2.3.4 Kirkaldy Model

During the past several years, Kirkaldy examined cells and cell-dendrite mixtures for the organic alloys succinonitrile-salol (S-Sa), succinonitrile-acetone (S-A), and pivalicacod-ethanol (P-E). Kirkaldy analyzed data on cell systematics, and found that the relationships for the three systems (S-S, S-A and P-E) submit to the same rational exponents in a power law fit of the experimental results. The metallographic observations for the above three systems yield spacing, amplitude, and aspect ratio (the cell length L to the cell spacing λ_{cell}) measurements. The supercritical power law relations in advance of the cell to dendrite transition are with alloy concentration C_0 in mole fractions [27,28],

$$\lambda_{cell}R^{1/3}G^{1/3}C_0^{1/6} = \begin{cases} 0.16 \pm 0.02 \text{ (S-S) } (2 \le R \le 85 \text{ μm/s}, 4 \le G \le 15 \text{ K/mm}, 0.002 \le X_0 \le 0.007), \\ 0.17 \pm 0.02 \text{ (S-A) } (8 \le R \le 85 \text{ μm/s}, 5 \le G \le 15 \text{ K/mm}, 0.001 \le X_0 \le 0.005), \\ 0.25 \pm 0.02 \text{ (P-E) } (5 \le R \le 85 \text{ μm/s}, 3.5 \le G \le 18 \text{ K/mm}, 0.001 \le X_0 \le 0.005), \end{cases} \quad \textbf{(2-32)}$$

Kirkaldy then considered a semiquantitative justification for empirical formulae (2-32) pertaining to deep-rooted single-valued cells. In the process an additional thermal length m/G, a quantity absent from Mullins and Sekerka marginal formulations, is incorporated into the configuration to give [32]

$$\lambda_1=[24\frac{T_m\sigma_e D}{(1-k_0)\Delta H}]^{\frac{1}{3}}R^{-\frac{1}{3}}G^{-\frac{1}{3}}C_0^{-\frac{1}{6}} \qquad \textbf{(2-33)}$$

where ΔH is the latent heat per unit volume, σ_e is the surface energy of the cellular wall, which subsumes the solute segregation at the root of the cell ($\sigma_e \approx 6\sigma$), T_m is the melting point of alloy. Kirkaldy also shows the Eq.(2-33), i.e. the -1/3 power, more closely agrees with the dendrite spacing observed in the thin film solidification of several transparent organic alloys.

Kirkaldy [29] found experimentally for S-S that in support of the equivalence premise, dendrite tip radii r and secondary branch spacing λ_2 are independent of the temperature gradient and that $\lambda_2 \approx 2.6r \pm 0.3r$, which is very close to the empirical relation ($\lambda_2 \approx 3r$) for free thermal dendrites. Kirkaldy [29] also developed a formula for r based on MS stability theory, as

$$r=(\frac{2\pi}{3})^{\frac{2}{3}}[6d_0\frac{k_0}{C_0(1-k_0)}]^{\frac{1}{3}}(\frac{D}{R_{nt}})^{\frac{2}{3}} \qquad \textbf{(2-34)}$$

where R_{nt} is the normal velocity at the tip. This is remarkably similar in function and magnitude to an estimate from the Mullins and Sekerka marginal wavelength in binary solidification,

$$r=\frac{2\pi}{3}[2d_0\frac{1}{C_0(1-k_0)^2}(\frac{D}{R_{nt}})^2]^{\frac{1}{3}} \qquad \textbf{(2-35)}$$

which may be regarded as an alternative justification for the form of (2-34). Then the secondary branch spacing λ_2 becomes:

$$\lambda_2 = 2\pi[2d_0 \frac{1}{C_0(1-k_0)^2}(\frac{D}{R})^2]^{\frac{1}{3}} \qquad (2\text{-}36)$$

where d_0 is the capillary length. For diffusion controlled growth the capillary length $d_0=\gamma R/k_B N_A T$, where k_B is Boltzmen's constant and N_A Avogadros number, and for thermally controlled growth $d_0 = \gamma/\Delta H$.

2.2.4 Non-Steady Dendrite Growth Model: L-M Stability Criterion

Langer and Muller-Krumbhaar (L-M) applied a Mullins-Sekerka (MS) type stability test to the dendrite tip. According the L-M theory [32], the dendrite tip grows close to the condition of marginal stability. To construct the simplest possible model of the dendritic process, L-M assume that the rate-controlling process is either thermal or chemical diffusion, but not both, and that interface kinetics may be ignored. Further, diffusion only in the liquid phase is considered and any transport of heat or chemical species within the solid is neglected. The defined scaling parameters are: r, the radius of curvature of the front-most tip of a steady-state dendrite, and the diffusion length $l = 2\alpha/R$, where α is either thermal or chemical diffusivity. The ratio r/l is the Peclet number defined earlier (Eq.2-21). The dimensionless ratio σ, which is a measure of the capillarity effect on the instability and growth of the dendrite, given by

$$\sigma \equiv \frac{ld_0}{r^2} = (\frac{\lambda_s}{2\pi r})^2 \qquad \textbf{(2-37)}$$

L-M obtain for the shortest wavelength (λ_s) of a disturbance which would cause a plane interface, moving at the velocity R, to suffer a MS instability

$$\lambda_s = 2\pi\sqrt{ld_0} \qquad \textbf{(2-38)}$$

where d_0 is the capillary length given by

$$d_0 = \frac{T_m\gamma}{\Delta H(\Delta T)} (for\ thermal\ supercooling)$$
$$d_0 = \frac{\gamma\Omega C_{int.}}{(\Delta C)k_B T_m} (for\ constitutional\ supercooling) \qquad \textbf{(2-39)}$$

where γ is the surface tension, C is the composition difference (C_l-C_s), and Ω is the gram atomic volume. It is evident from Eq.(2-39) that an increase in thermal undercooling (ΔT) or constitutional supercooling (ΔC) will result in a decrease (refinement) in dendrite spacing.

In the L-M model, a linear stability analysis of the Ivantsov paraboloidal dendrite (no capillarity, σ=0) in the quasi stationary approximation and in the limit of vanishingly small Peclet number is used. The parabolic coordinate ξ, which is the distance down the dendrite stalk in units of the tip radius r, and the displacement of the surface away from the unperturbed paraboloid $F(\xi,t)$ are introduced (Fig.2.7). The entire coordinate system is understood to be moving with constant velocity R in the z direction; thus any time-dependence of F constitutes a departure from uniform, steady-state growth. This instability is termed a tip splitting stability. When effects of capillarity are taken into account, the result

is a linear equation of motion for $F(\xi,\tau)$ which contains σ as its only system-dependent parameter. In the case of $\sigma=0$, the dendrite grows very slowly with a very large tip radius and the effects of surface tension are negligible. As the capillarity effect increases, R increases and r decreases.

The most striking feature of this time-dependent results is that, for any finite σ, a perturbation at the tip always generates a train of deformations which moves down the dendrite at just such a velocity as to remain nearly stationary in the laboratory frame of reference. The spacing between bumps is always proportional to the stability length λ_s. The side-branching instability is illustrated in Fig.2.8, which shows the sequence of tip shapes computed for a cylindrically symmetric dendrite growing at its natural velocity. The dendrite is shown in the laboratory frame, at five equally spaced instants in time, as it grows from the bottom to the top of the page. The dashed lines indicate approximate growth paths for the secondary tips.

In general, for very small values of σ, r becomes larger and $r > \lambda_s$, then the parabolic tip is unstable and corresponds to the tip-splitting instabilities. As σ increases, to $\sigma = \sigma^* \approx 0.025$, active side-branching instability develops. For $\sigma > \sigma^*$, there are no exponentially growing modes at the tip; however, there is an important marginal instability: when $r < \lambda_s$ the tip is stable, but the sides of the parabola are not stable and side branching occurs and blunts the tips. Because the tip becomes linearly unstable at $\sigma<\sigma^*$, L-M conclude that the operating point is at or near $\sigma=\sigma^*$, for which

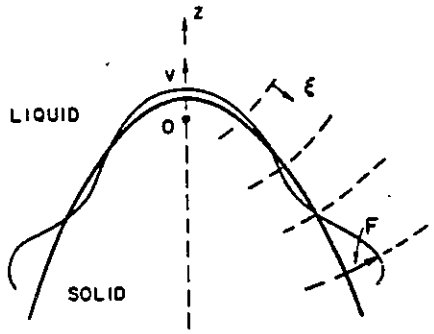

Fig.2.7 Parabolic coordinates used for description of dendritic deformations [32].

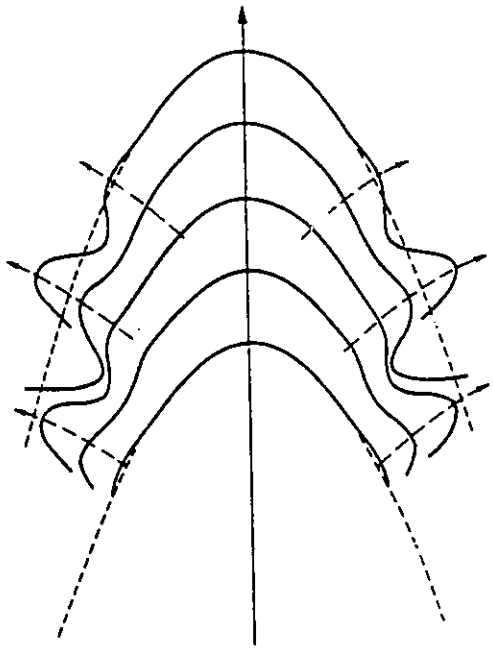

Fig.2.8 Time-ordered sequence of tip shapes for a cylindrically symmetric dendrite growing at its natural velocity ($\sigma = 0.025$) [32].

$$r=\lambda_s \qquad (2\text{-}40)$$

$$\sigma=\sigma^* \cong 0.0253.$$

2.3 EFFECT OF MICROALLOYING ELEMENTS ON INTERFACIAL INSTABILITY

2.3.1 Steady-State and Initial Transient Solute Distributions

Tiller and Co-workers [35] have solved the solute distribution in the liquid and solid for the steady state and initial transient conditions, and obtain the steady state solution for C_l

$$C_l=C_0[1+(\frac{1-k_0}{k_0})e^{-(R/D)x'}] \qquad (2\text{-}41)$$

The region before equilibrium conditions are reached may be termed the transient region. The solute distributions in the liquid for the initial transient stage is given by

$$\begin{aligned} C_l=C_0\{1+\frac{p}{2k_0}e^{-(R/D)x'}erfc[\frac{1}{2}\sqrt{1/Dt}(x'-Rt)] \\ -\frac{1}{2}erfc[\sqrt{1/Dt}(x'+Rt)]+\frac{p}{2}(\frac{1}{p}-\frac{1}{k_0}) \\ e^{-p(R/D)(x'+k_0Rt)}erfc[\frac{1}{2}\sqrt{1/Dt}(x'+(2k_0-1)Rt)]\} \end{aligned} \qquad (2\text{-}42)$$

where p=1-k, x′=distance measured from the interface into the liquid. And for the solid

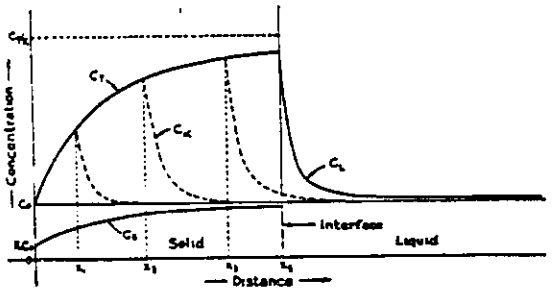

Fig.2.9 Distribution of solute in the liquid C_L and in the solid C_s, in the first part of the specimens to solidify [35].

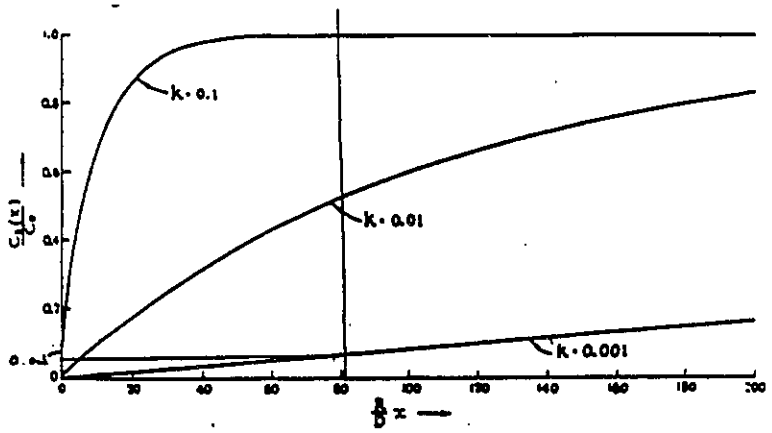

Fig.2.10 Initial transient solute distribution in the solid [36].

$$C_s(x)=\frac{C_0}{2}\{1+erf(\frac{\sqrt{(R/D)x}}{2})+ (2k_0-1)e^{-k_0P(R/D)x}erfc[\frac{2k_0-1}{2}\sqrt{(R/D)x}]\} \quad (2\text{-}43)$$

where x is the distance measured from the beginning of the crystal. Fig.2.9 and Fig.2.10 show the initial transient distributions of the solute in the liquid and in the solid. An approximate but more expediently applied solution for the initial transient solute distribution in the solid is given by [35]

$$C_s=C_0\{(1-k_0)[1-\exp(-k_0\frac{R}{D}x)]+k_0\} \quad (2\text{-}44)$$

The rise of C_s is illustrated in Fig.2.9.

2.3.2 Effect of Sudden Change of the Solidification Rate

If the rate of steady state growth is suddenly changed to R_1>R, since the amount of solute carried ahead of the interface in the steady state case is less for R_1 than for R, the difference must appear in the solid, rising from C_0 to a transient value that again decays in time to the steady state value C_0. The rise in the solid is accompanied by a rise in the interfacial liquid, maintaining equilibrium according to the phase diagram. The transient concentration distribution produced in the solid as a result of the speed change is given by [35]

$$\frac{C_s(x_1)}{C_0}=1-\frac{1}{2}erfc(\frac{\sqrt{(R_1/D)x_1}}{2})+p(\frac{\frac{1}{2}-R/R_1}{k_0-R/R_1})$$
$$\exp[-\frac{R}{R_1}(1-\frac{R}{R_1})\frac{R_1}{D}x_1]erfc[(\frac{R}{R_1}-\frac{1}{2})\sqrt{(R_1/D)x_1}]+ \qquad (2\text{-}45)$$
$$(\frac{2k_0-1}{2})(\frac{1-R/R_1}{k_0-R/R_1})e^{-k_0p(R_1/D)x_1}erfc[(k_0-\frac{1}{2})\sqrt{(R_1/D)x_1}]$$

where x_1 = distance from the point at which the speed change occurred. A family of curves each corresponding to a different value of R/R_1 is obtained for each value of k_0. Three such families of curves are shown in Fig.2.11. This increase in solute concentration in the solid is termed solute trapping, and depends on the k_0 and R/R_1 values. For example, for a k_0=0.01, and a solidification speed increase of 100%, there is a twofold increase in the maximum solute solid concentration attached, and for a tenfold increase in velocity, there is an eightfold increase in C_s.

It is evident that even when the microalloying element is not at its steady-state distribution, a sudden doubling of the interface velocity can result in the liquid concentration reaching very high values for elements highly insoluble in the primary solid (i.e. for $k_0<<1$), - i.e. approaching 100%.

2.3.3 Effect of Post Solute Trapping - Thermal Undercooling

During the uncontrolled solidification, the solidification rate (interface velocity) fluctuates due to thermal fluctuations associated with convective flow fluid. As the interface velocity is suddenly increased, the concentration of the microalloying element will reach high values above C_0/k_0 (eg. $2C_0/k_0$, $4C_0/k_0$, etc.). As the interface concentration is again restored

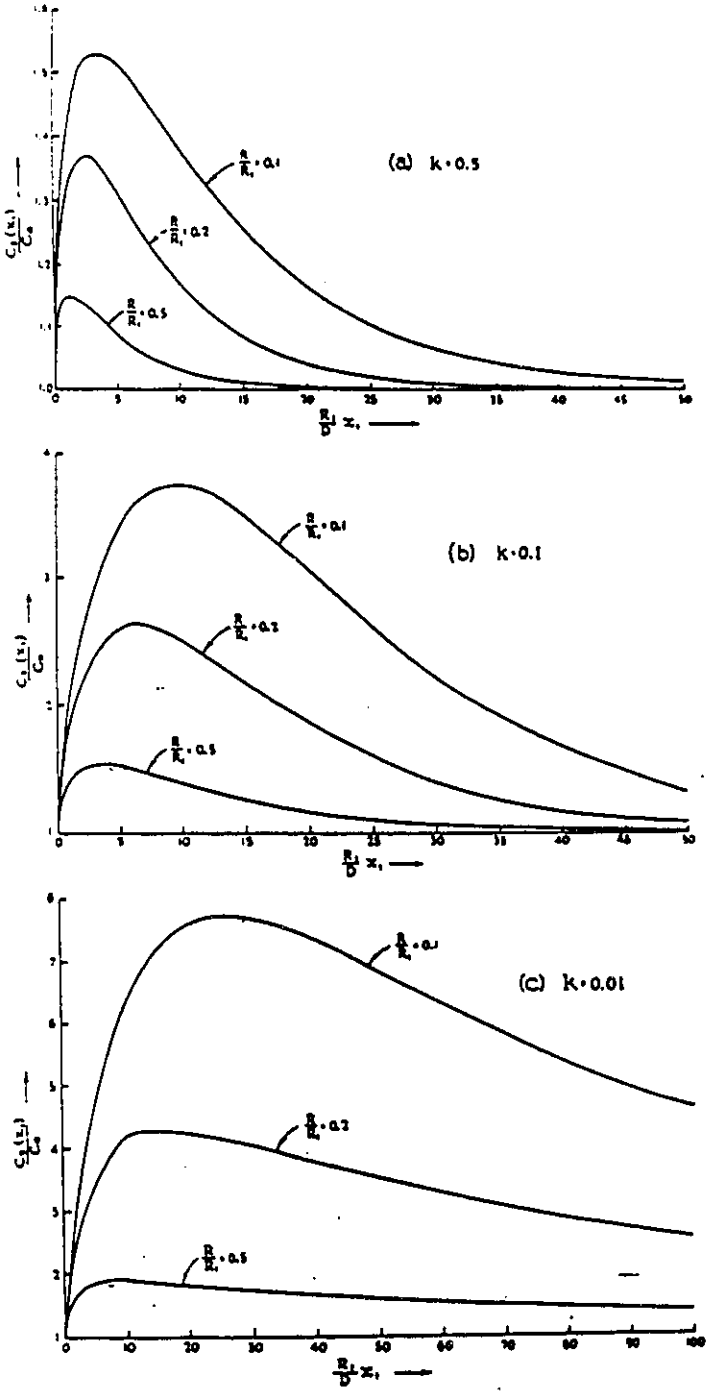

Fig.2.11 Initial Transient solute distribution in the solid caused by a change in the rate of solidification.

to its steady-state value (C_0/k_0), the solution of the diffusion equation becomes Gaussian (Fig.2.12), as opposed to the steady state (error function) mode. Considering only the diffusion component of the liquid solute transport ahead of the interface, the distribution of the solid-insoluble solute element (eg. C) in the liquid will be [38]

$$C_C(x,t) = \frac{Q}{\sqrt{\pi Dt}}\exp\left(\frac{-x^2}{4Dt}\right) \qquad \textbf{(2-46)}$$

$$At\ x=0,\ C(0,t)=\frac{Q}{\sqrt{\pi Dt}}$$

where Q is the maximum solute build-up in the interfacial region following a velocity increase. Fig.2.12 shows the concentration profile in the liquid is concave downward in the interface region. Also, it is a noteworthy that the concentration is exponentially dependent on D, so that even a small increase of D with concentration will result in a large decrease in the negative curvature of the concentration profile in the interface vicinity, i.e. the gradient ($\partial C/\partial x$) can approach zero.

The solute (C), solvent (A), and temperature distributions in the liquid ahead of the advancing interface are shown in Fig.2.13 for the steady-state (SS) and post-trapping (PT) transient cases. Note that when the concentration (C_C) of the insoluble microalloying element builds up to high levels, and takes on a Gaussian distribution (post-trapping), it necessarily forces an inverse Gaussian distribution for the solvent metal (C_A), which is the primary and major solidifying component, and forces a radical decrease in the concentration gradient ($\partial C_A/\partial x$), and thus the diffusion rate of the solidifying component, and correspondingly, a decrease of an equal magnitude of the solidification rate and rate of latent heat production.

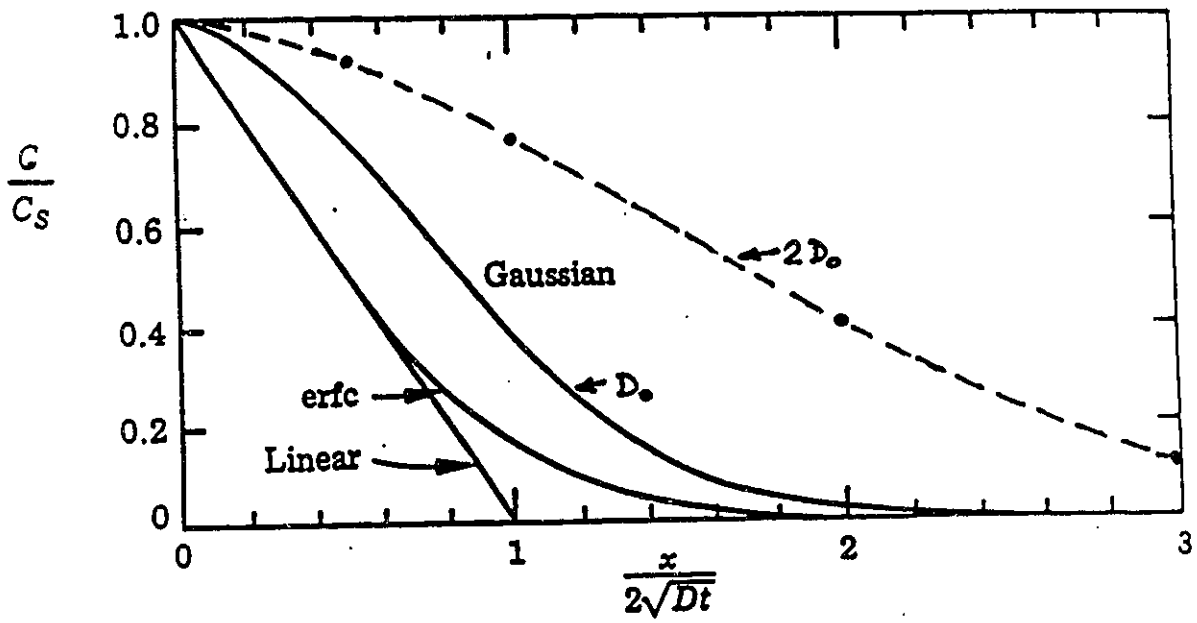

Fig.2.12 Gaussian Distribution

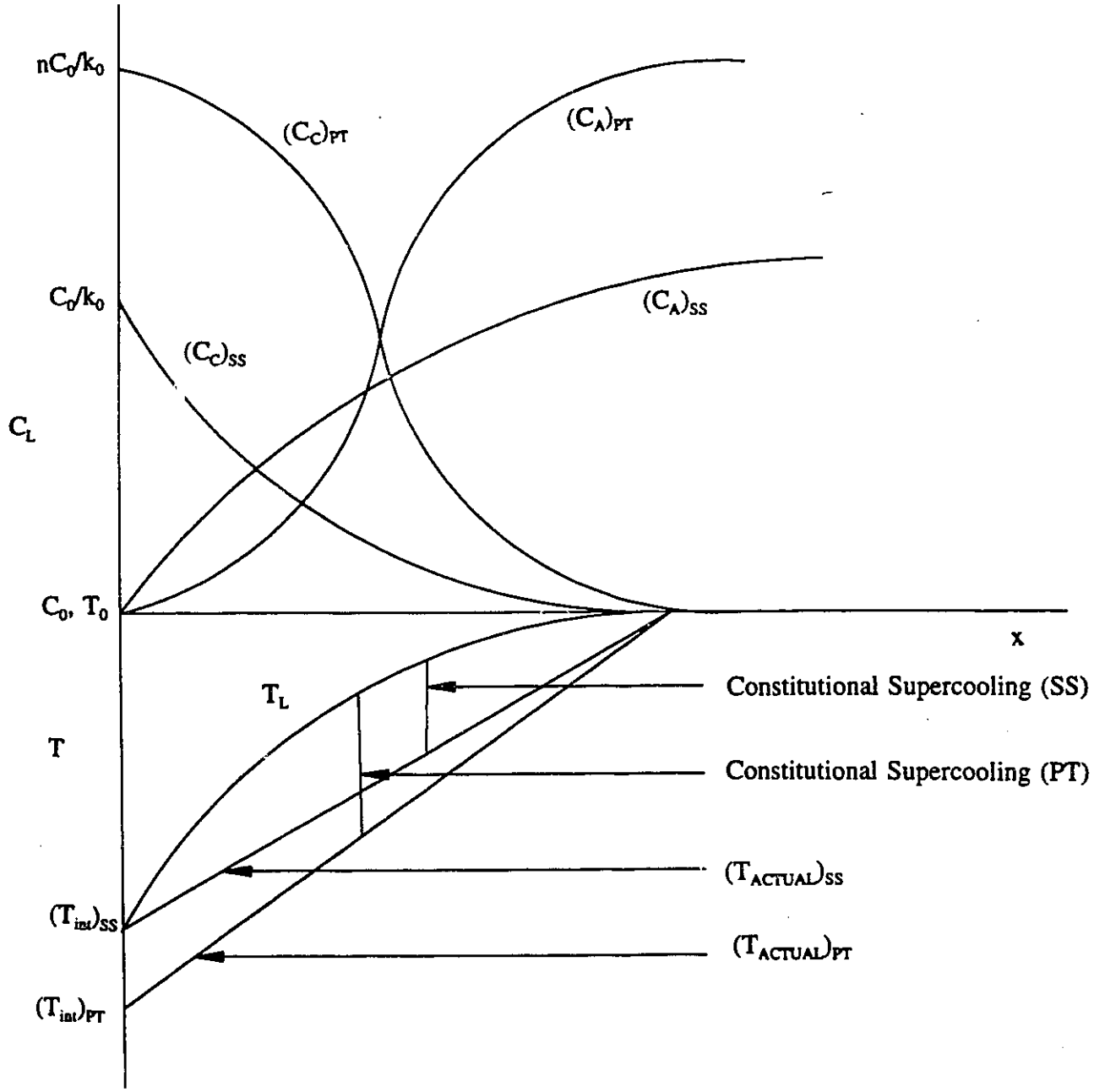

Fig.2.13 Solute, Solvent, Temperature Distributions for Steady State and Post Trapping Transient State.

However, temperature gradients that were established in the solid for the faster solidification rate will temporally persist, forcing the temperature of the interface solid and liquid to drop, i.e. thermal supercooling will be significantly increased as shown in Fig.2.13, and thus dendritic growth promoted.

2.3.4 Effect of Variable Diffusivity ($\partial D/\partial C > 0$)

The concentration of an insoluble element, although present in dilute amounts, can rise to very high levels at the interface when the distribution coefficient is very small and there is a velocity fluctuation. This requires consideration of the effect of an increasing D with concentration on the form of the transient distribution of the (solid-insoluble) solute in the interfacial liquid.

For a variable diffusivity the transport equation is in general given by

$$\frac{\partial C_c}{\partial t} = \frac{\partial}{\partial x}\left(D_c \frac{\partial C_c}{\partial x}\right) + R\frac{\partial C_c}{\partial x} \qquad (2\text{-}47)$$

which becomes

$$\frac{\partial C_c}{\partial t} = \frac{\partial D_c}{\partial C_c}\left(\frac{\partial C_c}{\partial x}\right)^2 + D_c\frac{\partial^2 C_c}{\partial x^2} + R\frac{\partial C_c}{\partial x} \qquad (2\text{-}48)$$

For the case of $\partial D_c/\partial C_c > 0$, the first term in Eq.(2-48) gives a positive contribution to C_c when the concentration is decreasing with a negative curvature, (i.e. for $\partial C_c/\partial x < 0$ and $\partial^2 C_c/\partial x^2 < 0$), i.e. it is an "uphill" diffusive component in the overall negative solute transport. To enhance interfacial segregation, insoluble solutes that have a potential for

"uphill diffusion" should be used for microalloying.

Eq.(2-48) can be numerically solved for the steady state case (i.e., for $\partial C_c/\partial t=0$) using

$$C''(x_i)=\frac{C_{i+1}-2C_i+C_{i-1}}{(\Delta x)^2}$$

and

$$C'(x_i)=\frac{C_{i+1}-C_{i-1}}{2(\Delta x)}$$

to give for Eq.(2-48)

$$\frac{a(C_{i+1}-C_{i-1})^2}{4D^0+4aC_i}+C_{i-1}[1-\frac{\Delta x\cdot R}{2D^0+2aC_i}]-2C_i+[1+\frac{\Delta x\cdot R}{2D^0+2aC_i}]C_{i+1}=0$$

The numerical solution of Eq.(2-48) for the steady-state case shows that it has a monotonically decreasing slope, with a reduced but still positive curvature (Fig.2.14). However, in the initial transient interval, due to velocity fluctuations (prior to the steady state being established) and the increasing D with concentration, the concentration profile near the interface will tend to the Gaussian rather than the error function form, i.e. it has a negative curvature temporarily.

2.3.5 Thermodynamic requirement for $\partial D_c/\partial C_c > 0$

The thermodynamic condition for the diffusion coefficient to increase with concentration can be determined using Darken's Intrinsic Diffusion Coefficient [41], i.e.

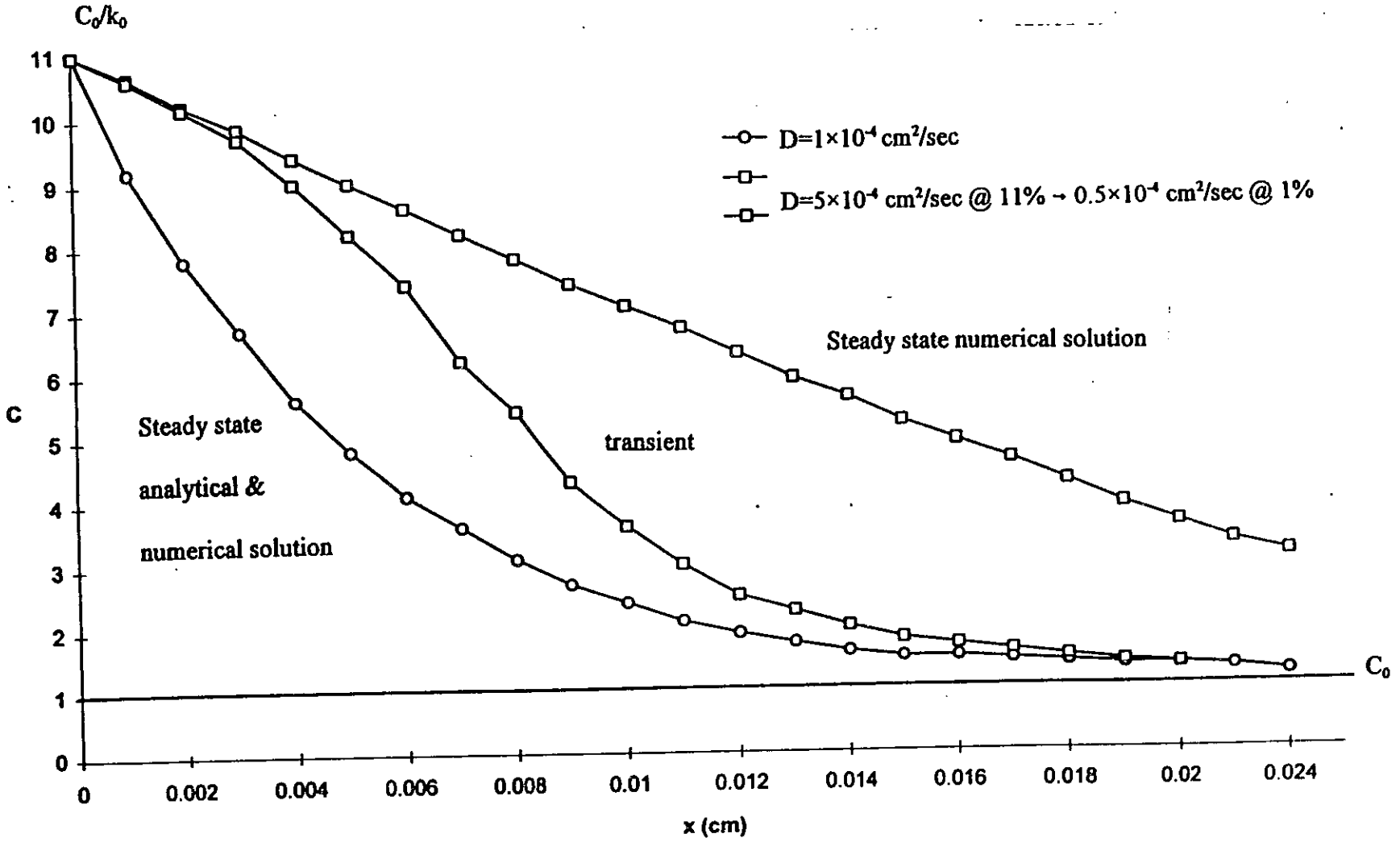

$R=2\times10^{-2}$ cm/sec, $k_0=0.091$, $C_0=1\%$

Fig.2.14 Liquid Solute Distribution for Constant and Variable Diffusivities - Steady State and Initial Transient Distribution.

$$D_c = D_c^0(1 + C_c\frac{\partial \ln\gamma_c}{\partial C_c}) \qquad (2\text{-}49)$$

from which

$$\frac{\partial D_c}{\partial C_c} = (\frac{\partial \ln\gamma_c}{\partial C_c} + C_c\frac{\partial^2 \ln C_c}{\partial C_c^2}) > 0 \qquad (2\text{-}50)$$

The activity coefficient γ is related to the Gibbs free energy of mixing of the solution and the chemical potential $\Delta\mu_c$.

For a binary solution

$$\Delta G = RT(C_A \ln C_A + C_C \ln C_C) + \Delta G^{xs} \qquad (2\text{-}51)$$

$$\Delta\mu_c = RT\ln(\gamma_C C_C)$$
$$\Delta\mu_C = \Delta G^{xs} + (1 - C_c)\frac{\partial}{\partial C_c}(\Delta G) \qquad (2\text{-}52)$$

Combine Eq.(2-51),(2-52) gives

$$\ln\gamma_c = \frac{1}{RT}[\Delta G^{xs} + (1 - C_c)\frac{\partial}{\partial C_c}(\Delta G^{xs})] \qquad (2\text{-}53)$$

Thus, if the excess free energy of mixing for the A-C solution is known, then $\ln\gamma_c$ can be related to C_c at which "uphill diffusion" occurs as determined using Eq.(2-50).

CHAPTER 3

EXPERIMENTAL

3.1 MATERIALS AND CASTING

The commercial Al-Si alloys A319 and A356, provided by Alcan International (Kingston R&D Centre), were used as the base alloys in the study. The microalloying elements Sb, Bi, In and Sn were added either as pure metals or as Al master alloys containing 10% of the microalloying element.

The alloys were prepared in graphite crucibles by induction melting the base alloy (A319 or A356) first, and then adding the microalloying element, either in the pure state or via the master alloy. The melts were heated to well above the liquidus temperature (~900^{0}C) for about 10 minutes and periodically stirred to ensure complete homogenization, and then held under vacuum for 5 minutes for degassing prior to pouring into molds. Two types of molds were used to obtain different cooling rates. To obtain a fast cooling rate (4.0^{0}C/s) the melts were poured from 750^{0}C into graphite molds (20mm dia × 60mm) at room temperature (25^{0}C). The mold for mechanical testing (A356, A356+1.0%Sb) was prepared in the same manner as above except that it was machined with two vents in the bottom and two vents on each side of the parting lines (see Fig.3.1), which were to facilitate air entrapment when pouring melts. The slower solidification rate of 0.3^{0}C/s was obtained by pouring from a melt temperature of 900^{0}C into molds consisting of pyrex tubes (20mm dia × 130mm) set in sand,

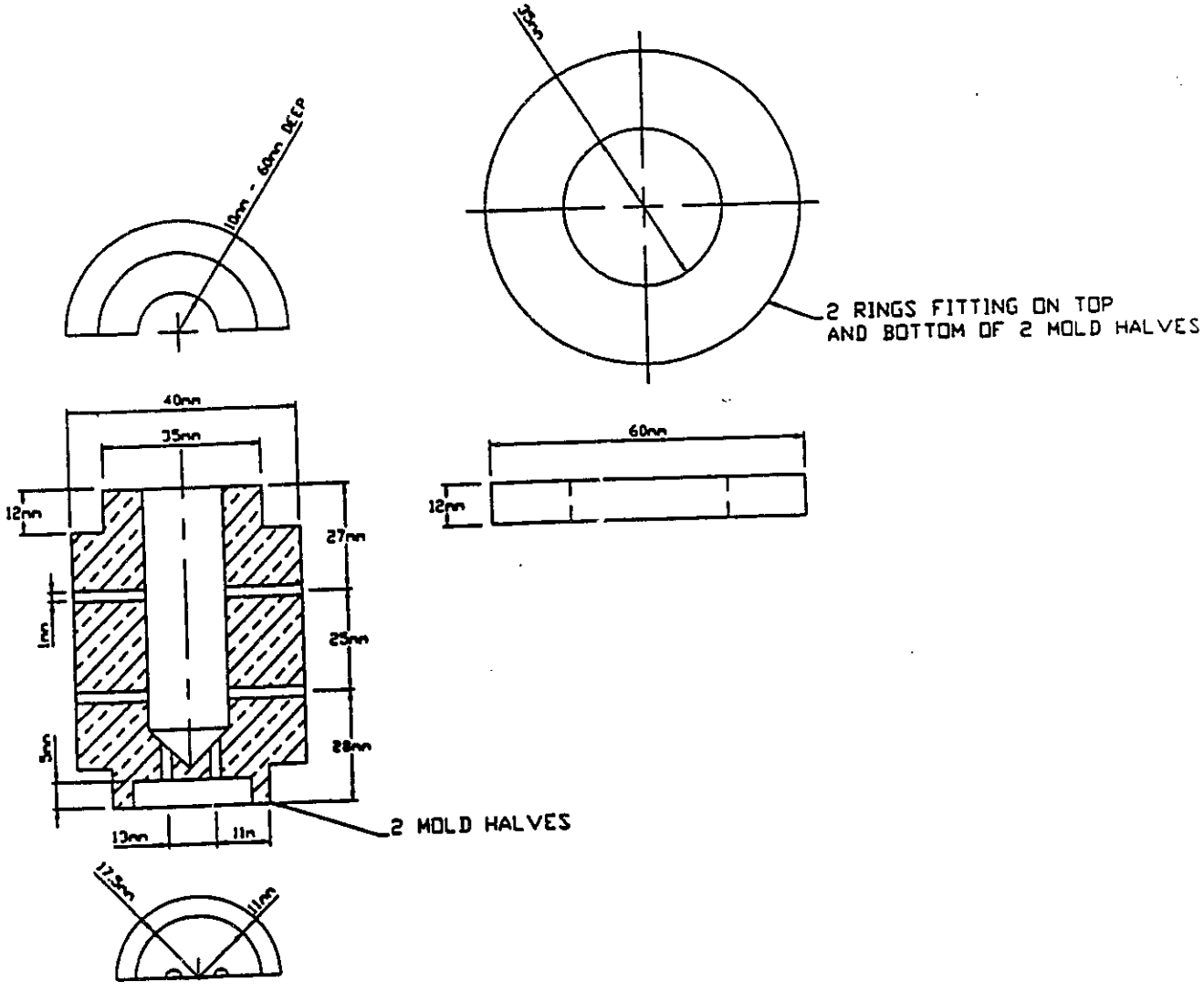

Fig.3.1 Mold for mechanical testing ingots

with the mold assembly (container, sand, and tube) preheated to 250^{0}C prior to ingot pouring.

3.2 ANALYTICAL PROCEDURE

3.2.1 Thermal Analysis

Thermal analysis was performed on all ingots using a type K (Chromel - Alumel) thermocouples (0.5mm dia). The thermocouples were positioned midheight in the mold to record the thermal history of the casting during solidification. The cooling curves were obtained by connecting the thermocouple to a high speed data acquisition system, comprised of a Meltlab3 software, installed on a personal computer (486) linked to an A/D converter supplied by Foundry Information Systems. This system has a sampling rate of 6 Hz and was able to produce adequate cooling curves.

3.2.2 Optical and SEM Analysis

Samples for metallographic analysis were cut from the centre of the solidified ingots. Specimens for optical microscopy were prepared in the conventional manner, starting with grit paper (down to No. 600), then 1 μm alumina polish, and then 0.05 μm alumina, and finishing with colloidal silica suspension for the polishing media. The etchant used was dilute Keller's etchant. Etching was performed by submerging the specimen in the etchant for 5-10 seconds, and then rinsing the specimen surface with running tap water. The specimens from thermal analysis were used to correlate their microstructure with the cooling curves. The optical microscope used was a Leitz Laborlux 12 model, with a maximum

magnification of 1000×. For scanning electron microscopy (SEM) analysis, a progressive etching was carried out, sufficient to create a topographic contrast. A "JSM-5800 LV" SEM was used for the secondary and back-scattered electron imaging mode at 10 KV, and X-ray map technique to determine the distribution of each element in the specimen. Dendrite arm spacing was measured by using the line intercept method, at least three different locations were scanned within a specimen at locations where fully developed dendrites were present. The mean of the above measurements was taken as the dendrite arm spacing (DAS).

3.3 MECHANICAL TESTING

The slower solidified ingots (0.3^0C/s) were cut into three equally sized pieces from the top, middle and bottom of the ingot, from which cylindrical tensile specimens (4mm dia × 16mm gauge length) were machined (see Fig.3.2). Tensile tests were performed at a strain rate of $10^{-3}s^{-1}$ using an Instron Universal Testing Instrument. The tensile property data (0.2% yield strength Y_s, ultimate tensile strength UTS and elongations to failure E_f) are based on the average of three tests. For impact testing by the ZWICK charpy apparatus, ASTM Type A (subsize) charpy V-notch specimens (10mm × 10mm) were milled from the central region of the as-cast ingots. The dimensions of the V-notch specimens are shown in Fig.3.2 (b). Charpy V-notch energy (CVN) data were obtained by testing at room temperature, and are based on the average of three tests.

For the faster solidified ingots, 5 rectangular specimens, 1.5 mm thick and 40mm length, were cut from ingot, from which tensile specimens (1.5mm × 10mm gauge length)

were machined (see Fig.3.3). Tensile tests were performed by Westmoreland Mechanical Testing & Research Inc. (Youngstown, Pennsylvania). All the tensile property data (Y_s, UTS and E_f) are based on the average of at least four tests. ASTM Type A (subsize) charpy V-notch specimens (5mm × 5mm) were milled from the as-cast ingots. The dimensions of the V-notch specimens are shown in Fig.3.3 (b). Charpy V-notch energy (CVN) data were obtained from the average of four tests.

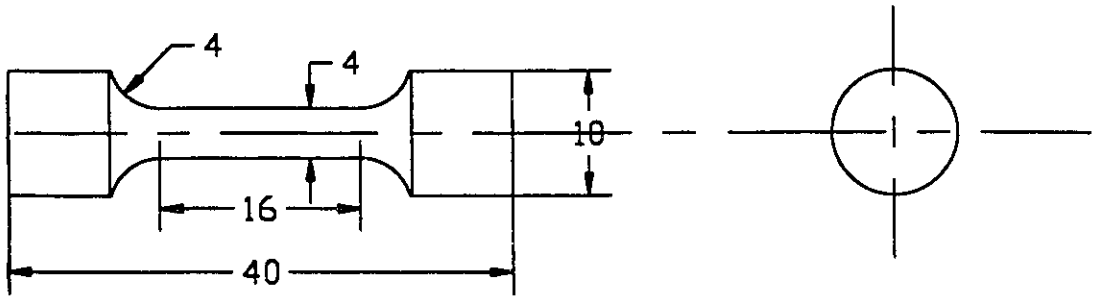

(a)

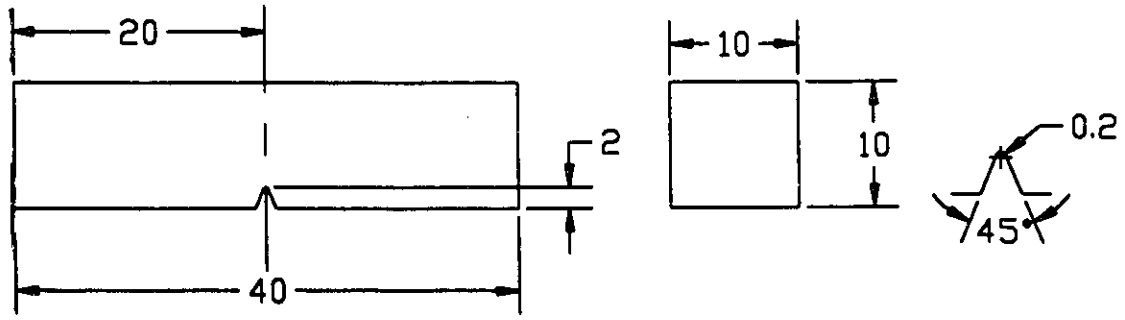

(b)

Fig.3.2 (a) Cylindrical tension test specimen;

(b) Charpy impact test specimen (all dimensions in mm).

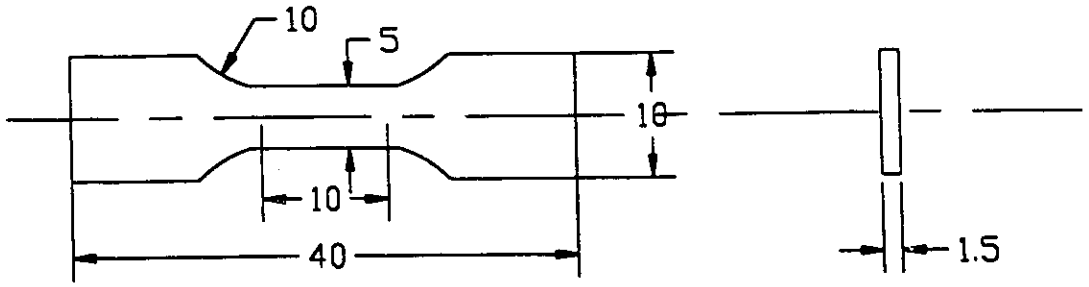

(a)

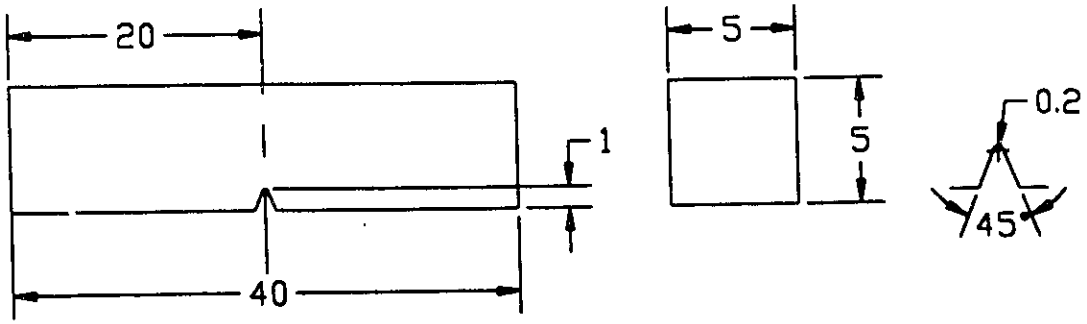

(b)

Fig.3.3 (a) Rectangular tension test specimen;

(b) Charpy impact test specimen (all dimensions in mm).

CHAPTER 4

RESULTS AND DISCUSSION

4.1 THERMAL ANALYSIS

Thermal analysis is a technique where the temperature of the melt is monitored during solidification, and characteristic parameters are then correlated with the observed microstructural features. In this study the modification effects of the insoluble elements on the primary phase and eutectic phases can be related to changes in the cooling curve of A356 alloy. The microalloying elements have the most significant effect on the eutectic reaction, as evident from changes in the cooling curve; specifically a lowering of the eutectic arrest temperature, an increase in the apparent undercooling required to start eutectic freezing, and a lengthening of the time required for the required for the eutectic reaction.

There is considerable variation in the literature [42-44] concerning the definitions of thermal analysis parameters. The method of calculation of cooling rate, eutectic arrest temperature and eutectic undercooling adopted here follows that of Gruzleski and coworkers [45] and is illustrated in Fig.4.1.

- Cooling Rate: calculated by taking the slope of the straight line portion of the cooling curve (590-560^{0}C).
- Liquidus Temperature (T_L): temperature corresponding to the liquidus maximum temperature, and is generally assumed to be the nucleation temperature.

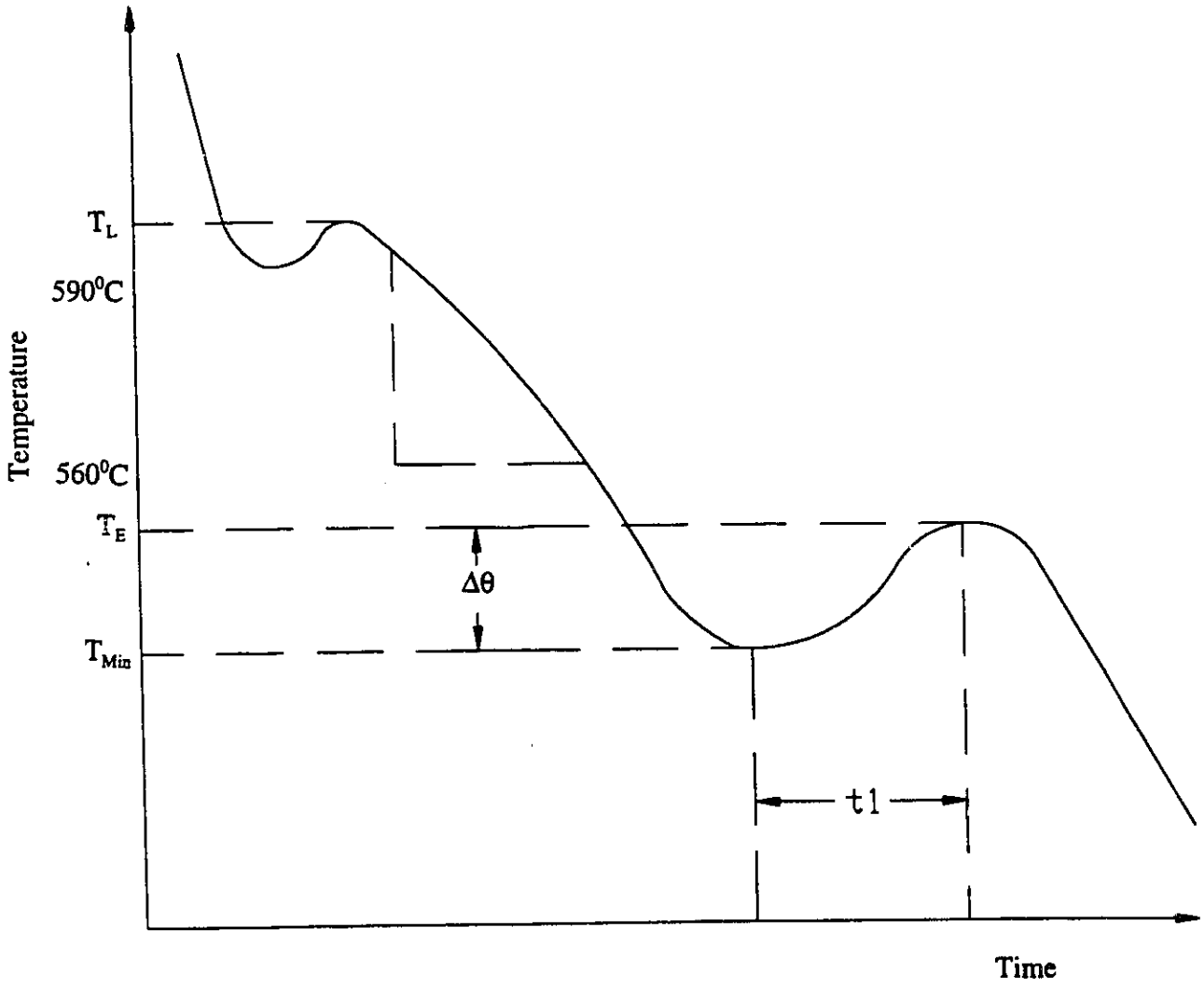

Fig.4.1 A schematic characteristic thermal analysis curve showing cooling rate parameters.

- Eutectic Arrest Temperature (T_E): the maximum temperature achieved during the eutectic arrest event.
- T_{Min}: the temperature at the minimum before the eutectic arrest.
- Eutectic Undercooling ($\Delta\theta=T_E-T_{Min}$): the difference between the minimum temperature and the eutectic arrest temperature.
- Undercooling Time (t1): the time from the maximum undercooling until the maximum eutectic arrest temperature.
- ΔT: change in Eutectic Arrest Temperature resulting from microalloying element, and $\Delta T = T_{E(\text{base alloy})} - T_{E(\text{microallyed base alloy})}$.

The following cooling and cooling rate curves (Fig.4.2 - Fig.4.7) shows the change of the liquidus temperature, eutectic arrest temperature and undercooling for the A356 alloy with the addition of the microalloying elements. These measurements are summarized in Table 4.1, and indicate the level of modification in the melt microalloying elements exert. The error in instrument measurement of temperatures (T_L, T_E, etc.) is $\pm 0.1^0$C. First, it is evident that the addition of a microalloying element increases the nucleation temperature of α-Al dendrite phase (T_L increases). Also the addition of microalloyed elements has lowered the eutectic arrest temperature (T_E), with which the modification of Al-Si eutectic structure is associated. A further effect of the Sb and Bi microalloying elements is the increase in the eutectic undercooling. For A356 base alloy there is essentially no undercooling ($\Delta\theta = 0$), while the addition of Sb and Bi increases $\Delta\theta$ to 2.92^{0}C (1.0% Sb) and 1.61^{0}C (1.0% Bi), respectively. The In and Sn additions had little or no effect on $\Delta\theta$. The eutectic reaction is lengthened (t1 increases) considerably when Sb and Bi are added, but not for In and Sn addition.

Table 4.1 Thermal analysis parameters measured from cooling curves

Alloy	T_L (^{0}C)	T_E (^{0}C)	T_{min} (^{0}C)	$\Delta\theta=T_E-T_{Min}$ (^{0}C)	t1 (s)	ΔT (^{0}C)
A356	612.6	575.2	575.2	0.00	0.00	
A356+0.5%Sb	613.7	572.4	570.4	2.0	49.6	2.8
A356+1.0%Sb	618.0	574.5	571.6	2.9	48.0	0.7
A356+1.0%Bi	616.7	571.3	569.7	1.6	35.6	3.9
A356+1.0%In	615.6	573.4	573.4	0.00	0.00	1.8
A356+1.0%Sn	615.8	574.1	574.0	0.1	3.1	1.1

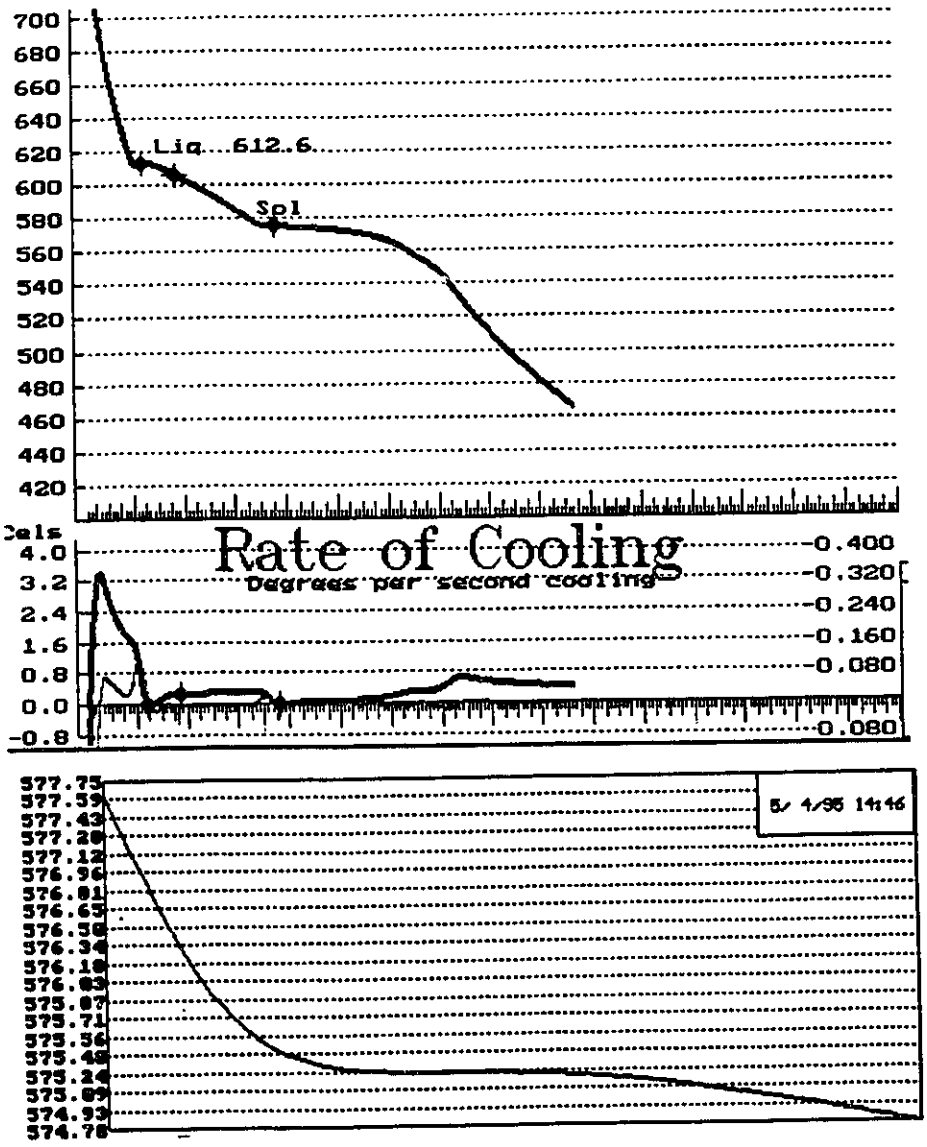

Fig.4.2 Thermal analysis of A356 base alloy

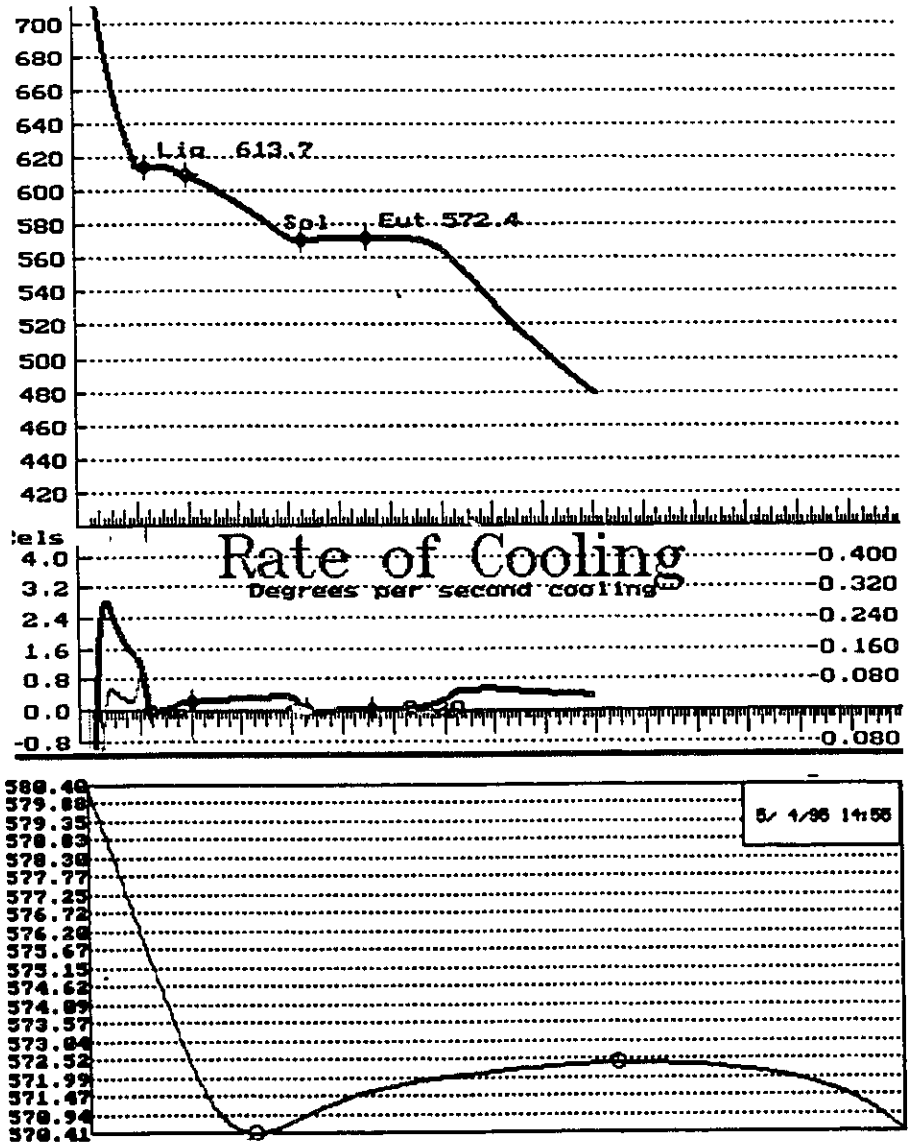

Fig.4.3 Thermal analysis of alloy A356 + 0.5% Sb

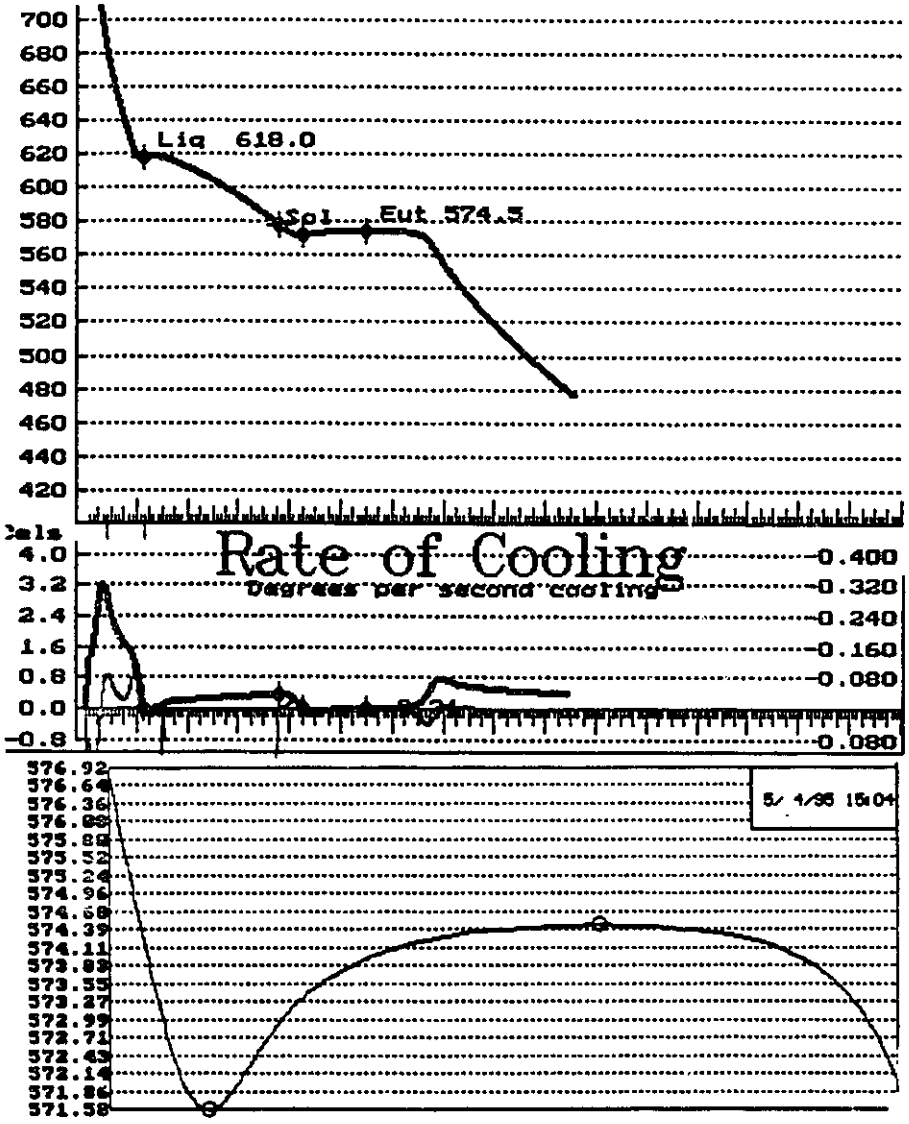

Fig.4.4 Thermal analysis of alloy A356 + 1.0% Sb

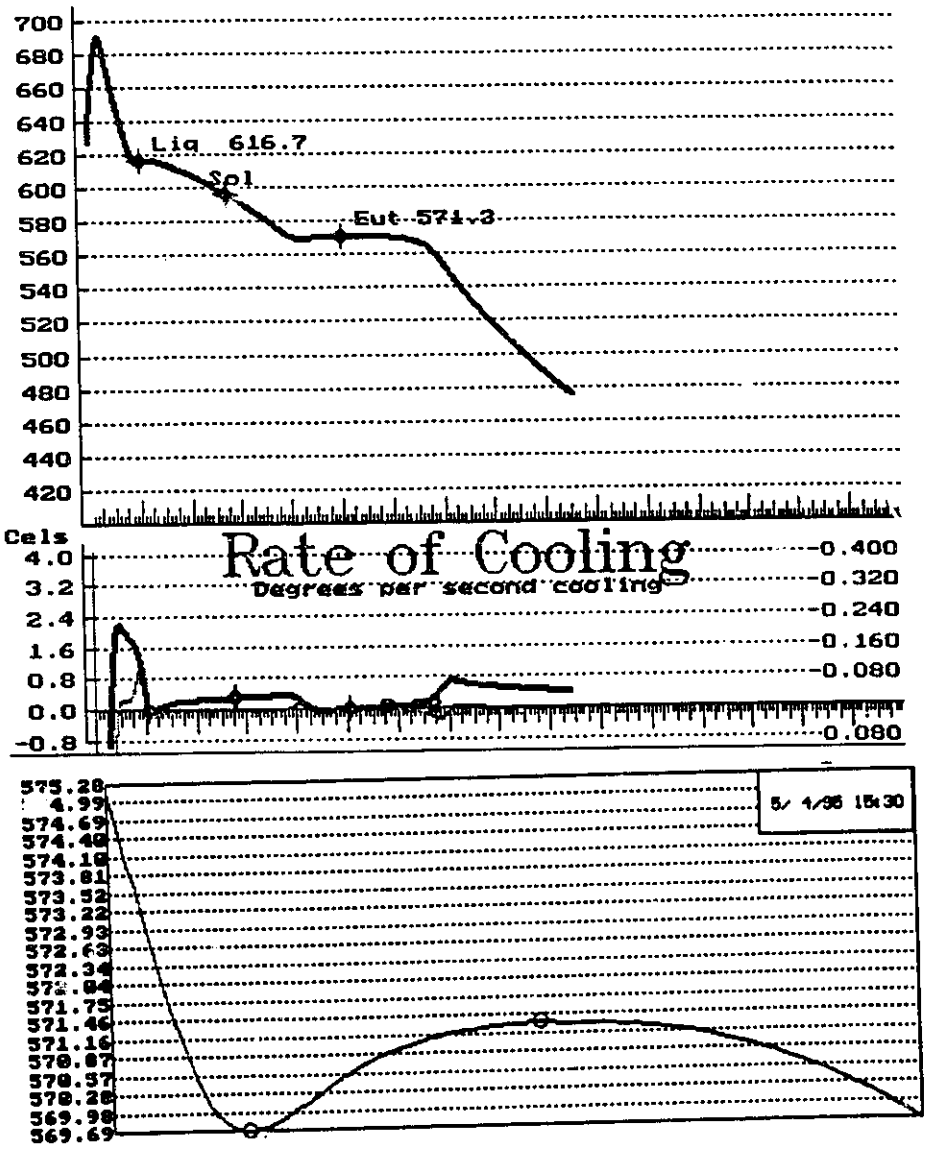

Fig.4.5 Thermal analysis of alloy A356 + 1.0% Bi

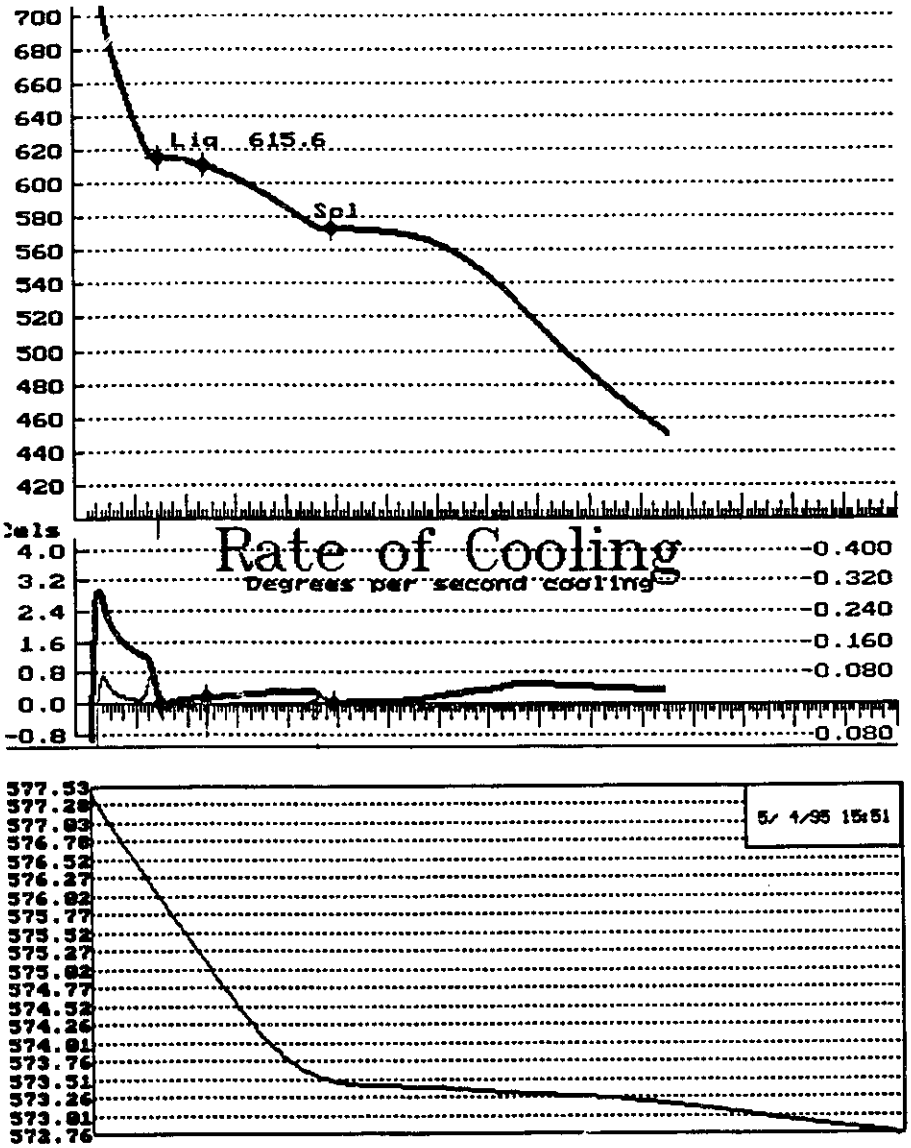

Fig.4.6 Thermal analysis of alloy A356 + 1.0% In

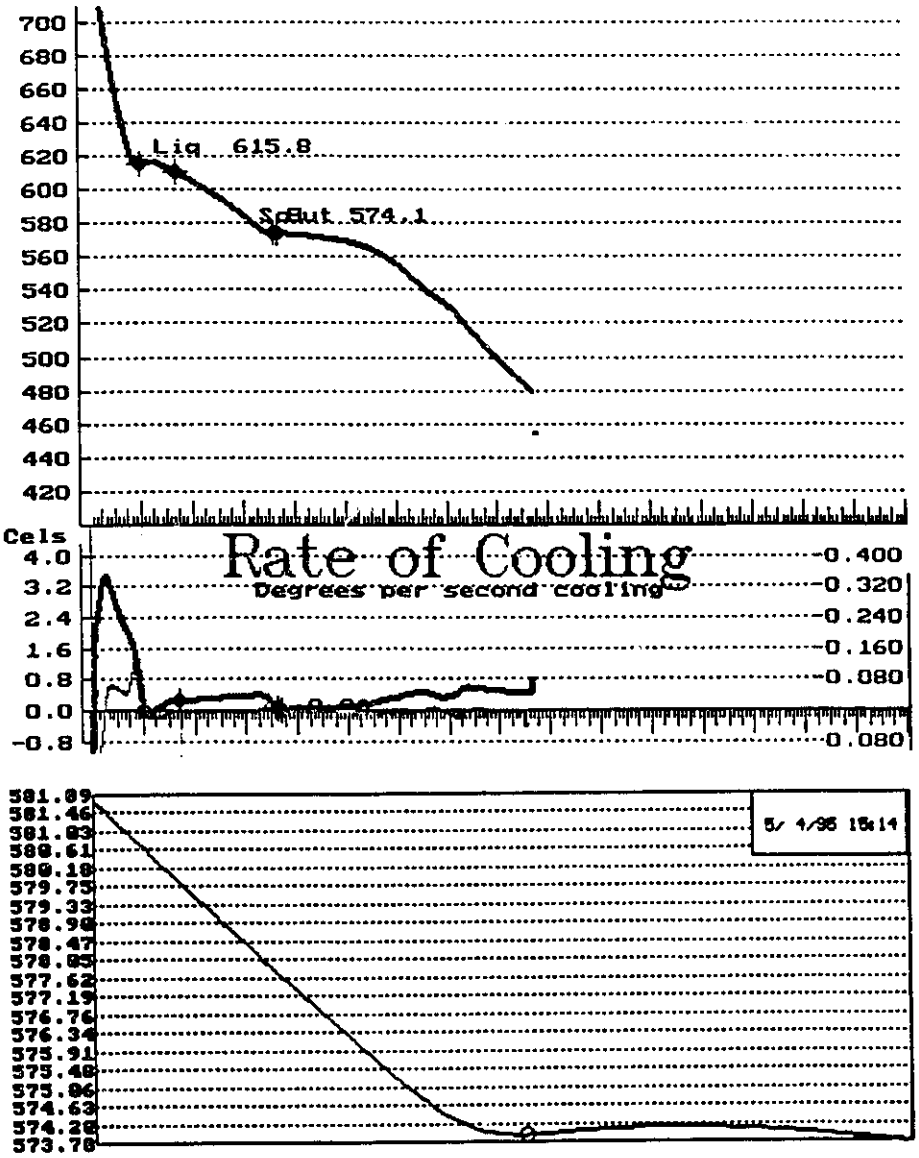

Fig.4.7 Thermal analysis of alloy A356 + 1.0% Sn

4.2 MICROSTRUCTURE

4.2.1 Fast Cooling Rate (4.0°C/s)

Fig.4.8(a) shows the photomicrograph of the base alloy A319, solidified at a cooling rate of 4.0°C/s. The solidification microstructures of the A319 alloys microalloyed using additions of pure Sb, Bi, In and Sn are shown in Fig.4.8(b) - (f). The addition of 1.0%Sb and 1.0%Bi to the A319 alloy reduced significantly the dendrite arm spacing (DAS), with the 1.0%Sb addition giving the most refinement, decreasing the DAS approximately 50% (from ~29μm for the base alloy to ~15μm). The dendrite arm spacing, as measured by using the line intercept method, are given in Table 4.2. The In and Sn additions show little or no significant reduction in the DAS values. Fig.4.9(a) and (b) shows the SEM micrographs of the base alloy A319 and the base alloy with the 1.0% pure Sb addition. The phases identified in the micrographs are the eutectic Si phase, the Cu-rich phase ($CuAl_2$), a Mn-rich phase, and the Sb-rich phase (AlSb), which were determined using the X-ray map analysis.

In the second phase of the investigation, the microalloying elements were added as Al master alloys containing 10% of the microalloying element. The procedure was introduced to minimize the risk of some loss of the microalloying addition during alloying through entrapment in the melt surface oxide of the base alloy. The as-cast microstructure at higher magnification for A319 and A319 containing 0.5% Sb and 1.0% Sb are shown in Fig.4.10, 4.11, and 4.12 respectively. It is evident that the Sb additions significantly decreases the DAS, and modifies the eutectic Si structure, from a relatively coarse to a much finer structure in which the Si particles have tended towards spheroidization. Fig.4.13 shows

that Bi has much the same effect on Si morphology and DAS (Table 4.2) as Sb. A comparison of the higher magnification micrographs for ingots containing 1.0% In and 1.0% Sn (Fig.4.14, 4.15) with the base alloy (Fig.4.10) shows no significant refinement of the eutectic Si phase. Table 4.3 gives the DAS results for the A319 and A356 alloys microalloyed using master alloy additions. The results for the A319 alloys agree with those of Table 4.2 (within standard deviation). It is evident that the microalloying additions to A356 tend to decrease the DAS, however, the decrease is not statistically significant. The A356 alloy differ from A319 in higher Mg content and lower Cu content (see Table 2.1). The presence of a significant amount of Mg in A356 (up to 0.45% vs <0.1% in A319) may be the cause for the ineffectiveness of some of the microalloying elements on DAS. In the case of Sb, for which Mg has a strong affinity, the Sb may be precipitated out as Mg_3Sb_2 prior to its interfacial segregation role during solidification. The effect of the microalloying elements on eutectic Si morphology in the A356 alloy (see Fig.4.16 to Fig.4.21) is similar to that for A319 alloy in the case of Sb, i.e. Sb significantly refine the Si particle, and promotes spheroidization (cf. Fig.4.16 and Fig.4.18). In also significantly refines the Si (see Fig.4.20) in A356, unlike that in A319, in which In had little effect on Si particle modification.

The refinement of the dendritic structure in the commercial Al alloy castings (A319, A356) containing the microalloying element (Sb and Bi) may be attributed to their thermal and constitutional supercooling effects during solidification, which are the result of the extremely low distribution coefficients of the elements in Al. Since the microalloying elements used here all have extremely low distribution coefficients k_0 (see Table 4.2), the rejection of the insoluble element (Sb) by the growing Al base dendrites rapidly increases the

concentration of the microalloying element (Sb) to high levels in the interfacial liquid. In a fluctuating growth velocity, due to varying temperature and composition conditions resulting from convective flow effects, the interfacial liquid concentration profile can take on a Gaussian form, which is concave downward in the interface region (Fig.2.13). The Gaussian distribution of the solute element will force an inverse Gaussian distribution for the solvent metal, which is the major solidifying component. So the concentration gradient of the principal solidifying element (C_A) decreases, which slows down the solidification rate and rate of latent heat release. However, temperature gradients that were established in the solid for the faster solidification rate will persist, thus forcing the temperature of the interface to drop, i.e. thermal and constitutional supercooling will be significantly increased. According to L-M theory (Eq. 2-39), the short wavelength λ_s of a perturbation will decrease with the increase in thermal undercooling ΔT, promoting secondary arm development on the primary dendrite stalks, and thus refining significantly the dendrite structure [46,47]. It can be seen from Table 4.2 that the microalloying element with the lowest distribution coefficient element is not the most effective in refining the dendrite structure.

The possible effect of an increasing diffusivity with the insoluble elements in the interfacial liquid requires some consideration. It was shown that when the diffusivity increase with concentration, an "uphill" diffusive transport will contribute to developing a Gaussian concentration distribution in the interfacial liquid (cf. Eq.2-46, Fig.2.12). The concentrations at which "uphill diffusion" occur in the binary alloy system, are calculated in Appendix A. The result of the calculations shows that "uphill" diffusion will occur in the binary Al alloys when

when

$$C_{Sb} >= 14 \text{ at\%}$$

$$C_{Bi} >= 16 \text{ at\%}$$

$$C_{In} >= 18 \text{ at\%}$$

$$C_{Sn} >= 27 \text{ at\%}$$

It is interesting to note that the order in which $\partial D_c / \partial C_c > 0$ is Sb first, followed by Bi, In, and Sn, and this is the order of effectiveness in the refinement of dendrites in the A319 alloy. However, too much can't be read into this agreement, since the distribution coefficient has a much larger effect in the build-up of insoluble element concentration at the solid-liquid interface, and Sb does not have the lowest distribution coefficient of the above elements. The presence of the other alloying elements will also alter the distribution coefficients. Also, surface energy effects may have a significant, and possibly even a controlling effect, in determining solidification microstructure for some of the alloys.

4.2.2 Slow Cooling Rate (0.3^0C/s)

The effect of cooling rate on microstructure was investigated for the A356 alloy only. Fig.4.22 - 4.27 show the microstructure of the base A356 alloy and the alloys containing the microalloying elements (added via the master alloys) solidified at a cooling rate of 0.3^0C/s. It is observed from Fig.4.22 and 4.24 that the most pronounced change resulting from the slower solidification (cooling) rate is the morphology of the eutectic Si particle. Fig.4.22 shows that the shape of eutectic Si particles in A356 base alloy is coarse and faceted (unmodified), and with the addition of 1.0% Sb and 1.0% Bi the Si particle takes on a much

finer and lamellar-like structure (modified), i.e. Si needles become thinner, shorter and more closely and uniformly spaced (see Fig.4.24, 4.25). Fig.4.23 show that less Sb addition (0.5%) results in less refinement of the Si, i.e. the effect is concentration dependent. In and Sn additions have very little effect on the coarse and faceted eutectic silicon structure (Fig.4.26, 4.27). The modification of Si eutectic in Al-Si hypoeutectic alloy with Sb addition has been reported by other investigators [48,49,53]. This modification may be related to a change in Si growth mode [51,52], which is evident in the result of the thermal analysis, i.e. Si eutectic undercooling increases with the Sb or Bi addition (see Table 4.1).

The effect of the slower cooling rate on the dendrite growth is to significantly increase the DAS. Although no DAS measurements are available, the coarse dendritic structure is evident when comparing the microstructures of the fast and slow solidified base alloy ingots (cf. Fig.4.16 to Fig.4.22). The increase of dendrite refinement is expected, since the degree of constitutional supercooling increases [50] with cooling (solidification) rate (see Eq.2-11).

Table 4.2 Dendrite arm spacing for A319, pure element additions
cooling rate = 4.0^0C/s

Alloy	Partition coefficient of element (k_0)	Dendrite arm spacing (μm)
A319 BASE		29.05 ± 7.45
A319 + 0.5% Sb	$k_{Sb}^{Al(l)} < 0.001$	23.87 ± 5.15
A319 + 1.0% Sb	$k_{Sb}^{Al(l)} < 0.001$	15.12 ± 4.44
A319 + 1.0% Bi	$k_{Bi}^{Al(l)} < 0.00035$	17.57 ± 4.30
A319 + 1.0% In	$k_{In}^{Al(l)} < 0.00055$	27.42 ± 5.02
A319 + 1.0% Sn	$k_{Sn}^{Al(l)} < 0.00035$	28.14 ± 4.93

Table 4.3 Dendrite arm spacing for A319 and A356 alloys, master alloy additions
cooling rate = 4.0^0C/s

addition element (using master alloy)	A319 alloy Dendrite arm spacing, μm	A356 alloy Dendrite arm spacing, μm
BASE	29.61 ± 6.05	37.93 ± 8.98
0.5% Sb	20.02 ± 5.42	32.43 ± 8.67
1.0% Sb	18.33 ± 4.28	24.79 ± 6.61
1.0% Bi	24.27 ± 5.48	36.26 ± 8.85
1.0% In	26.16 ± 4.74	27.83 ± 7.77
1.0% Sn	26.21 ± 5.63	30.10 ± 7.91

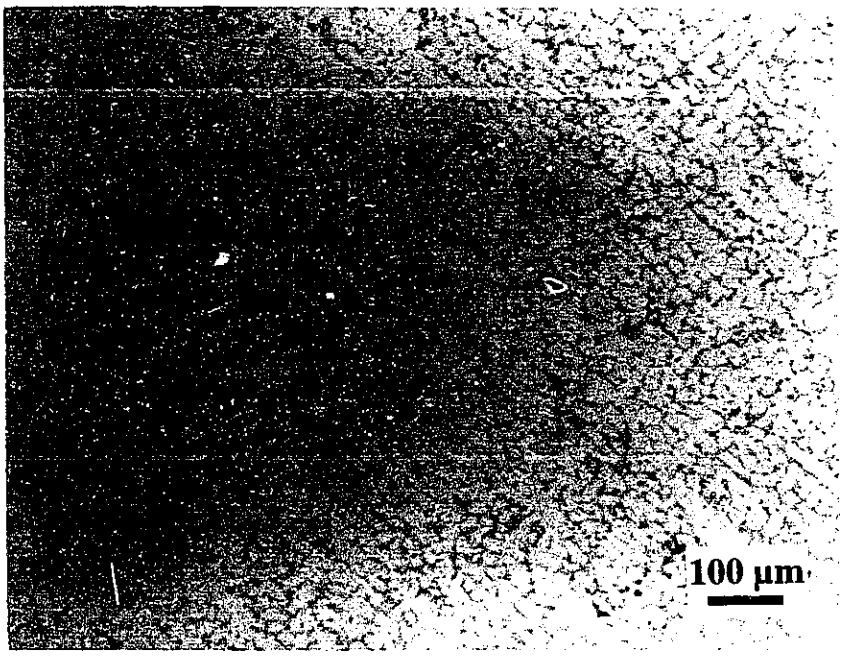

(a) × 100

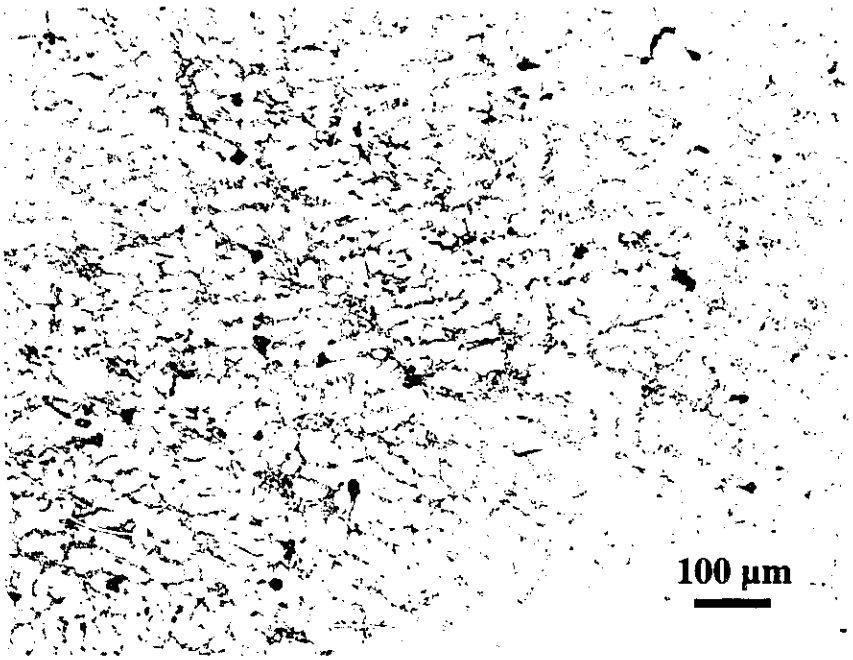

(× 100

Fig.4.8 (a) A319 base; (b) A319 + 0.5%Sb.

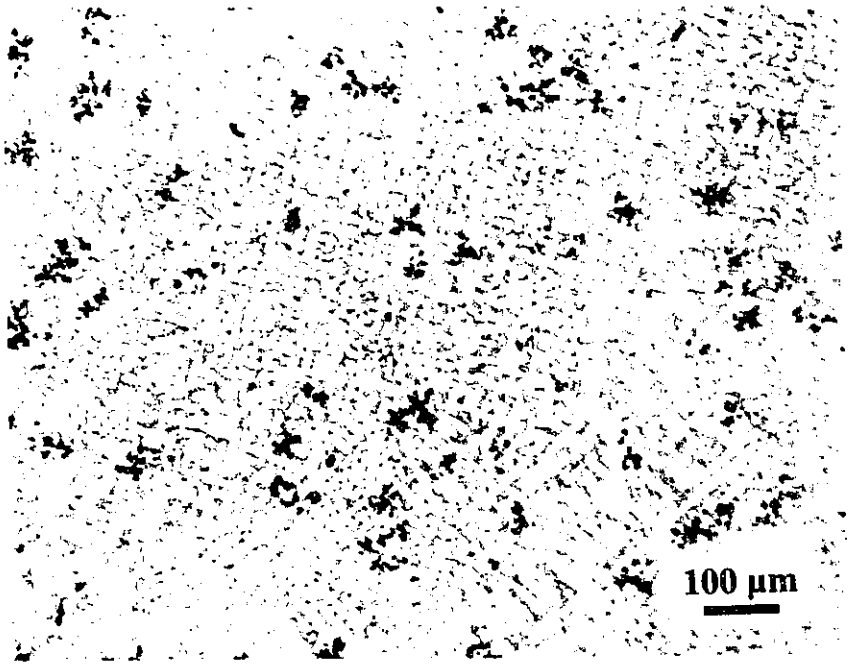

(c) × 100

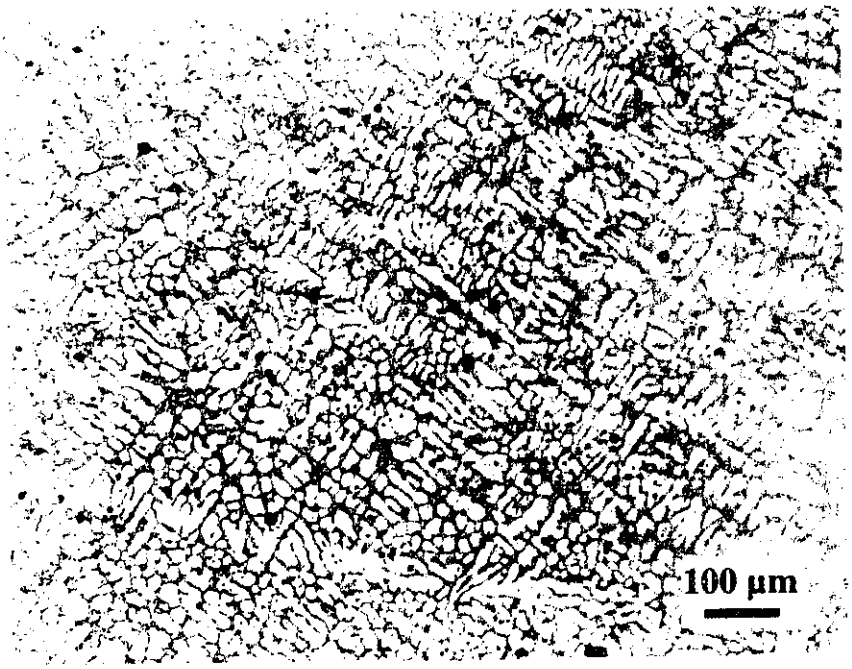

(d) × 100

Fig.4.8 (c) A319 + 1.0% Sb ; (d) A319 + 1.0% Bi.

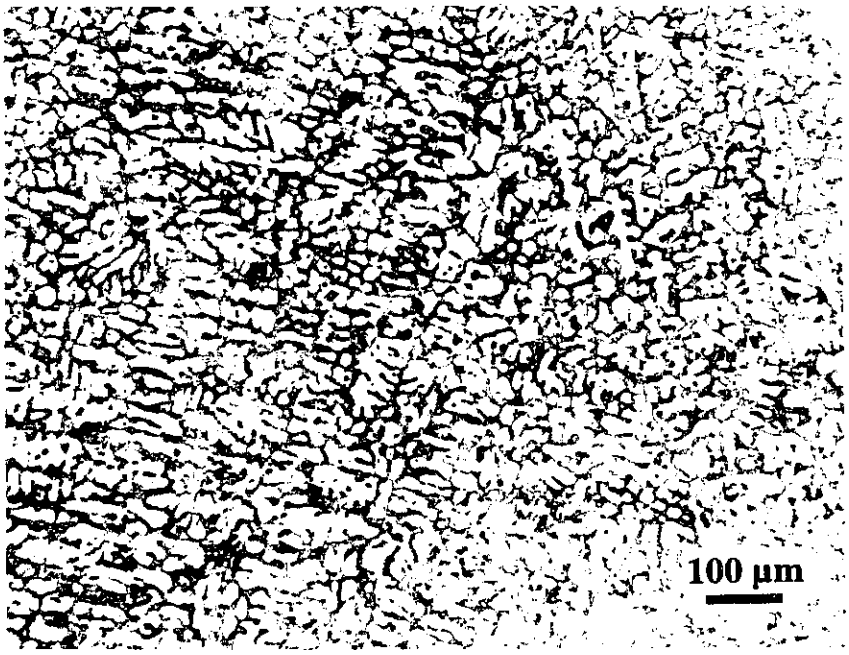

(e) × 100

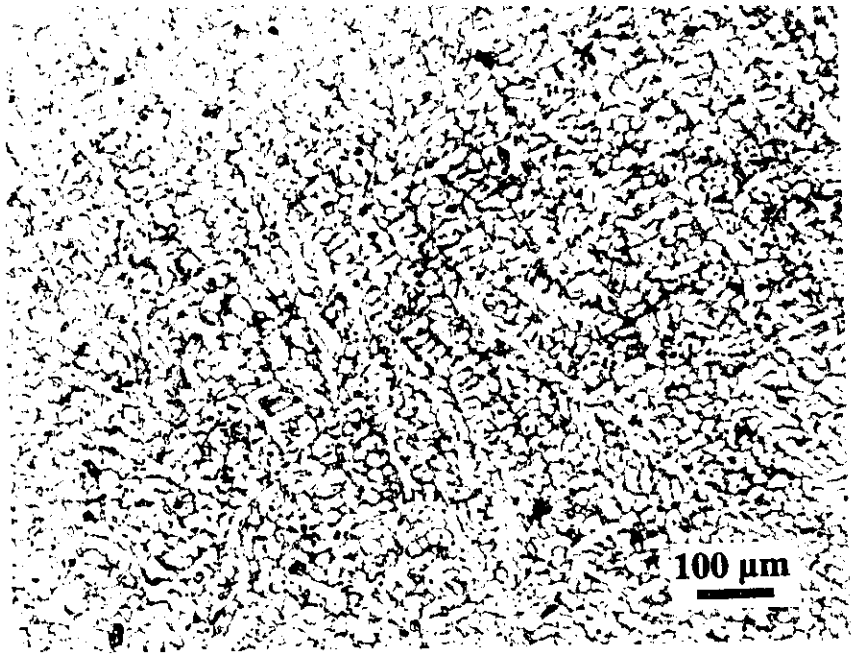

(f) × 100

Fig.4.8 Optical micrographs showing dendrite refinement by the addition of pure microalloying elements; (a) A319 base; (b) A319 + 0.5% Sb; (c) A319 + 1.0%Sb; (d) A319 + 1.0% Bi; (e) A319 + 1.0% In; and (f) A319 + 1.0% Sn (Cooling Rate = 4.0^0C/s).

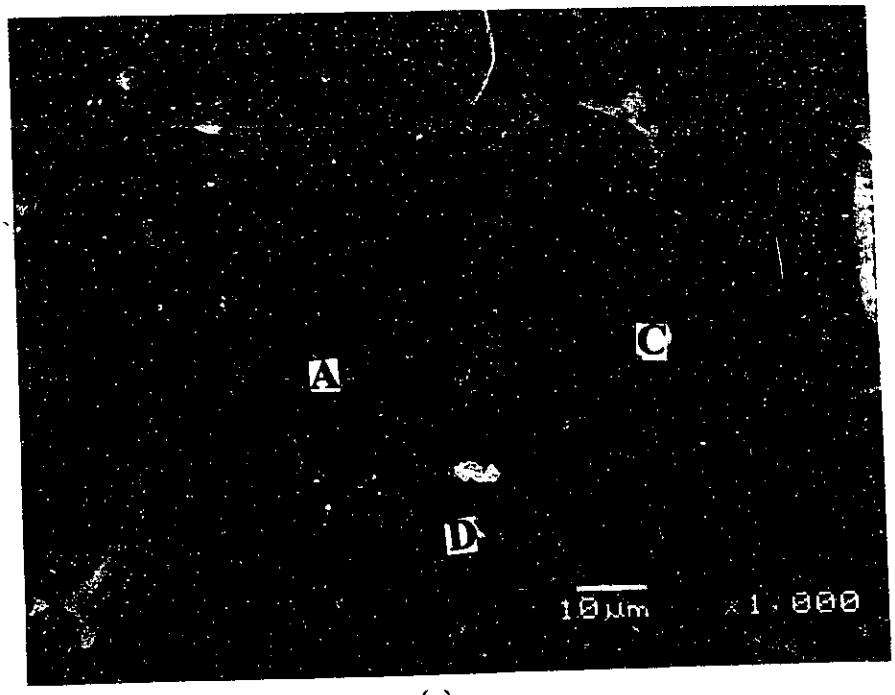

(a)

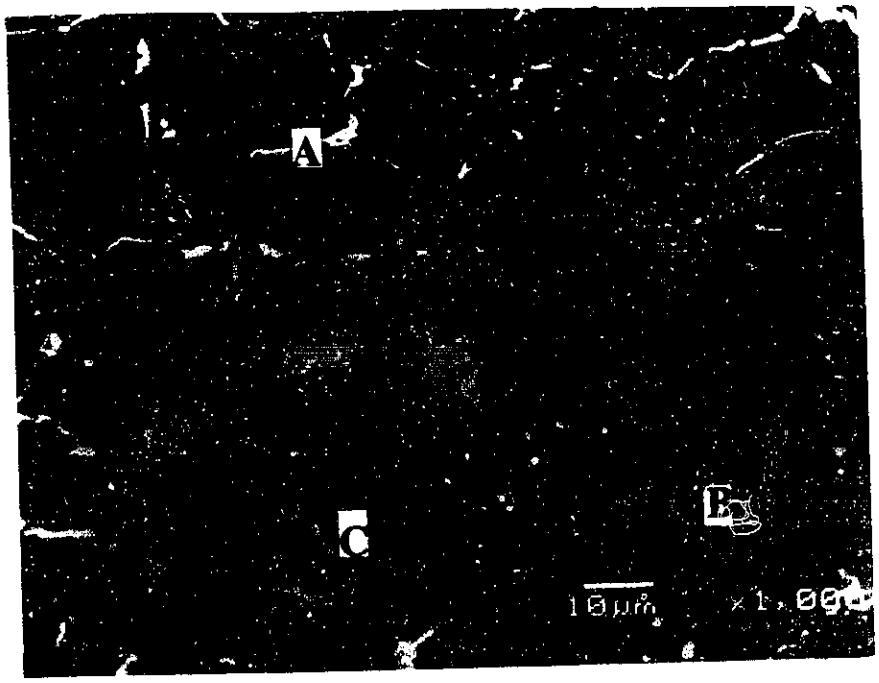

(b)

Fig.4.9 SEM micrographs showing the distribution of each element in (a) A319 base alloy; and (b) alloy A319+1.0% pure Sb. **'A'**, Cu rich region; **'B'**, Sb rich phase; **'C'**, Si rich phase; **'D'**, Mn rich region (Cooling rate 4.0^{0}C/s).

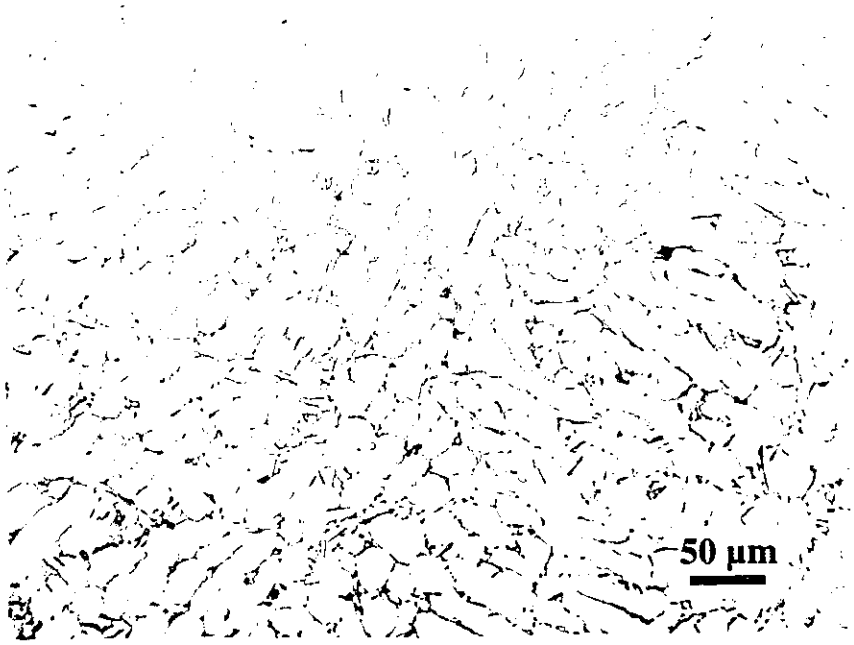

× 200

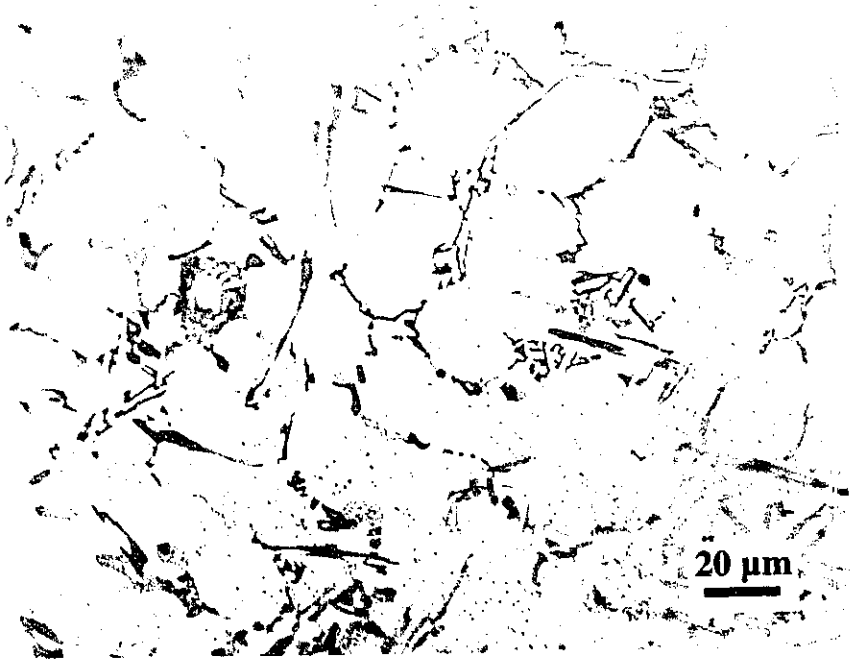

× 500

Fig.4.10 As-cast microstructure for A319 base alloy, cooling rate = 4.0°C/s.

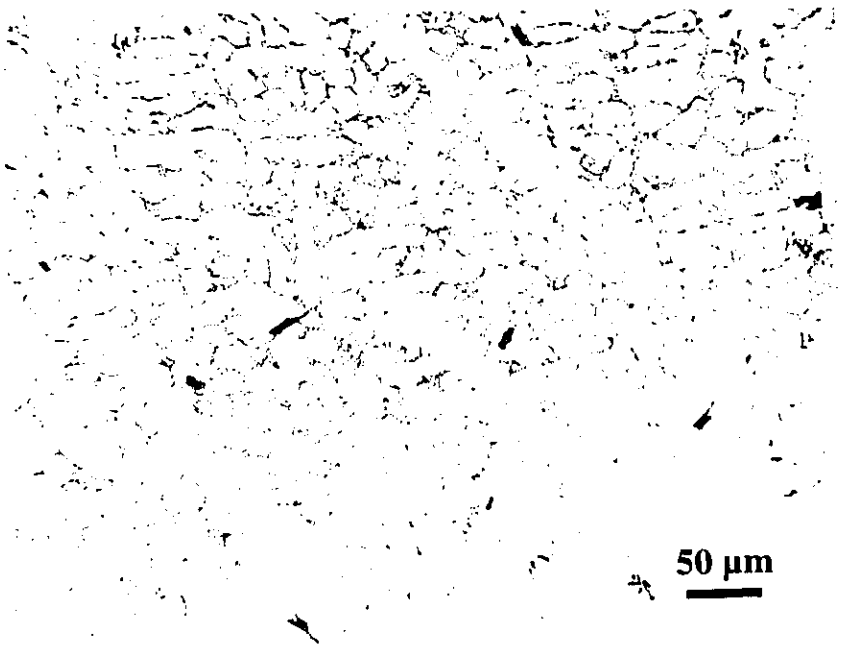

× 200

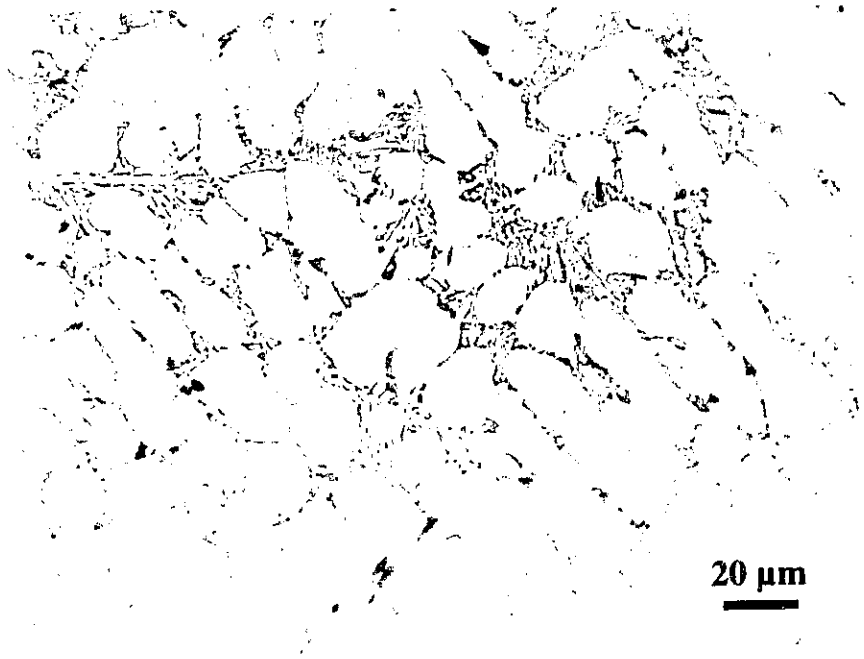

× 500

Fig.4.11 As-cast microstructure for alloy A319 + 0.5% Sb, cooling rate = 4.0°C/s.

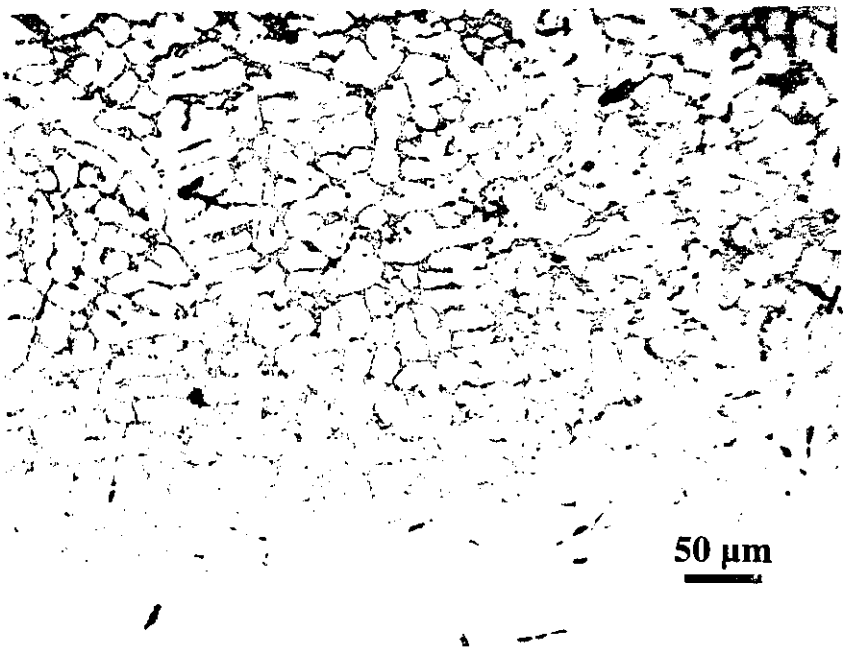

× 200

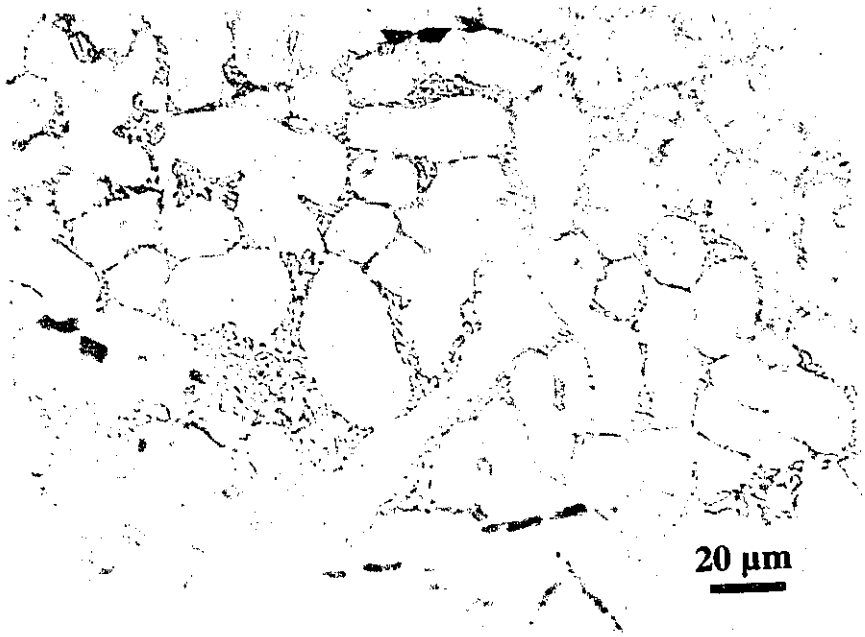

× 500

Fig.4.12 As-cast microstructure for alloy A319 + 1.0% Sb, cooling rate = 4.0°C/s.

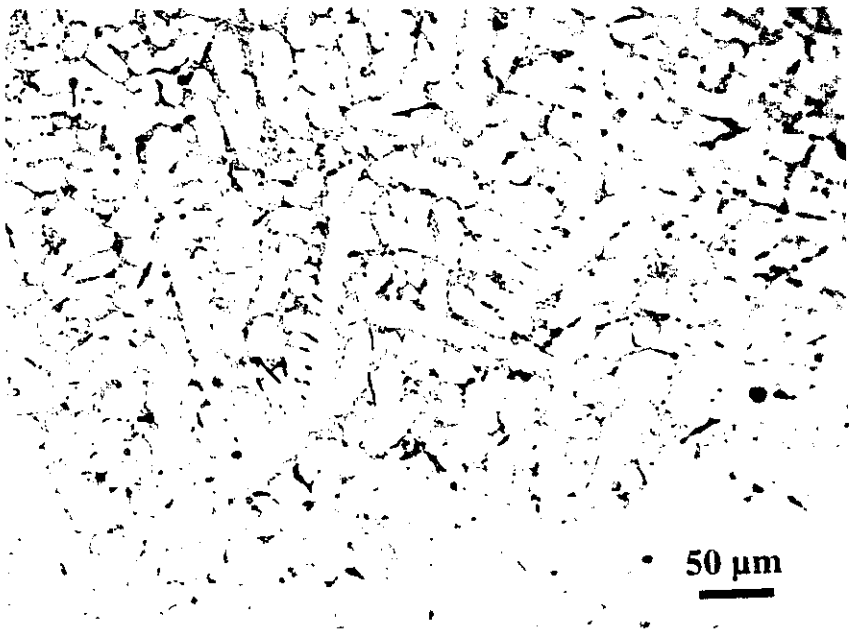

× 200

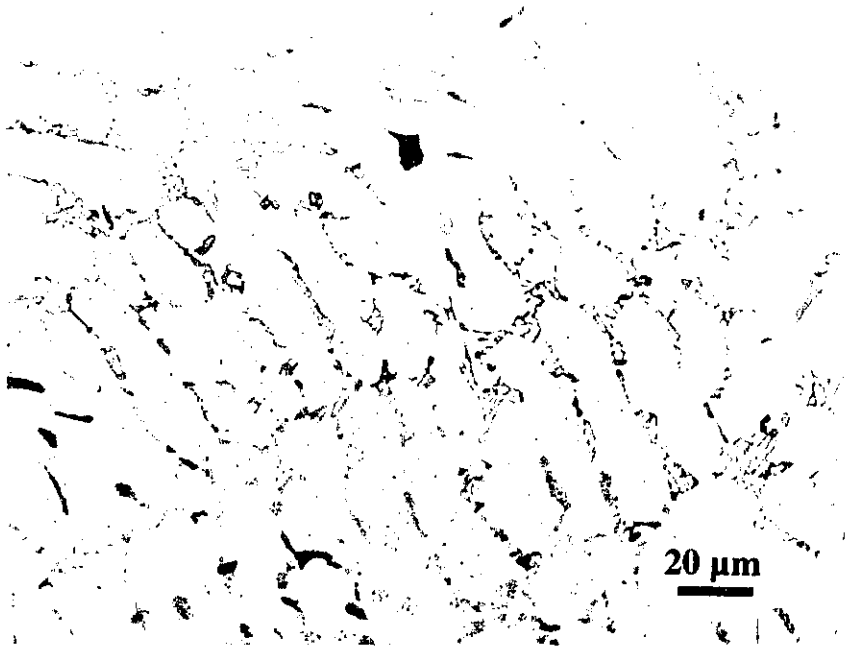

× 500

Fig.4.13 As-cast microstructure for alloy A319 + 1.0% Bi, cooling rate = 4.0°C/s.

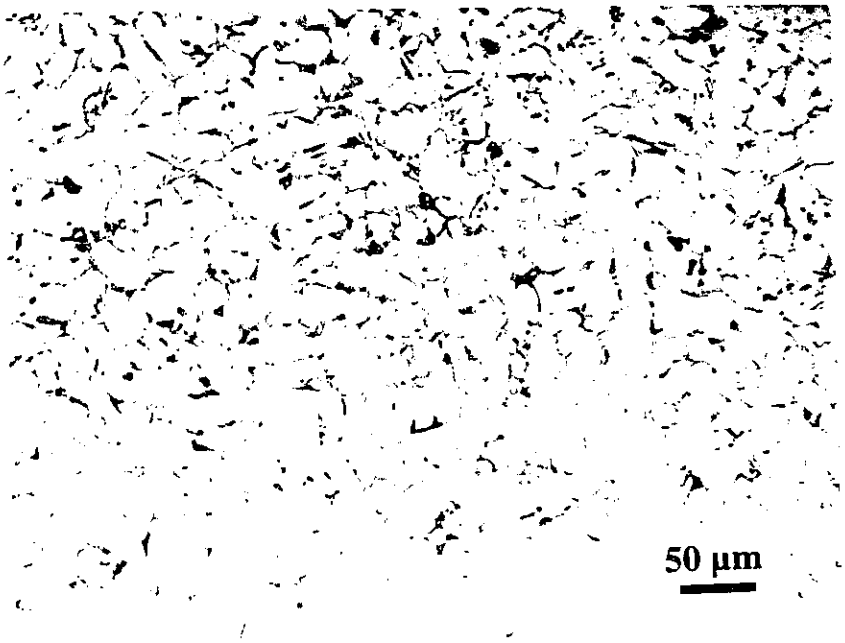

× 200

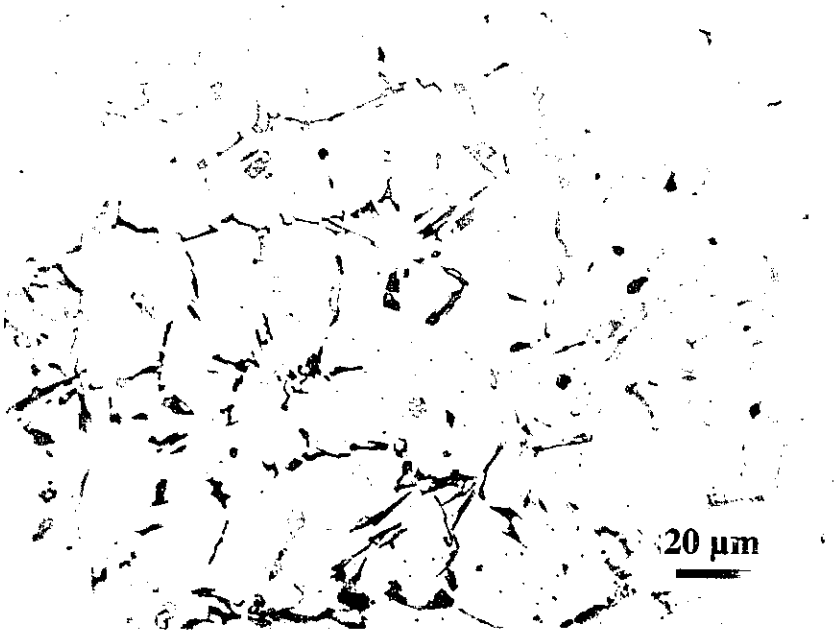

× 500

Fig.4.14 As-cast microstructure for alloy A319 + 1.0% In, cooling rate = 4.0°C/s.

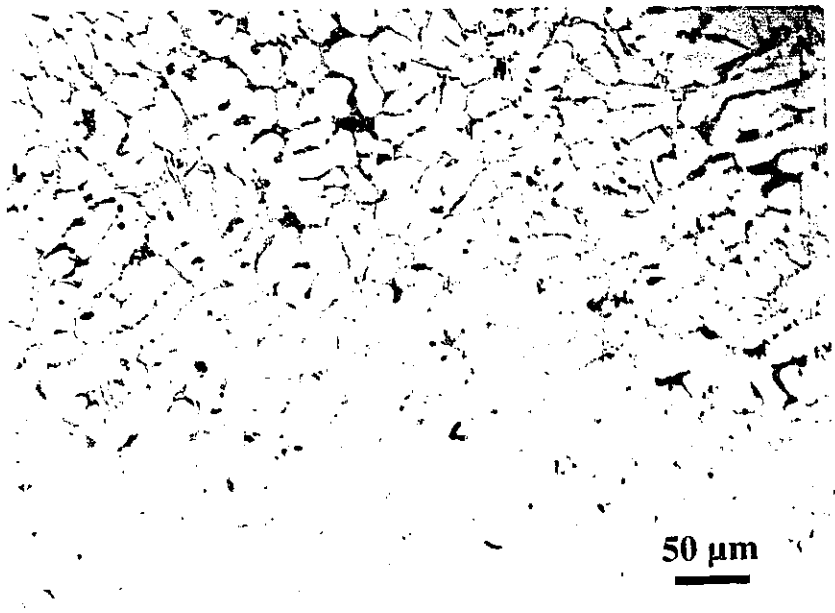

× 200

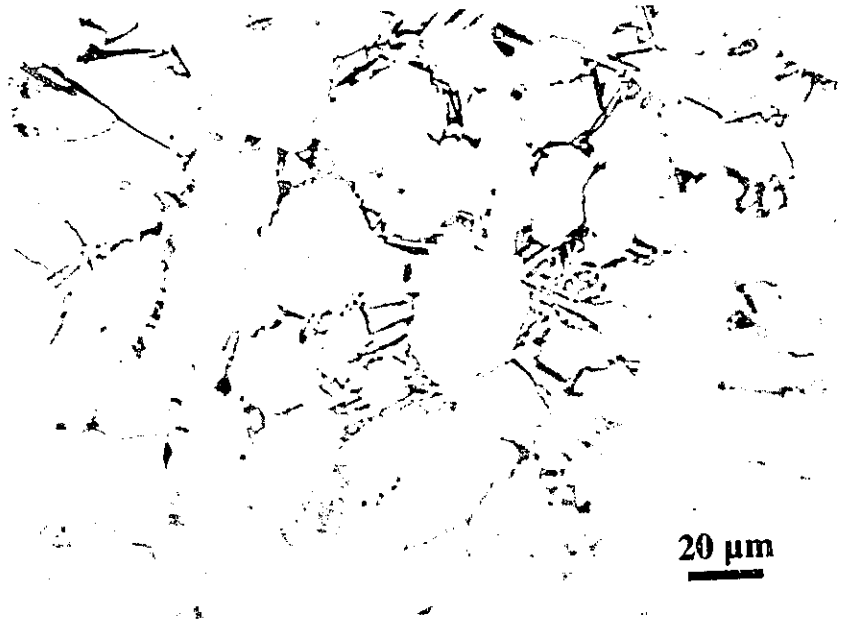

× 500

Fig.4.15 As-cast microstructure for alloy A319 + 1.0% Sn, cooling rate = 4.0°C/s.

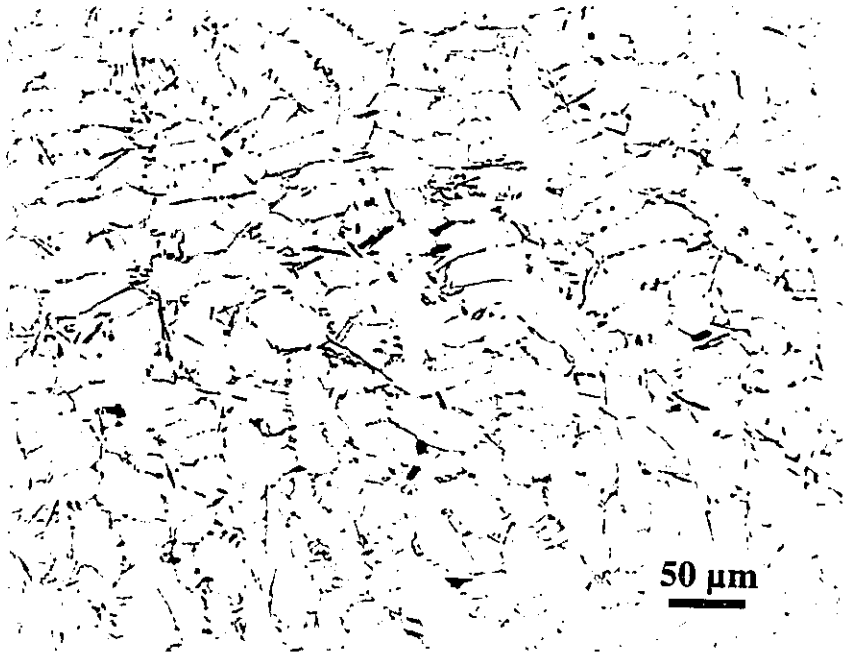

× 200

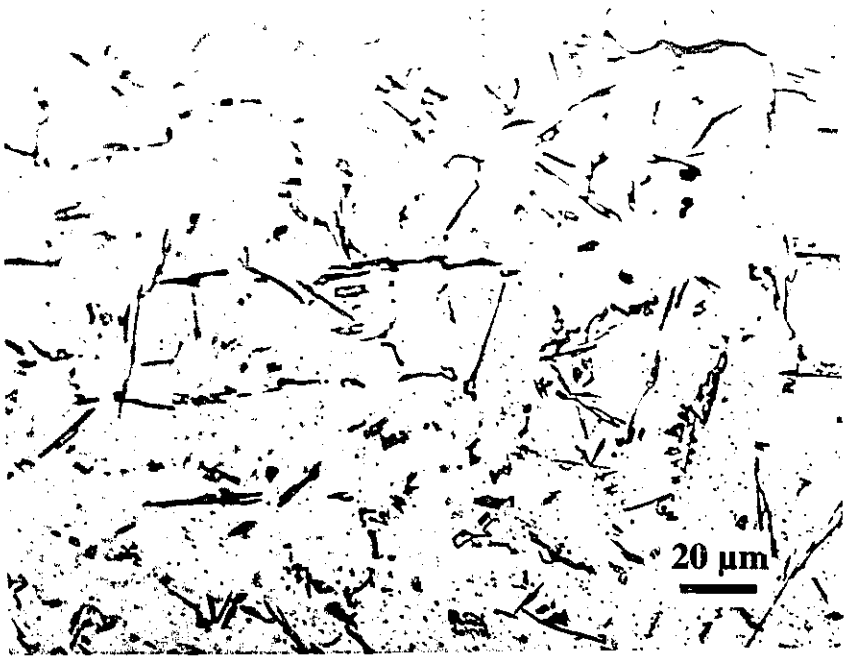

× 500

Fig.4.16 As-cast microstructure for A356 base alloy, cooling rate = 4.0°C/s.

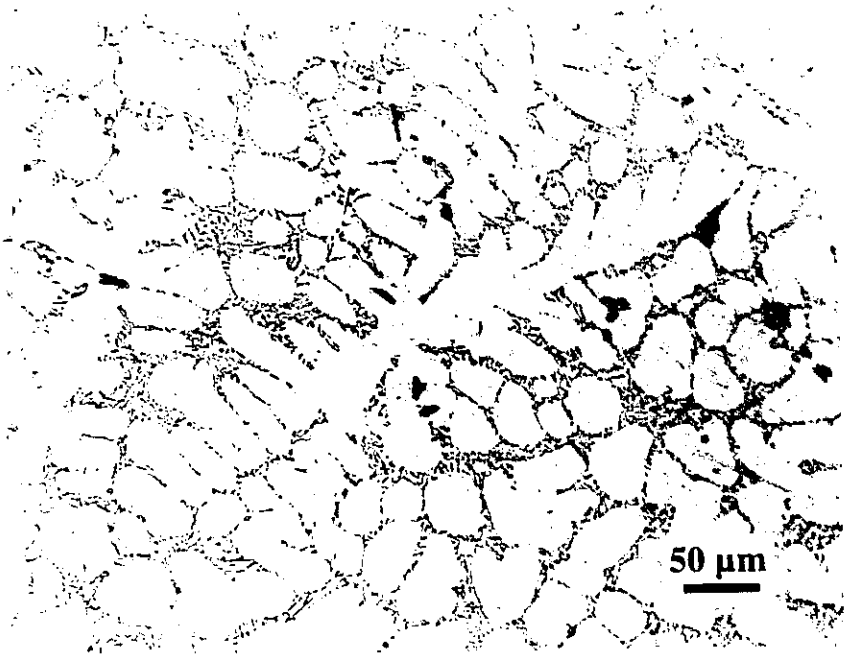

× 200

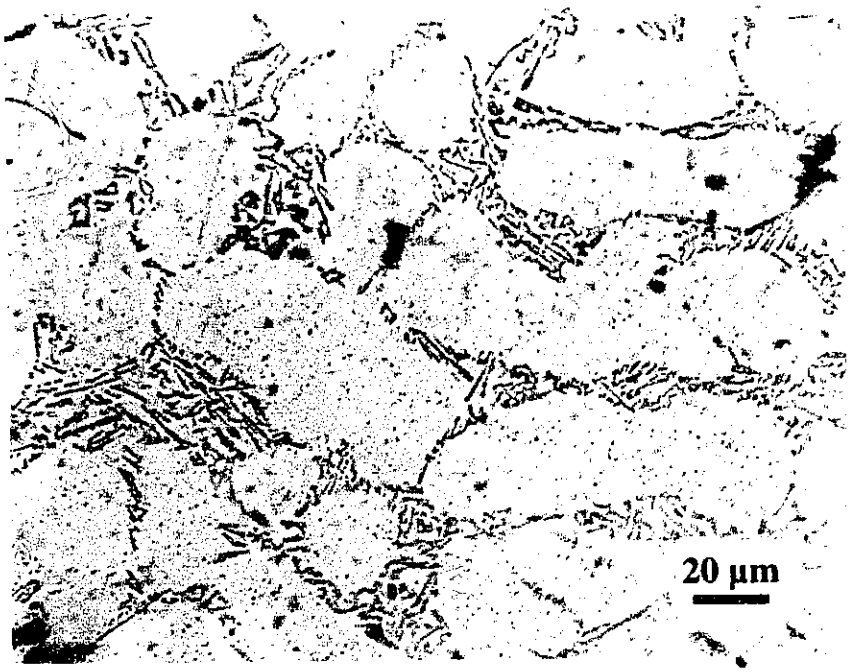

× 500

Fig.4.17 As-cast microstructure for alloy A356 + 0.5% Sb, cooling rate = 4.0°C/s.

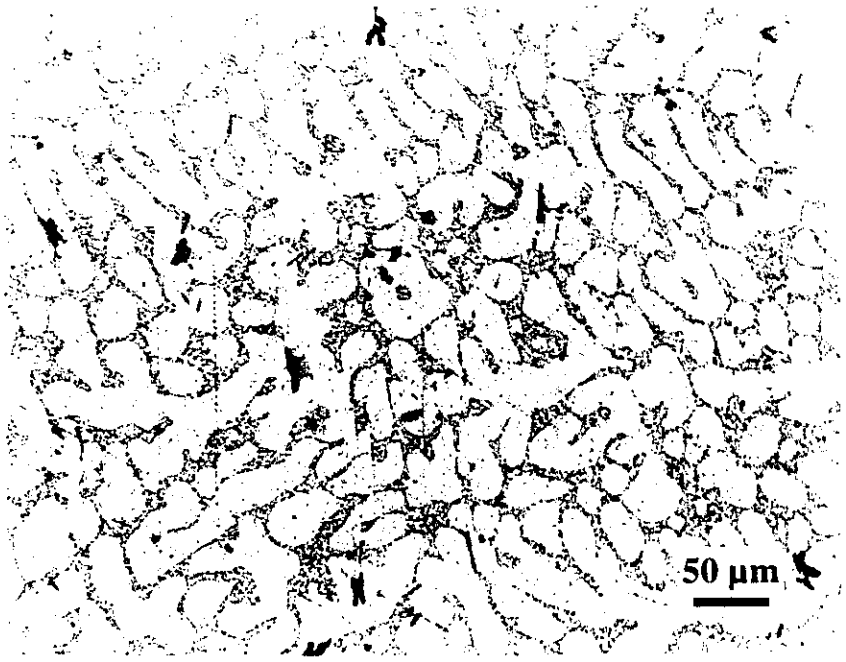

× 200

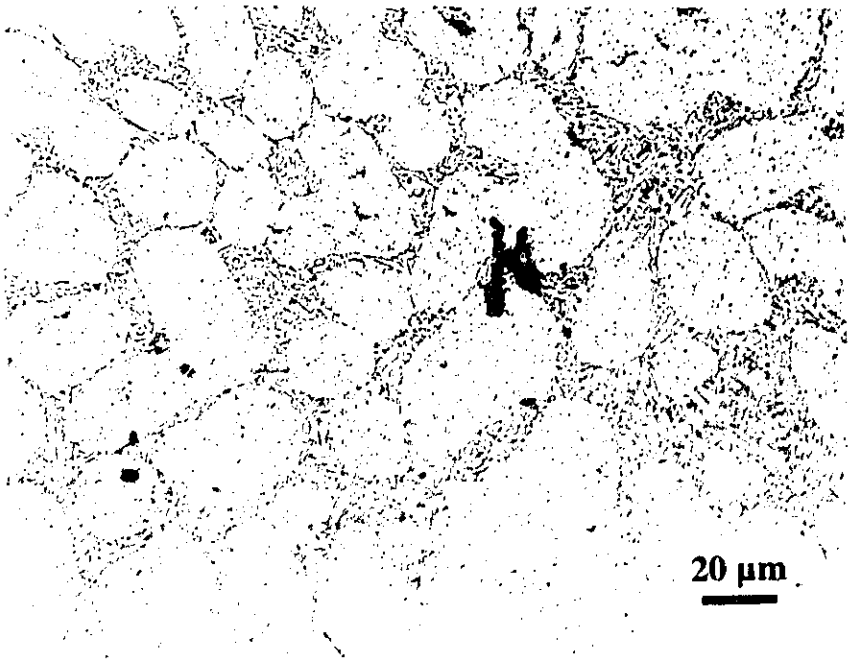

× 500

Fig.4.18 As-cast microstructure for alloy A356 + 1.0% Sb. cooling rate = 4.0°C/s.

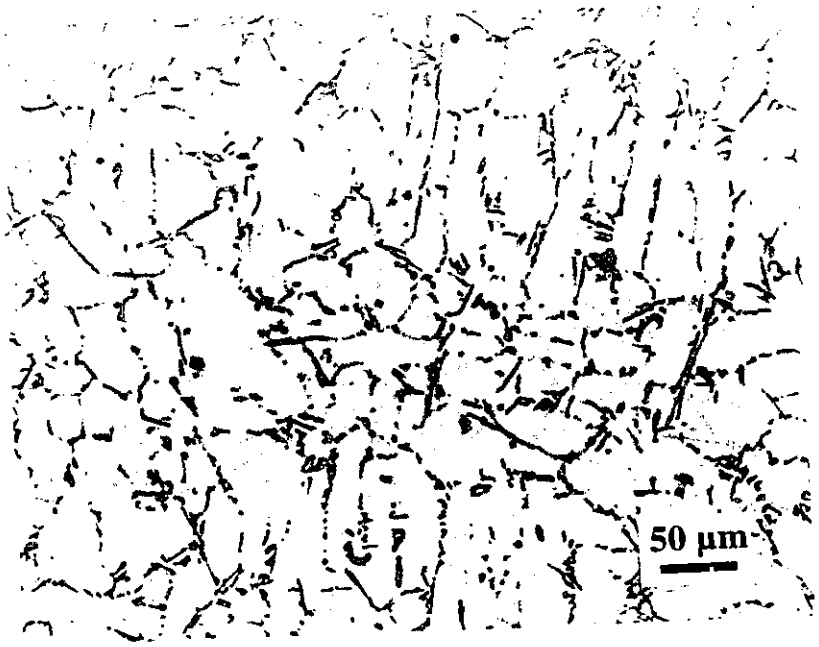

× 200

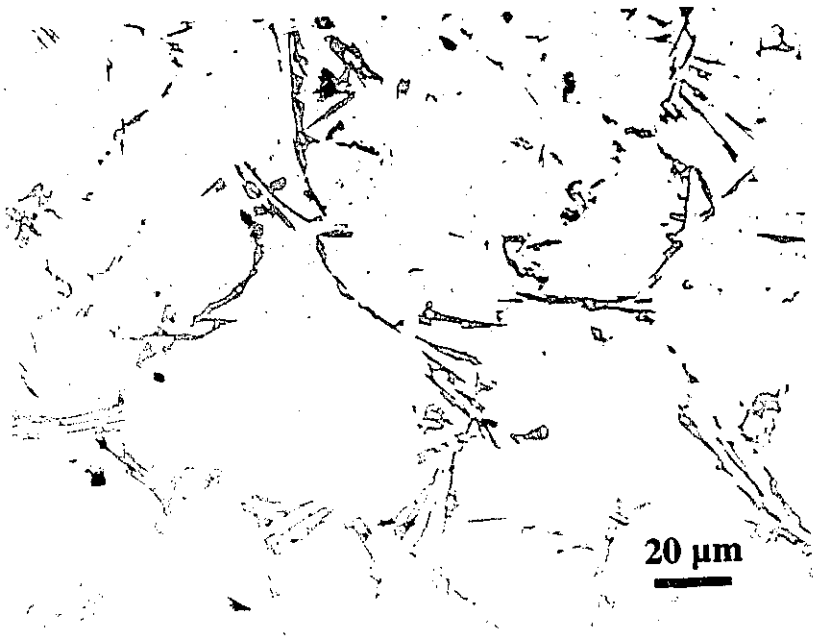

× 500

Fig.4.19 As-cast microstructure for alloy A356 + 1.0% Bi, cooling rate = 4.0°C/s.

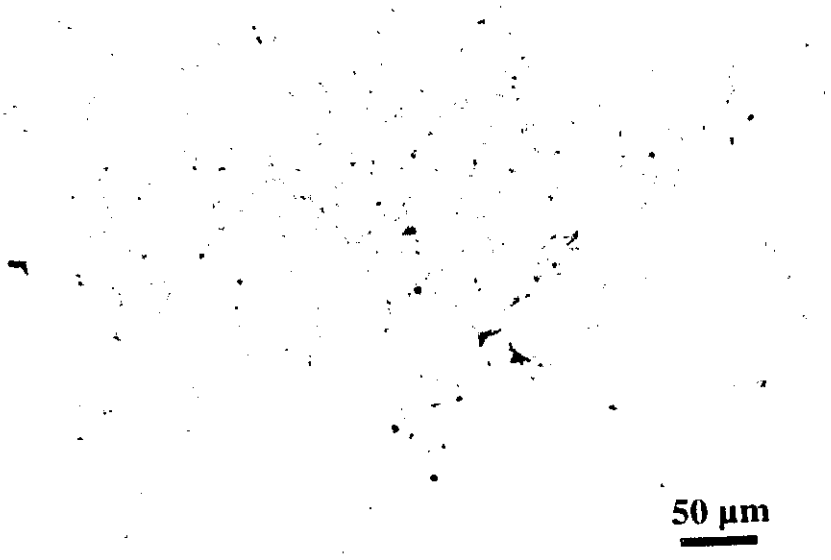

× 200

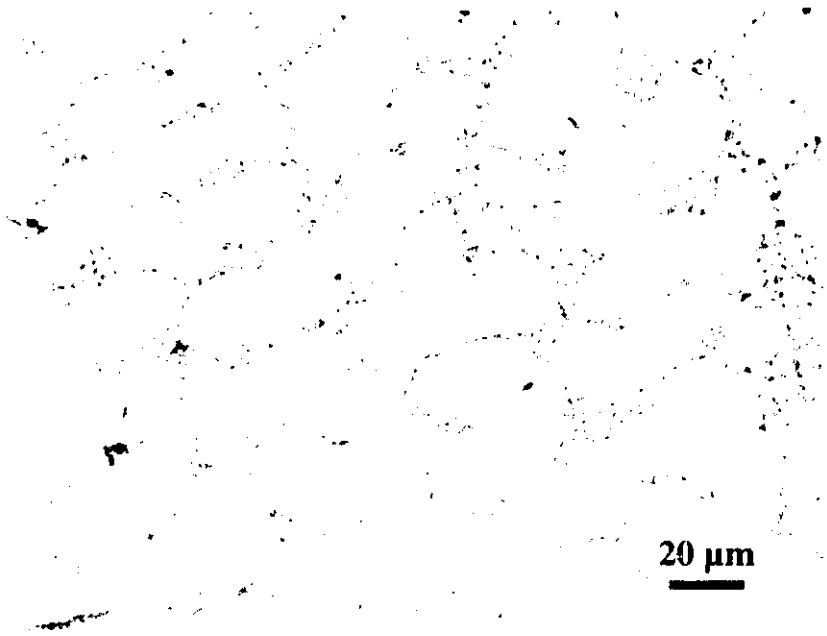

× 500

Fig.4.20 As-cast microstructure for alloy A356 + 1.0% In, cooling rate = 4.0°C/s.

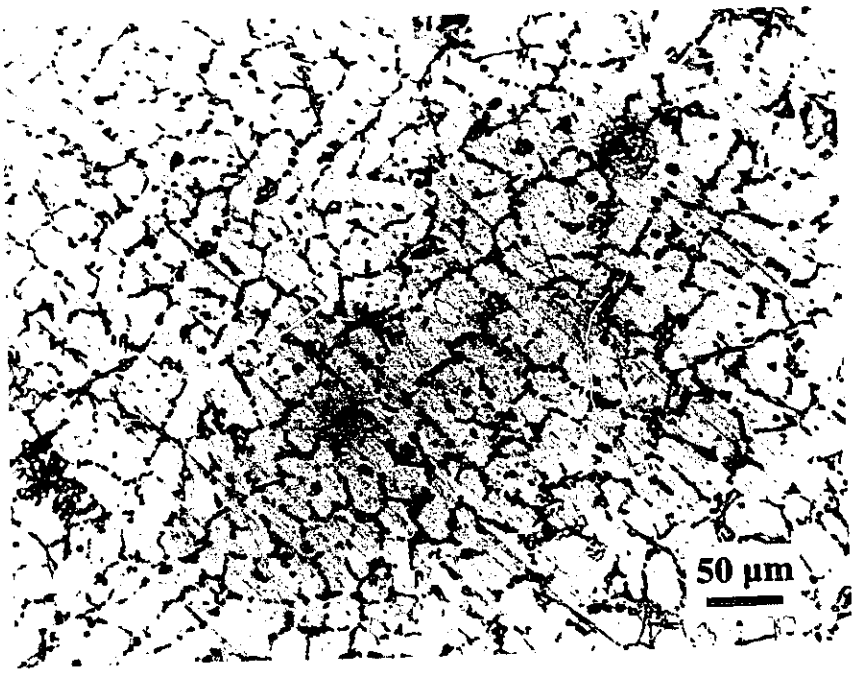

× 200

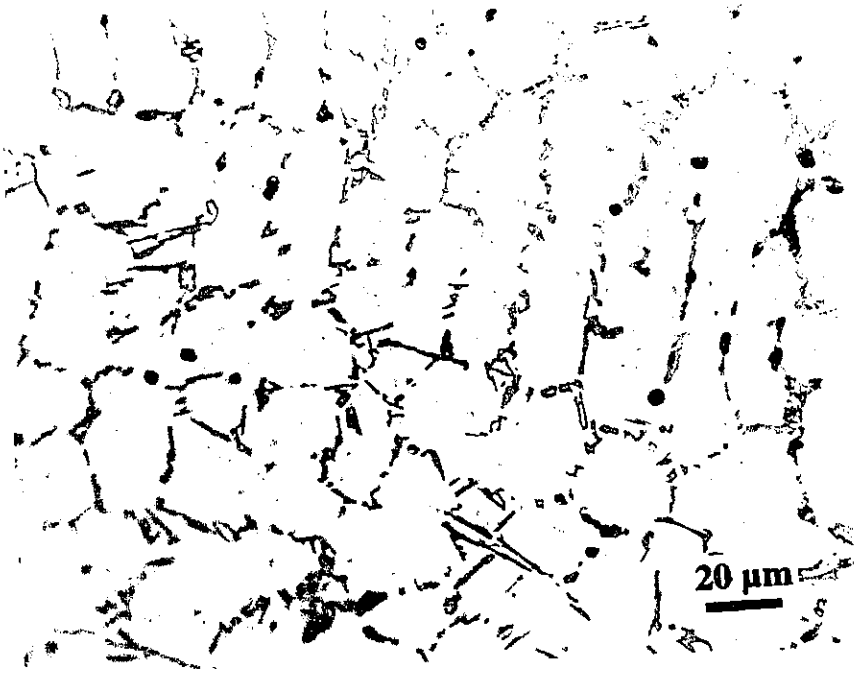

× 500

Fig.4.21 As-cast microstructure for alloy A356 + 1.0% Sn, cooling rate = 4.0°C/s.

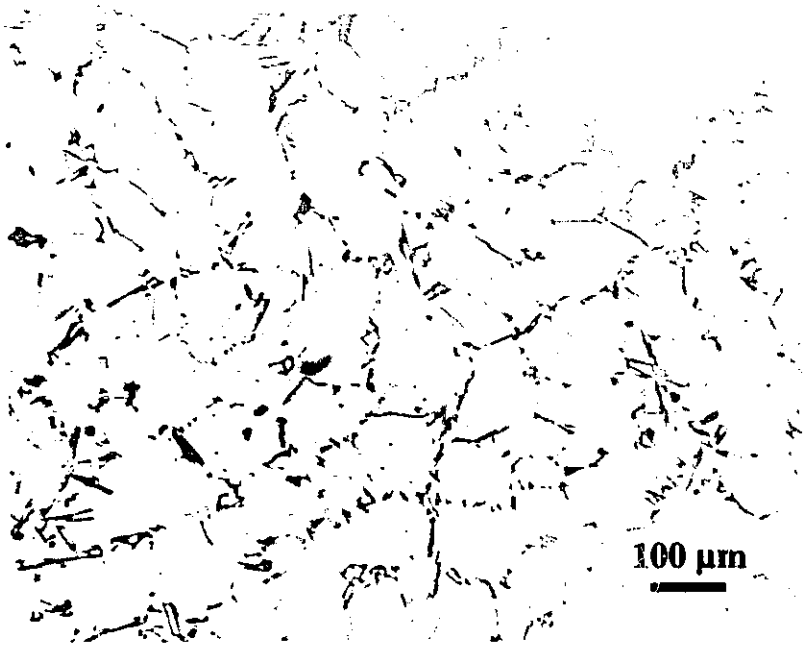

× 100

× 500

Fig.4.22 As-cast microstructure for A356 base alloy, cooling rate = 0.3°C/s.

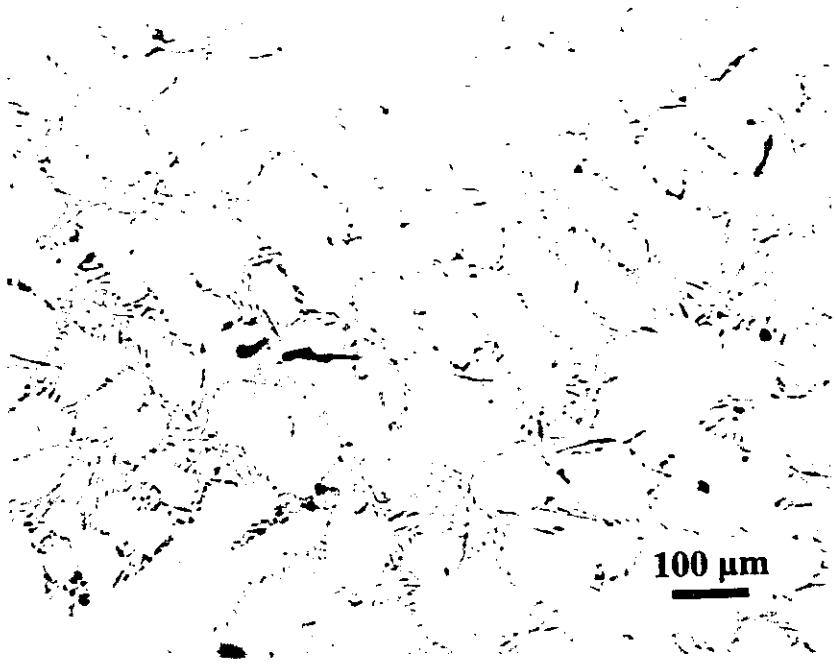

× 100

× 500

Fig.4.23 As-cast microstructure for alloy A356 + 0.5% Sb, cooling rate = 0.3°C/s.

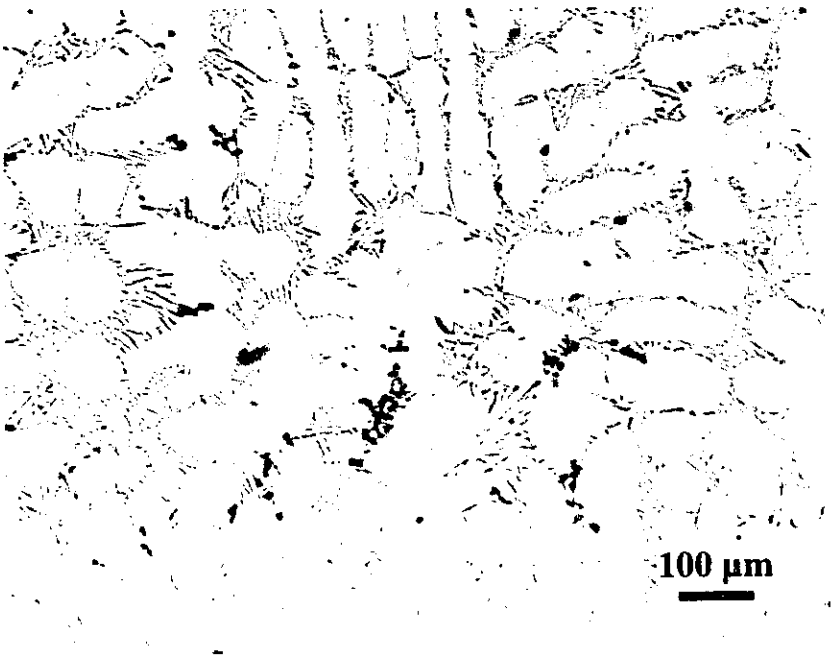

× 100

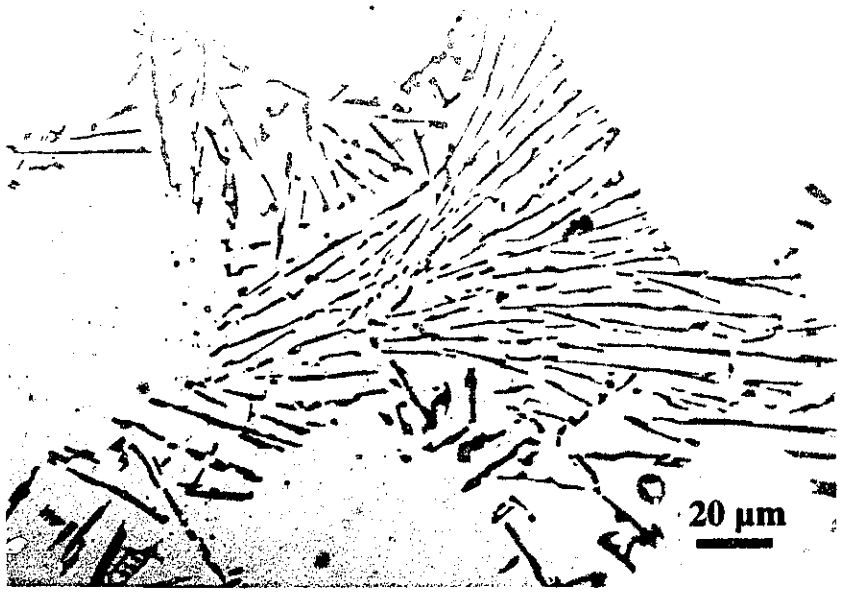

× 500

Fig.4.24 As-cast microstructure for alloy A356 + 1.0% Sb, cooling rate = 0.3°C/s.

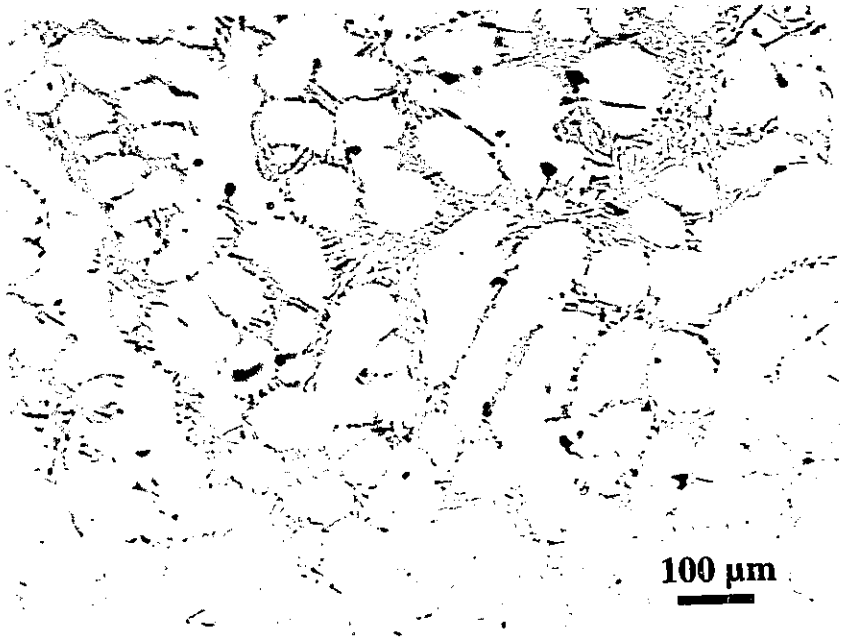

× 100

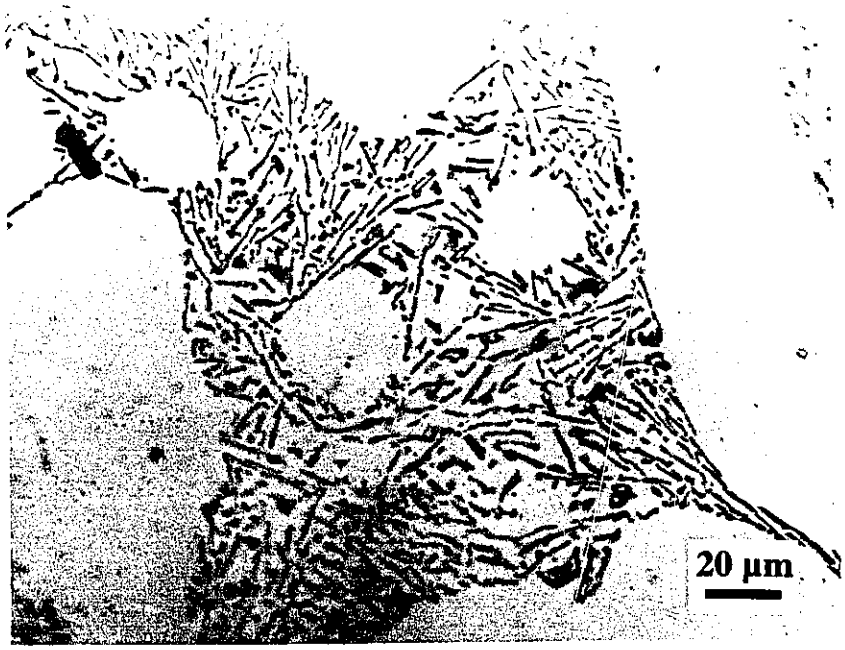

× 500

Fig.4.25 As-cast microstructure for alloy A356 + 1.0% Bi, cooling rate = 0.3°C/s.

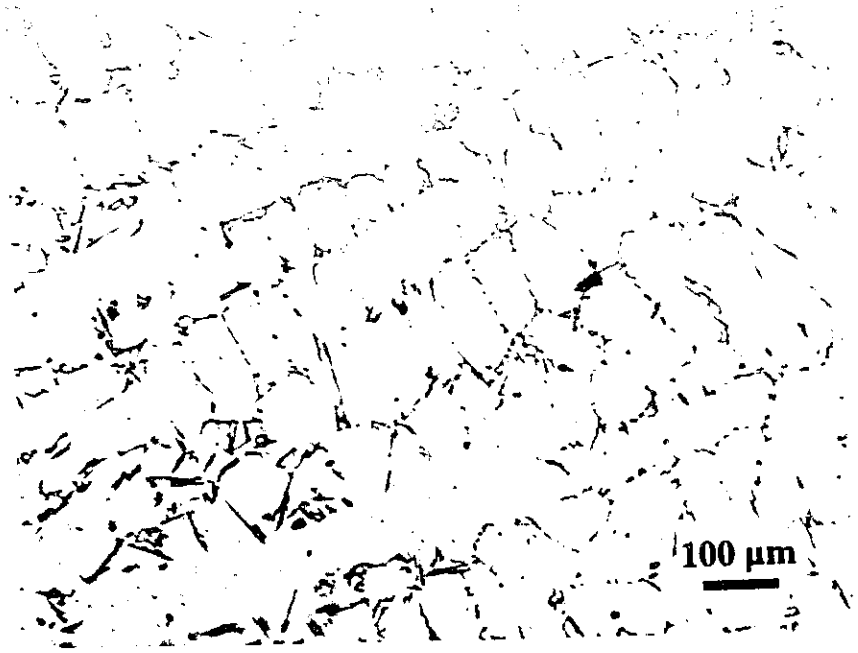

× 100

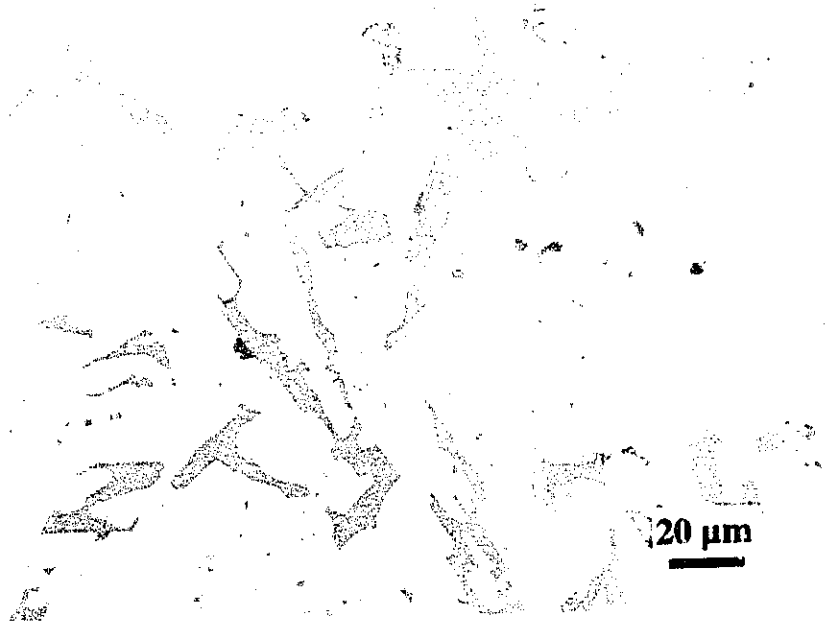

× 500

Fig.4.26 As-cast microstructure for alloy A356 + 1.0% In, cooling rate = 0.3°C/s.

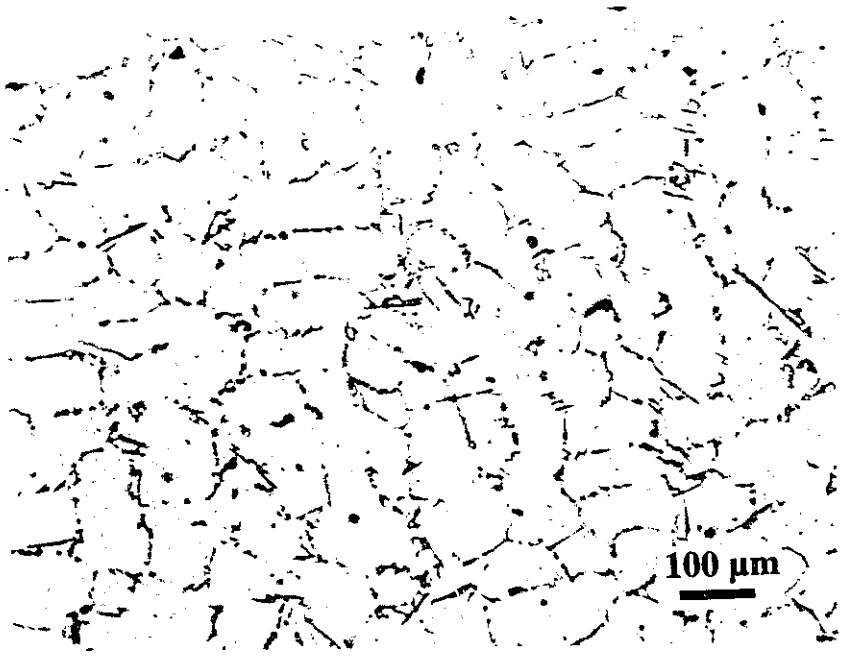

× 100

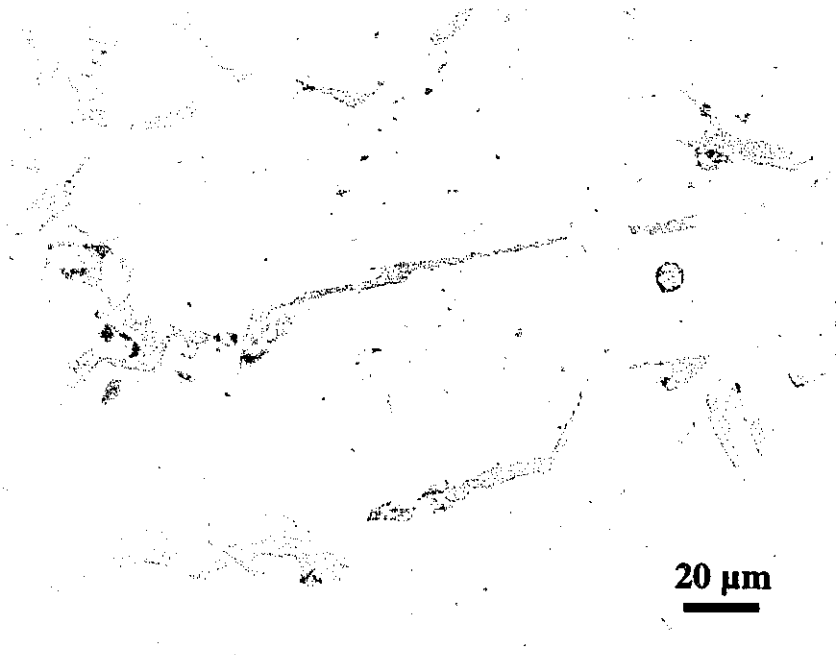

× 500

Fig.4.27 As-cast microstructure for alloy A356 + 1.0% Sn, cooling rate = 0.3°C/s.

4.3 MECHANICAL BEHAVIOR

The mean tensile and charpy test data for base alloy A356 and the base alloy containing the microalloying elements, solidified at a cooling rate 0.3^{0}C/s are given in Table 4.4. The results in Table 4.4 are based on a minimum of 3 test specimens (except where indicated). For the base alloy A356, the elongation to failure is low, and no necking was observed before fracture. For the A356 alloys containing Sb, which is the most effective element in DAS reduction and Si particle refinement, the yield and ultimate strengths are significantly increased. For 1.0% Sb the yield strength increases from 83 to 107 MPa, and the ultimate tensile strength increases from 124 to 156 MPa. The elongation to failure is slightly reduced from 1.29% to 1.26%; however for the 0.5% Sb addition the elongation is increased over 100% (3.15% vs 1.29%). The Sb addition effect is even more dramatic on impact energy, increasing from 1.51 J/cm^2 for the base alloy to 4.09 J/cm^2 for the alloy containing 1.0% Sb. Bi additions are also beneficial as evident from the data in Table 4.4, although only one tensile sample (sufficiently free of casting porosity) was available. The beneficial effects of the Sb and Bi additions to the A356 cast alloy is attributed principally to the modification of the eutectic Si particle, i.e. the change in the eutectic Si morphology from a coarse, faceted and needle-like form, to a finer, more rounded particle phase (see Fig.4.24 and 4.25). The In and Sn additions appear to have a slightly deleterious effect on the tensile properties of the base alloy, although there is a slight improvement in Charpy values, and this is consistent with the absence of any significant effect on the Si particle morphology.

The effect of an increased cooling rate on the tensile and impact energy of the A356

alloys is given in Table 4.5. Only Sb as a microalloying element was used in this test. The test specimens for the fast cooling rate were cast in the vented mold, from which then, rectangular specimens were melted for the tensile samples (see Fig.3.3). The excellent results show that gas porosity was largely eliminated using the specially designed graphite mold (Fig.3.1). The faster cooling rate has significantly increased all the mechanical properties of the base alloy, which must be attributed to the refinement of the dendrites (decreasing DAS), and the modification of eutectic Si particles as shown in Table 4.3 and Fig.4.18. The effect of the Sb addition is to further improve the UTS, E_f, and CVN values over the base alloy to approximately the same degree as for the slower cooled ingots, which is the result of further refinement in the DAS and the eutectic Si particles.

Table 4.4 Mechanical properties of A356 alloys, cylindrical test specimens cooling rate = 0.3°C/s

Alloy	0.2% Y_s (MPa)	UTS (MPa)	E_f (%)	CVN (J/cm^2)
A356 BASE	83±6	124±10	1.29±0.17	1.51±0.06
A356+ 0.5%Sb[1]	90	139	3.15	3.46±0.46
A356 + 1.0%Sb	107±3	156±2	1.26±0.05	4.09±0.16
A356 + 1.0%Bi[1]	93	150	4.31	3.53±0.27
A356 + 1.0%In	73±4	115±14	1.5±0.3	2.61±0.07
A356 + 1.0%Sn	76±5	102±13	0.9±0.1	1.92±0.30

Table 4.5 Mechanical properties of A356 alloys, rectangular test specimens cooling rate = 4.0°C/s

Alloy	0.2% Y_s (MPa)	UTS (MPa)	E_f (%)	CVN (J/cm^2)
356 BASE	124±11	170±27	3.1±0.5	2.4±0.1
356 + 1.0%Sb	94±9	190±8	9.3±1.5	5.9±0.1

[1] one tensile sample is recorded.

CHAPTER 5

CONCLUSIONS AND RECOMMENDATIONS

5.1 CONCLUSIONS

The following conclusions can be drawn from the results of this investigation:

1. The addition of the Al-insoluble elements Sb and Bi (0.5 - 1.0%) gave significant refinement (~50%) of the dendrite arm spacing in the hypoeutectic Al-Si alloys (A319 and A356 alloy), while Sn and In have no or little effect. The refinement of dendritic structure is attributed to the extremely small distribution coefficients for insoluble elements in Al (α), promoting the thermal and constitutional undercooling, and the resulting spontaneous development of secondary and tertiary dendrite arms.
2. Increasing the solidification (cooling) rate from 0.3^{0}C/s to 4.0 ^{0}C/s further refined the dendrite structure (decreasing DAS) by more than 100%, which is consistent with all solidification models, which show that supercooling and interfacial instability increases with solidification rate to promote dendritic growth (structure refinement).
3. The Sb and Bi additions modified the morphology of the eutectic Si particle from a coarse, faceted and sharp morphology to a finer, somewhat rounded and partially lamellar morphology, increasing the strength and toughness of the A356 alloy.
4. The eutectic Si particle modification has a significant effect on the eutectic

reaction, which is manifested in changes in the cooling curve: a depression of the eutectic temperature (T_E), an increase in the eutectic undercooling ($\Delta\theta$), and an increase in the undercooling (eutectic reaction) time (t1).

5. The addition of 1.0%Sb to the A356 alloy increased the ultimate tensile strength, elongation to failure, and impact toughness by approximately 20%, 200%, and 150% respectively for both slow and fast solidification rates.

5.2 RECOMMENDATIONS FOR FUTURE RESEARCH

The results of this investigation show that the mechanical properties of commercial, hypoeutectic Al-Si cast alloys can be significantly improved by microalloying with Al and Si-insoluble elements. However, before the above can be adopted to foundry practice and commercial exploitation, several phenomena and questions remain to be resolved.

1. The optimum levels of Sb (or Bi) for A356 and A319 to maximize improvements in mechanical properties (UTS, E_f, CVN) must be determined.
2. The effect of the Sb (or Bi) additions on low cycle fatigue of A356 and A319 alloys (a determining property for Al engine blocks for the automotive industry) must be determined.
3. The presence of insoluble element compounds (e.g. AlSb) or the pure metal phase (e.g. Bi) in the microstructure may have a highly deleterious effect on the corrosion behavior of the Al-Si alloy, and this requires investigation.

4. The structure refinement, and associated improvement in mechanical properties, increase with solidification (cooling) rate. The solidification rates in foundry practice (e.g. for engine blocks) vary considerably depending on the location in the casting. Thus full application of the microalloying technique for structure refinement in the industry requires developing comprehensive structure-composition-cooling rate (maps) for each insoluble element.

5. Not all Al and Si-insoluble elements were as effective as Sb (or Bi) in structure refinement, which may be surface energy related. A more detailed study of the solidification process through thermal analysis, TEM, and microstructure and phase analysis (elemental and structure) is required to determine what role surface energy plays in the refinement mechanism.

REFERENCES

1. R.C.Voigt: AFS Transactions, **99**, 33 (1991).
2. S.P.Iyer and W.V.Youdelis: Aluminum, **53**, 252 (1977).
3. W.V.Youdelis: Met.Sci., **13**, 540 (1979).
4. W.V.Youdelis and C.S.Yang: Mater.Sci., **16**, 275 (1982).
5. W.V.Youdelis: Met.Sci., **9**, 464 (1975).
6. W.V.Youdelis and J.Karov: Mater.Sci., Forum, **13/14**, 483 (1987).
7. T.Xiao and W.V.Youdelis: Mater.Sci.Tech., **5(10)**, 991 (1989).
8. J.E.Gruzleski and B.M.Closset: "The Treatment of Liquid Aluminum-Silicon Alloys", AFS (1990).
9. G.K.Sigworth, S.Skivkumar and D.Apelian: AFS Transactions, **97**, 811 (1989).
10. ASM Speciality Handbook: Aluminum and Aluminum Alloys, ASM International (1993).
11. M.Volmer and A.Weber: Z.Phys.Chem., **119**, 227 (1926).
12. R.Becker and W.Doring: Ann.Phys., **24**, 719 (1935).
13. D.Turnbull and J.C.Fisher: J.Chem.Phys., **17**, 71 (1949).
14. J.W. Rutter anf B.Chalmers: Can.J.Phys., **31**, 15 (1953).
15. I.Minkoff: "Solidification and Cast Structure", JOHN WILEY & SONS (1986).
16. W.W.Mullins and R.F.Sekerka: J.Appl.Phys., **35**, 444 (1964).
17. W.W.Mullins and R.F.Sekerka: J.Appl.Phys., **34**, 323 (1963).

18. T.F.Bower, H.D.Brody and M.C.Flernings: Trans, TMS-AIME, **236**, 624 (1966).

19. M.H.Burden and J.D.Hunt: J.Cryst.Growth, **22**, 109 (1974).

20. J.Lipton, M.E.Glickman and W. Kurz: Mater.Sci.Eng., **65**, 57 (1984).

21. G.P.Icantsov: Dokl.Akad.Nauk., SSSR, **58**, 567 (1947).

22. W. Kurz and D.J.Fisher: Acta Metall., **29**, 11 (1981).

23. D.J.Fisher and W.Kurz: Acta Metall., **28**, 777 (1980).

24. R.Trivedi, P.Magnin and W. Kurz: Acta Metall., **35**, 971 (1987).

25. R. Trivedi: Metall. Trans., **15A**, 977 (1984).

26. K.Somboonsuk, J.T.Mason and R.Trivedi: Metall. Trans., **15A**, 967 (1984).

27. L.X.Liu and J.S.Kirkaldy: Scripta Met., **28,** 1029 (1993).

28. D.Venugopalan and J.S.Kirkaldy: Acta Metall., **32**, 893 (1984).

29. L.X.Liu and J.S.Kirkaldy: Scripta Met., **29**, 801 (1993).

30. L.X.Liu and J.S.Kirkaldy: J. Crytal Growth, **140**, 115 (1994).

31. J.S.Kirkaldy: Metall. Trans., **24A**, 1689 (1993).

32. J.S.Langer and H.Muller-Krumbhaar: Acta Metall., **26**, 1681 (1978).

33. J.D.Hunt: "Solidification and Casting of Metals", The Metals Society (1979).

34. W.Kurz and D.J.Fisher: Fundamentals of Solidification, Trans.Tech.Publ. (1984).

35. W.A.Tiller, K.A.Jackson, J.W.Rutter and B.Chalmers: Acta Metall., **1**, 428 (1953).

36. V.G.Smith, W.A.Tiller and J.W.Rutter: Can.J.Phy., **33**, 723 (1955).

37. Metal Handbook, 9th edition, American Society For Metals (1988).

38. J.W.Mayer and S.S.Lou: "Electronic Materials Science: For Integrated Circuits

in Si and GaAs", Macmillan, New York (1990).

39. F. Weinberg, B. Chalmers, Can.J.Phy., **29**, 382 (1951)

40. R.E. Reed-Hill and R.Abbaschian: Physical Metallurgy, PWS Publ. (1994).

41. L.A.Darken: Trans. AIME, **175**, 184 (1948).

42. L.Ananthanarayanan and F.H.Samuel: AFS Transactions, **100**, 383 (1992).

43. D.Apelian, G.K.Sigworth and K.R.Whaler: AFS Transactions, **92**, 297 (1984).

44. B.L.Tuttle: "Principles of Thermal Analysis for Molten Metal Process Control", Proceedings of the Conference on Thermal Analysis of Molten Aluminum, AFS/CMI, Rosemout IL, 1-36 (1984).

45. N.Tenekedjiev, H.Mulazimoglu, B.Closset and J.Gruzleski: "Microstructures and Thermal Analysis of Strontium-Treated Aluminum-Silicon Alloys", AFS (1995).

46. H.L.Ge, W.V.Youdelis and G.L.Chen: Mater.Sci.Tech., **5**, 1207 (1989).

47. H.L.Ge, W.V.Youdelis, G.L.Chen and Q.Zhu: Mater.Sci.Tech., **5**, 985 (1989).

48. A.Flores et al.: Can. Meta. Quart., **33**, 133 (1994).

49. B.L.Tuttle, D.Twarog and E.Daniels: AFS Transactions, **99**, 7 (1991).

50. M.C.Flemings: "Solidification Processing", McGraw-Hill, Inc. (1974).

51. D.Turnbull and J.H.Hollomon: "Physics of powder metallurgy", McGraw-Hill, Inc., 109 (1951).

52. G.Tammann: Z.Metallkunde, **21**, 277 (1929).

53. Weixing Wang and J.E.Gruzleski: Mater.Sci.Tech., **5**, 471 (1989).

54. K.Radhakrishna, S.Seshan and M.R.Seshadri: AFS Transactions, **88**, 695 (1980).

55. A.J. McAlister: Bulletin of Alloy Phase Diagram, **5**, No.3, 4, 5 (1984).

APPENDIX A

CALCULATION OF CONCENTRATIONS OF INSOLUBLE SOLUTES NECESSARY FOR DENDRITIC GROWTH

McAlister and Murray [55] give the following ΔG^{XS} functions for the insoluble elements in liquid Al. It can be assumed that the presence of the other alloying components will alter these, but to what extent is unknown.

For Al-Sb system: A.J.McAlister gives

$$\Delta G^{xs} = C_{sb}(1-C_{sb})[-4490.7-4.3338T + (8839.1-0.5196T)(1-2C_{sb}) + (3372.4-0.2431T)$$
$$(1- 6C_{sb} + 6C_{sb}^2) + (-1885.2+0.2909T)(1-12C_{sb} + 30C_{sb}^2 - 20C_{sb}^3)]$$

For Al-Bi system: A.J.McAlister gives

$$\Delta G^{xs} = C_{Bi}(1-C_{Bi})[30972.9 - 6.878T + (17612.5-7.514T)(1-2C_{Bi}) + (13121.5-8.642T)$$
$$(1- 6C_{Bi} + 6C_{Bi}^2) + (2629.5-0.723T)(1-12C_{Bi}+30C_{Bi}^2-20C_{Bi}^3)]$$

For Al-Sn system: A.J.McAlister gives

$$\Delta G^{xs} = C_{Sn}(1-C_{Sn})[23810.8-15.707T + (-102.3+5.455T)(1-2C_{Sn})$$
$$+ (-6728.6+8.490T)(1 - 6C_{Sn}+ 6C_{Sn}^2)$$

For Al-In system: J.L.Murray gives

$$\Delta G^{xs} = C_{In}(1-C_{In})\{19188 + 2561(1-2C_{In}) + 7996(1-2C_{In})$$
$$- T[-1.2443 + 12.18(1-2C_{In}) + 5.4329(1-2C_{In})^2 - 0.8351(1-2C_{In})^3]\}$$

Using the above expression for the excess free energies in liquid Al, and Eq.(2-54) and Eq.(2-50), the "uphill diffusion" occurs component in the diffusive flux is present ($\partial D_c/\partial C_c > 0$) when

$$C_{Sb} >= 14 \text{ at\%}$$

$$C_{Bi} >= 16 \text{ at\%}$$

$$C_{In} >= 18 \text{ at\%}$$

$$C_{Sn} >= 27 \text{ at\%}$$

APPENDIX B

CALCULATION OF DISTRIBUTION COEFFICIENTS

Fig. B1 [55] shows the phase diagrams of the Al-Sb and Si-Sb systems; Fig. B2 [55] is the Al-Bi and Si-Bi systems; Fig. B3 [55] is the Al-In and Si-In systems; Fig. B4 [55] shows the phase diagrams for the Al-Sn and Si-Sn systems. The distribution coefficients from each diagram can be determined by the use of $k_0 = C_s / C_l$ in weight percent. For the distribution coefficient of Sb in Al at 657^{0}C, the concentration of solid C_s is 1.7 wt% (i.e. 0.4 at% Sb is [122×0.4%] / [122×0.4% + 27×99.6%] = 1.7 wt%), and 50 at% for AlSb is 81.8 wt% Sb giving, $k_{Sb}^{Al} = 0.025$ which drops to less than 0.001 at 600^0 C. The other coefficients are $k_{Bi}^{Al} = 0.000357$ at 656 ^{0}C, $k_{In}^{Al} = 0.00055$ at 630 ^{0}C, and $k_{Sn}^{Al} = 0.00035$ at 550 ^{0}C. The silicon systems are just as insoluble producing $k_{Sb}^{Si} < 0.001$ at 630 ^{0}C, and $k_{Bi}^{Si} < 0.000018$, $k_{In}^{Si} = 8 \times 10^{-6}$, $k_{Sn}^{Si} < 0.0001$ at 670 ^{0}C.

Al-Sb

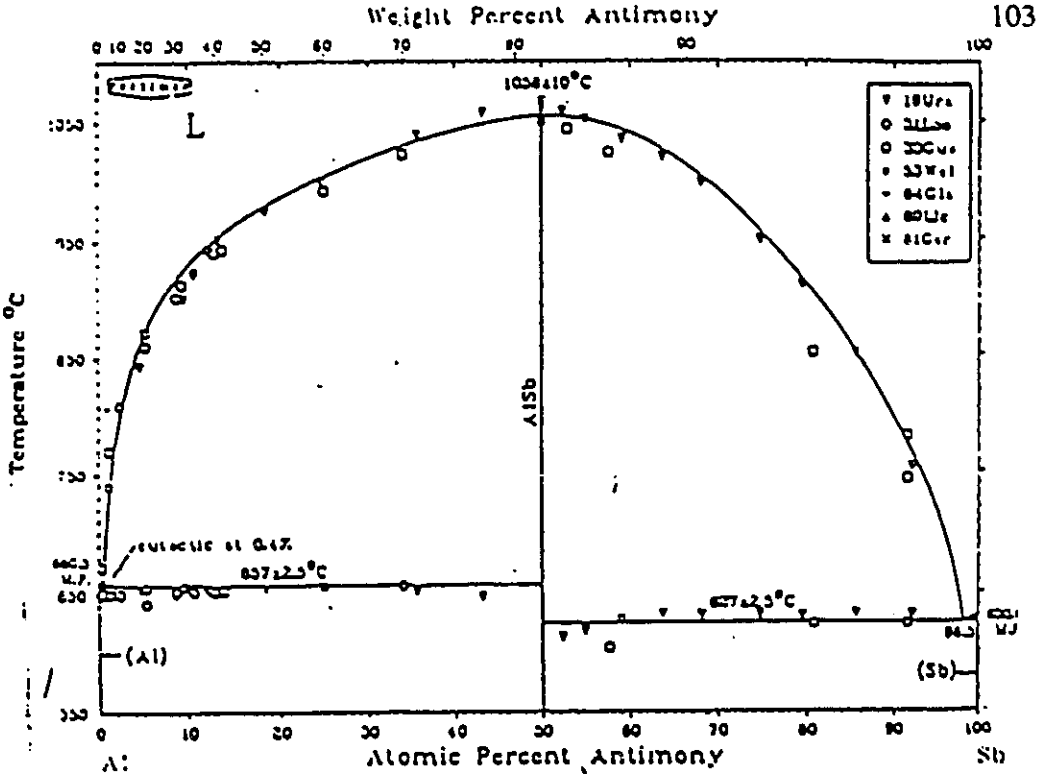

Sb-Si

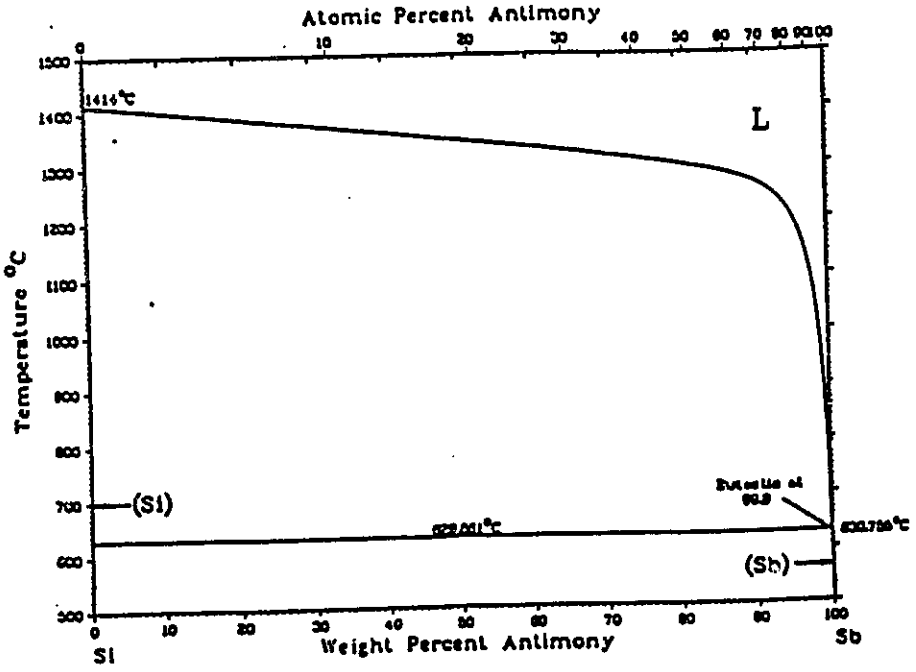

Fig.B1 Phase diagrams of Al-Sb and Si-Sb systems [55].

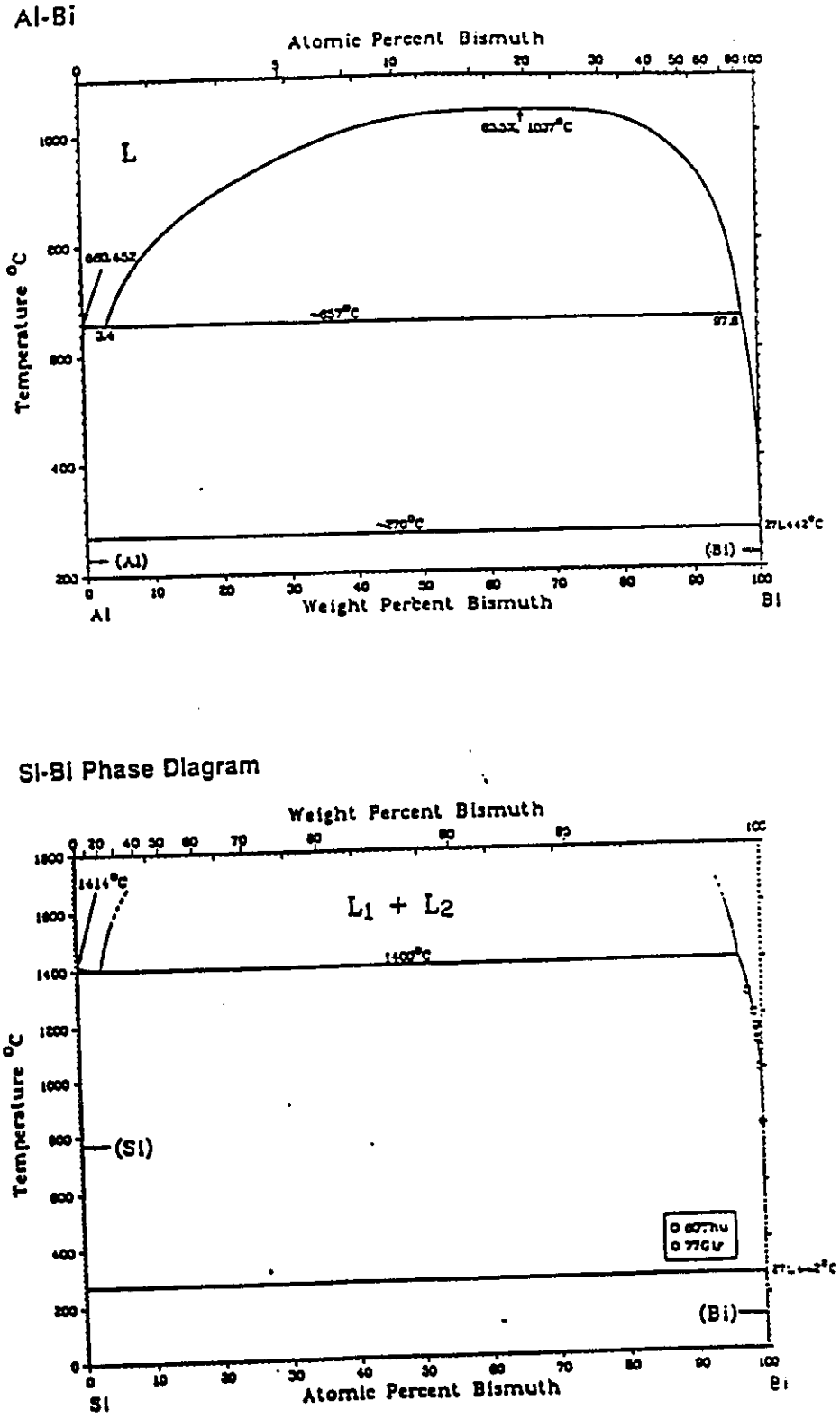

Fig.B2 Phase diagrams of Al-Bi and Si-Bi systems [55].

Al-In

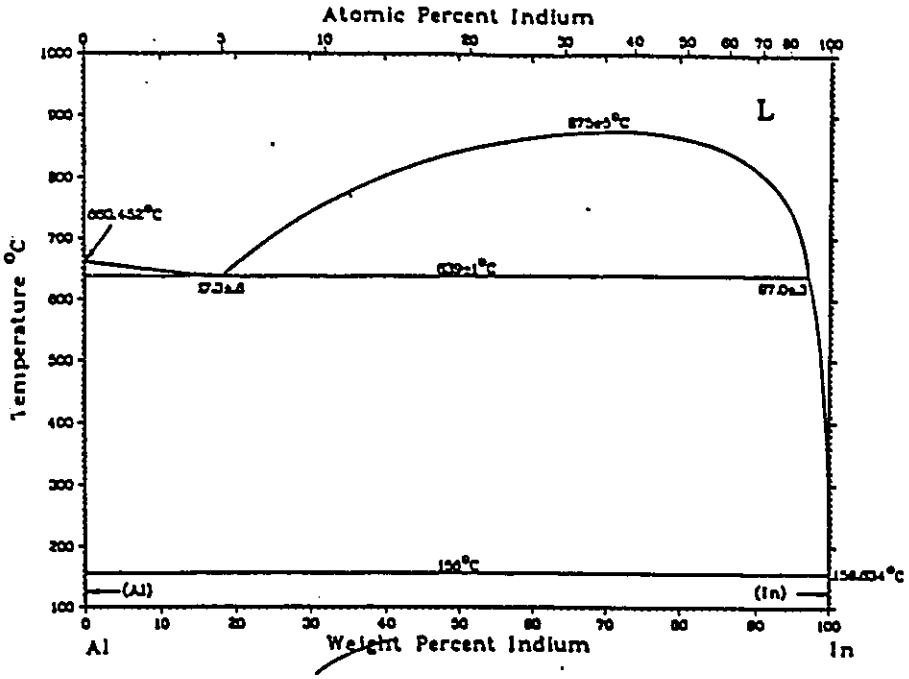

In-Si

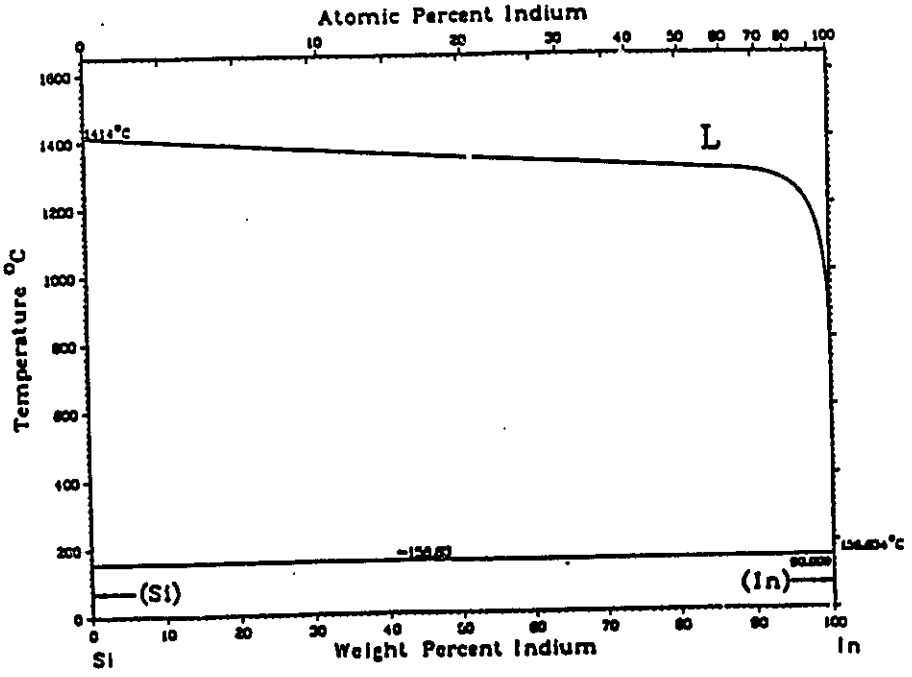

Fig.B3 Phase diagrams of Al-In and Si-In systems [55].

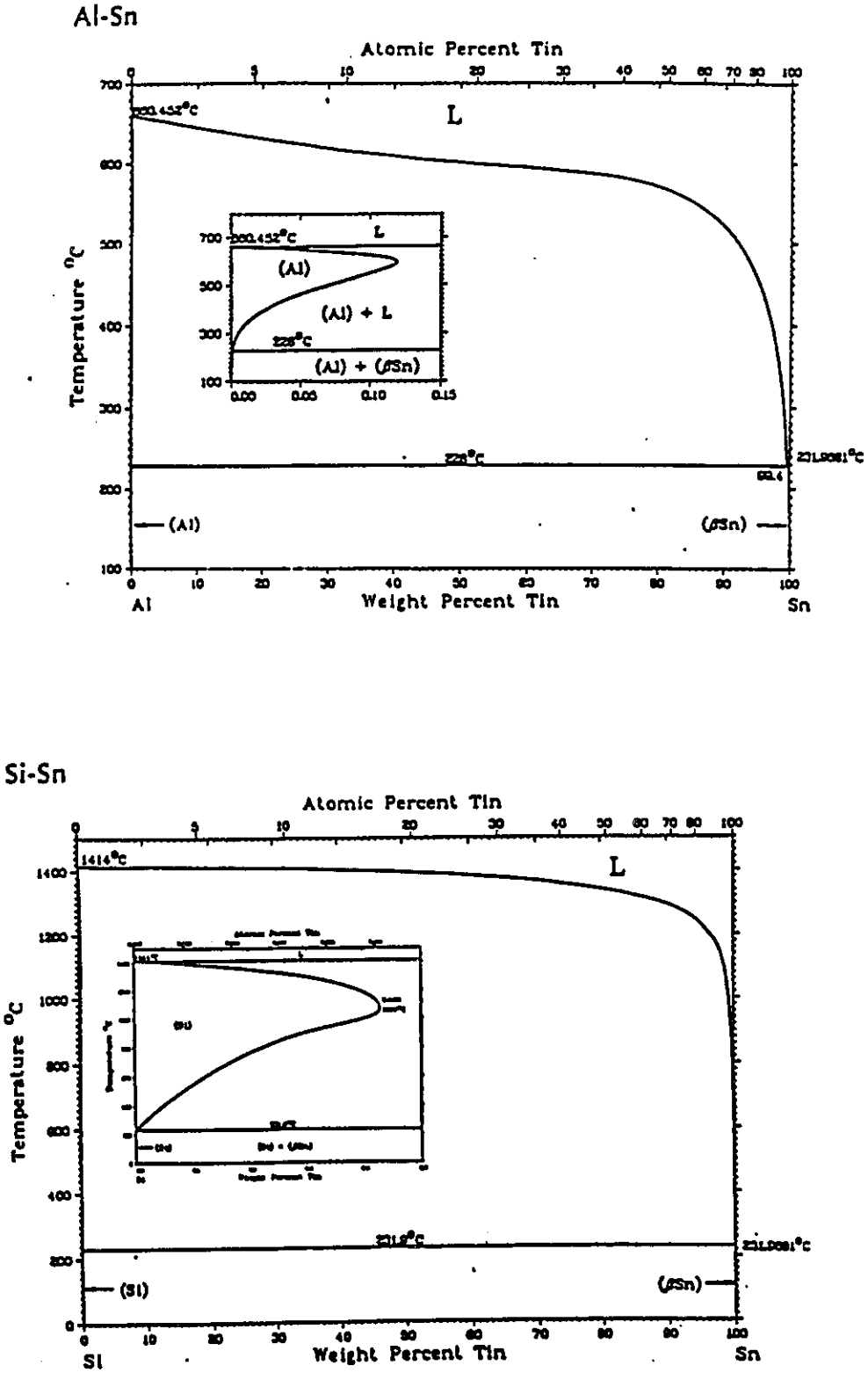

Fig.B4 Phase diagrams of Al-Sn and Si-Sn systems [55].

VITA AUCTORIS

November 1970	Born in People's Republic of China
July 1991	Graduated with B.Sc. degree in Engineering, Department of Flight Vehicle Engineering, Beijing Institute of Technology, Beijing, China
1991-1993	Assistant Engineer, Beijing Institute of Control Engineering, Chinse Academy of Space Technology, Beijing, China
January 1994	Registered in M.A.Sc. Program in Engineering Materials, Department of Mechanical and Materials Engineering, University of Windsor, Windsor, Ontario, Canada